JOHANNES GUTENBERG-UNIVERSITÄT MAINZ

Inside Perovskite Solar Cells
Charges at Interfaces

Dissertation

zur Erlangung des Grades

„Doktor der Naturwissenschaften“

am Fachbereich Physik, Mathematik und Informatik

der Johannes-Gutenberg-Universität in Mainz

vorgelegt von

Victor Wolfgang Bergmann

geb. in Mainz

Mainz, den 16.07.2019

Zusammenfassung

Eine der vielversprechendsten Photovoltaik-Technologien der nächsten Generation ist die Solarzelle auf Perowskit-Basis. In den letzten 7 Jahren konnte ihr zertifizierter Wirkungsgrad auf unvergleichliche Weise gesteigert werden. Als relativ junge Technologie sind jedoch verschiedene Prozesse auf der Nanoskala an den Grenzflächen der dünnen Schichten innerhalb der Perowskit-Solarzelle nicht vollständig verstanden. Das bedeutendste Beispiel hierbei ist die Hysterese in den Strom-Spannungs-Kennlinien. Durch Anlegen einer externen Spannung oder durch einfaches Beleuchten der Solarzelle über ein Zeitintervall kann der Zustand einer Zelle so geändert werden, dass die Effizienz der Ladungsextraktion danach über mehrere Sekunden erhöht oder verringert wird. Vorschläge über die zugrunde liegenden Prozesse sind unter anderem bewegliche Ionen innerhalb der Perowskitschicht oder gespeicherte Ladungen an den Grenzflächen. Beide Prozesse haben gemeinsam, dass sie das elektrische Feld innerhalb der Zelle verändern und dadurch die Dynamik des Ladungsaustauschs an den Grenzflächen beeinflussen.

Mit der Kelvinsonden-Kraftmikroskopie konnte ich die Verteilung der Kontaktpotentialdifferenz im Nanometerbereich über den Querschnitt für verschiedene Perowskit-Solarzellentypen abbilden. Aus der Kontaktpotentialdifferenz konnte ich die interne Potentialverteilung bestimmen, sowie das elektrische Feld und die korrelierte Ladungsverteilung berechnen. Bei gleichzeitigem Kontaktieren der Elektroden mit einer externen Spannungsquelle und der Beleuchtung mit einer Weißlichtquelle konnten sowohl der Gleichgewichtszustand der Zellen als auch die Änderungen unter verschiedenen Betriebsbedingungen untersucht werden. Durch kontinuierliches Messen über dieselbe definierte Linie auf dem Zellenquerschnitt wurden Änderungen der Kontaktpotentialdifferenz unter Stimulation der Solarzelle in Abhängigkeit der Zeit gemessen (Licht ein/aus, externe Vorspannung usw.).

Ich beobachtete, dass in Perowskit-Solarzellen ein p-i-n-Übergang besteht. An den Grenzflächen der Perowskitschicht kann im Gleichgewicht durch eine Verschiebung von beweglichen Ionen und mobilen Ladungen eine Bänderverbiegung auftreten. Eine beim Herstellungsprozess unbeabsichtigte spontane Selbstdotierung der Perowskitschicht bestimmt dabei das Verhältnis der Bandverbiegung an den beiden Grenzflächen der Perowskitschicht. Da diese Verbiegung der Bänder die Ladungsextraktion beeinflusst, trat in den meisten Zellen eine ungleiche Rekombination von Ladungsträgern an den jeweiligen Grenzflächen auf, die zu einer höheren Dichte von Löchern innerhalb der Perowskitschicht unter Betriebsbedingungen führte. Mit der zeitabhängigen Analyse der dynamischen Prozesse konnte ich zwischen elektronen- und ionenbasierten Prozessen unterscheiden. Durch den Vergleich der Zeitkonstanten aus den Änderungen des gemessenen Stroms mit den Änderungen der Potentialverteilung konnte die Verschiebung der Ionen direkt mit der Hysterese in den IV-Eigenschaften in Verbindung gebracht werden.

Meine Arbeit gibt einen Überblick über die Verteilung des elektrischen Potentials innerhalb verschiedener Perowskit-Solarzellen und die verschiedenen Prozesse, die diese beeinflussen können. Diese Prozesse können sich direkt auf die Betriebsbedingungen und die Vorschaltungszustände einer Zelle auswirken. Mit den Erkenntnissen aus meiner Arbeit können nun interne Prozesse besser zugeordnet werden und Zellen auf Grund ihres Ansprechverhaltens kategorisiert werden.

Abstract

The most promising next-generation photovoltaic device is the perovskite based solar cell. Over the past 7 years, their certified power conversion efficiency increased dramatically. As a relatively young system, the device physics of various nanoscale processes at the interfaces of the thin layers within an operating perovskite solar cell remain unclear. The most significant example of such a process is the hysteresis in the current-voltage characteristics. By applying an external voltage or illuminating the device for several tens of seconds, the state of the charge extraction dynamics can be modified in a way that requires some time for the cell to get back into equilibrium after switching off the external stimulus. Suggestions about the underlying processes include a migration of ions inside the perovskite layer or trapped charges at the interfaces. Both processes have in common, that the electric field within the device is changing and with it the dynamics of charge extraction at the interfaces are affected. To detect the processes at the interfaces it is necessary to introduce a technique, which can access to the inner layer structure and is able to resolve these on a nanoscale.

With cross-sectional Kelvin probe force microscopy, I was able to image the distribution of the contact potential difference (CPD) on a nanoscale within various types of perovskite solar cells. From the CPD I could determine the potential distribution as well as calculate the electric field and the correlated charge distribution. With a broad band white light and connections of the electrodes to an external voltage source, the equilibrium state and changes under different operating conditions could be studied. By continuously scanning over the same defined line on the cell's cross-section, time-resolved changes in the CPD upon stimulating the device were measured (e.g. light on/off, external bias, etc.).

I observed that a p-i-n junction is present within a perovskite solar cell. Band bending at the interfaces of the active layer can appear in equilibrium due to migrating ions and mobile charges, which are driven towards the interfaces upon the influence of the built-in electric field. Depending on the fabrication process, unintentional self-doping of the perovskite layer determines the proportion of the band bending between both interfaces of the perovskite layer. As this band bending impacts the charge extraction, an imbalanced interfacial recombination occurred in most cells, which lead to an accumulation of holes inside the perovskite layer under operating conditions. With a time-dependent analysis, I was able to distinguish between dynamic electronic charge and ion-based processes. By comparing the time constant of the changes in the current output with the changes in the CPD distribution the located process of migrating ions could be directly connected with the hysteresis in the IV-characteristics.

My study gives an overview over the distribution of the electric potential and the various processes that can alter it within different kinds of perovskite solar cells. These processes have a direct effect on the operating conditions and the preconditioning states of a cell. With the new knowledge about the effects of preconditioning or self-doping, external observations can now be correctly correlated with the internal processes.

Content

Abbreviations

AC ..... *Alternating Current*
ACS ..... *American Chemical Society*
AFM ..... *Atomic Force Microscopy*
AM-KPFM ..... *Amplitude Modulation Kelvin Probe Force Microscopy*
$CaTiO_3$ ..... *Calcium Titanate*
$CH_3NH_3PbI_3$ (MAPI) ..... *Methylammonium Lead Iodide*
CH_4 ..... *Methane*
CIGS ..... *Copper Indium Gallium Selenide*
CO_2 ..... *Carbon Dioxide*
CPD ..... *Contact Potential Difference*
DC ..... *Direct Current*
EBIC ..... *Electron Beam Induced Current*
EDX ..... *Energy-Dispersive X-ray*
E_F ..... *Fermi Energy*
E_G ..... *Band Gap*
EPFL ..... *École Polytechnique Fédérale de Lausanne*
ETL ..... *Electron Transport Layer*
FAI ..... *Formamidinium*
FF ..... *Fill Factor*
FIB ..... *Focused Ion Beam*
FM-KPFM ..... *Frequency Modulation-Kelvin Probe Force Microscopy*
FTO ..... *Fluorine Tin Oxide*
HTL ..... *Hole Transport Layer*
IS ..... *Impedance Spectroscopy*
I_{SC} ..... *Short Circuit Current*
ITO ..... *Indium Tin Oxide*
IV ..... *Current vs. Voltage*
JV ..... *Current Density vs Voltage*
KPFM ..... *Kelvin Probe Force Microscopy*
MA ..... *Methylammonium*
MAI ..... *Methylammonium*
N_2O ..... N*itrous Oxide*
NREL *National Renewable Energy Laboratory*
PCE ..... *Power Conversion Efficiency*
PID ..... *Proportional-Integral-Derivative*
PL ..... *Photoluminescence*
P_{MAX} ..... *Maximum Power Point*
PPP-EFM . *PointProbe Plus Electrostatic Force Microscopy*
SEM ..... *Scanning Electron Microscope*
SPM ..... *Scanning Probe Microscopy*
STEM ..... *Scanning Transmission Electron Microscopy*
STM ..... *Scanning Tunneling Microscopy*
TA ..... *Transient Absorption*
TiO_2 ..... *Titanium Dioxide*
UPS .... *Ultraviolet Photoemission Spectroscopy*
UVA ..... *Ultraviolet A*
UVB ..... *Ultraviolet B*
V_{OC} ..... *Open Circuit Voltage*
XPS ..... *X-ray Photoelectron Spectroscopy*

1. Motivation

"I'd put my money on the sun and solar energy. What a source of power! I hope we don't have to wait until oil and coal run out before we tackle that."

— Thomas Edison

Without a doubt, Thomas Alva Edison was one of the most important inventors in the 20th century. A huge number of his developments helped to push the process of electrification, as part of the industrial revolution. Today in times of the digital age, almost 87 years after Edison's death, his outlook is more prominent than ever. Our daily life becomes more and more dependent on devices which consume enormous amounts of energy. Although oil has not run out and predictions about the aftermath of the "peak oil" (an expected rapid decline of oil production based on the limitations in the earth's reservoir) are still under debate,[1] Edison's message stays highly relevant. Even if our generation will not suffer from a shortage of oil or coal, still every following generation will suffer from the consequences of the combustion of fossil fuels with air pollution and climate change. In 2013 the "intergovernmental panel on climate change", a group of leading experts in the field, gathered together to discuss the most relevant publications in their field.[2] They gave clear evidence that over the past decades the average temperature on the planet is increasing. Furthermore, with the help of computer simulations and the corresponding experimental data they confirmed that the increasing greenhouse gas concentration and the connected rise in positive radiative force is the major cause for this increase in temperature. By calculating the contributions for different greenhouse gases, e.g. CH_4 and N_2O from domestic livestock and rice cultivation, they showed that the CO_2-emission of the energy sector is the main part with 60% of the global emissions.[3] To further limit global warming in the next decades, the industrial nations agreed on a program to limit the rise in temperature, compared to the preindustrial times, to 2 °C by reducing the amount of greenhouse gas emission.[a] With an ongoing worldwide increase in demand of energy, an awareness to look for alternative solutions in the energy supply sector becomes more and more important. Beginning of 2017, one of the leading scientists in the field of climate research, Prof. Dr. Mark G. Lawrence (Institute for Advanced Sustainability Studies, Potsdam), presented about "What does physics tell us about possibilities of achieving the Paris Agreement climate goals?" in the Physics colloquium of the University Mainz (January 31st, 2017). Several possibilities for projects were presented, which could help to reduce the emission of greenhouse gases, or simply to slow down the trend of global warming.

Harvesting so called "green" energies is a widely known alternative solution against the combustion of fossil fuels. As an example, the German government adopted a plan for 2050 to obtain 80 % of the energy supply from green energies.[b] On that

[a] *UN Climate Change Conference COP21 CMP11; http://www.cop21.gouv.fr/en/*

[b] *Energieziel 2050; http://www.umweltbundesamt.de/publikationen/energieziel-2050*

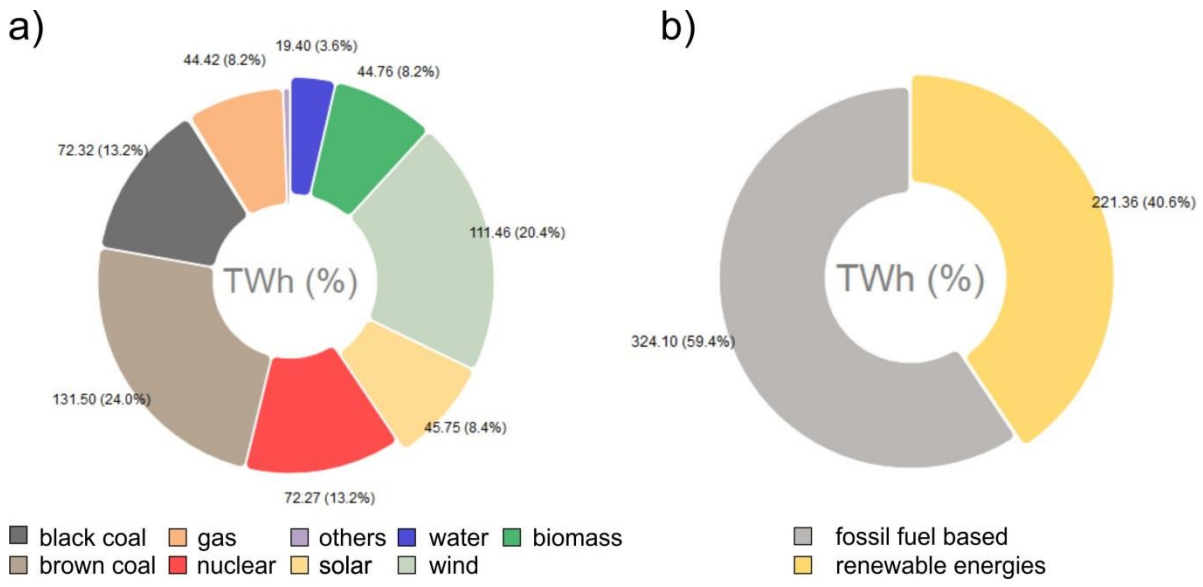

Figure 1: (a) German power production in 2018 from power plants for public power supply, divided into different energy sectors with the corresponding amount in TWh (and the percentage compared to the total production). (b) Same data as in part (a) divided in fossil fuel based and renewable energies.

(Data from the *Fraunhofer ISE website*, https://www.energy-charts.de with the data being extracted from 50 Hertz, Amprion, Tennet, TransnetBW, Destatis, EEX)

account a study was released, which described the possibility to completely change the energy supply to green energies until 2050, based on today's existing technology. Solar energy and explicitly photovoltaic is playing a crucial role in that plan, with covering up to 25 % of the German demand for electricity.[c] However, the significance of photovoltaics in the energy market is still behind it's potential (8.5 % in 2018; Figure 1).

While in the past decades the demand for energy drastically increased, the actual integration of photovoltaics into the energy market is relatively young. The key factor for increasing the fraction of solar energy in the market is the development of a next generation solar cell, which needs to be highly efficient, cheap, flexible or even transparent. These additional requirements for next generation solar cells to access a broader range of applications, like the integration into windows or into automotive, pose new challenges for this technology. Today, researchers around the world are working on the next generation of photovoltaics with the perovskite solar cell being the most recent and most promising discovery. Ever since its first introduction in 2009 and a first certified record power conversion efficiency in 2012, perovskite-based photovoltaics could be dramatically optimized to a value, which can nowadays compete with the state-of-the-art silicon-based technology. However, the young perovskite photovoltaic technology is still facing various problems, since

[c] *Energiekonzept 2050; http://www.fvee.de/fileadmin/politik/10.06.vision_fuer_nachhaltiges_energiekonzept.pdf*

various processes of the device physics still remain unclear. As the optimization of engineering efficient perovskite based solar cells continues, studies about the basic device physics is inevitable to understand and optimize this system.

A more detailed introduction into the exact underlying questions and further the motivation for the experiments which I performed, is given in the chapters 2.2.3 – "The evolution of perovskite solar cells" and 2.2.4 – "Hysteresis". In order to understand the basic knowledge for the research on the next generation solar cells, I will start with an introduction of the theoretical fundamentals and the history about the systematic use of solar power to harvest electrical energy.

2. Fundamentals

"I learned very early the difference between knowing the name of something and knowing something."
— Richard Feynman

2.1. Photovoltaics – A Brief Introduction into the Physics

The basic working principle of a photovoltaic cell relies on the generation of a voltage upon light absorption (photovoltaic effect). To participate in the process, the absorbed photon needs to exceed a lower limit of energy, which is defined by the width of the band gap E_G of the absorbing semiconducting material (Figure 2).

Semiconductors are the intermediate between electrical conductors and isolators. In the periodic table the most important pure elements with semiconducting properties (like silicon or germanium) can be found in group IV. However, there are more semiconducting elements or compounds and in general the classification is determined by their electronic band-structure, hence the allowed energy levels for the electrons in the structure.
The quantum mechanical description for an electron to move freely in a system is given by the wave function $\psi(\vec{x})$

$$\psi(\vec{x}) = Ce^{i(\vec{k}\cdot\vec{x})} \qquad (1)$$

with the wave vector $\vec{k}$ pointing in the direction of the wave propagation. By solving the Schrödinger equation with the corresponding boundary conditions of the system, we can find explicit solutions for the parameters of the wave functions

$$\frac{\hbar}{2m}\nabla^2\psi(\vec{x}) - U(\vec{x})\psi(\vec{x}) = E\psi(\vec{x}) \qquad (2)$$

with the potential $U(\vec{x})$ and the eigenvalue E of the wave function. The solution for a confined space with boundary conditions of infinite potential walls results in discrete energy states in the system. These discrete energy states become denser and converge against the continuous limit, with the width of the potential spreading over a respectively large distance. In case of a crystal lattice this is true, since the periodic potential of the single atom spreads across the whole crystal. According to Bloch's theorem the periodicity of the potential leads to the solution of the electrons wave function

$$\psi(\vec{x}) = u(\vec{x})e^{i(\vec{k}\cdot\vec{x})} \qquad (3)$$

whereas $u(\vec{x})$ being a periodic function with the same periodicity as the potential $U(\vec{x})$ and hence the crystal lattice. Thereby, the almost continuous energy levels split up and energy gaps E_G form, which represent no solutions of the Schrödinger equation and therefore forbidden zones for the occupation of electrons. As a consequence, there are allowed energy bands with energy gaps separating these

bands. To further characterize a solid whether it is defined as an insulator, semiconductor or a conductor, the location of the Fermi energy E_F of the system is determining.

Giving a limited number of electrons N into a system, the electrons fill the energy states from bottom to top. The Pauli principle thereby states that only two electrons of spin up and down can occupy a single energy state. At a temperature of $0\ K$ all states below a certain energy $E_{N/2}$ in the system are occupied by electrons and E_F can be determined as the energy of the highest occupied state. Under realistic conditions ($T > 0$) however, energy is fed into the system and E_F corresponds to the exact energy level, where the occupation probability for an electron is $1/2$. With the help of the Fermi-Dirac statistic we can calculate the occupation probabilities of the energy bands within the system

$$p(E) = \frac{1}{1+exp\left(\frac{E-E_F}{k_B T}\right)} \qquad (4)$$

with the Boltzmann constant k_B and the absolute Temperature T. The exact position of the Fermi energy compared to the location of the nearest band gap E_G in the system is crucial for the electric properties of the solid.
If E_F is located within an energy band, a significant number of mobile electrons occupy the band above E_F (conduction band). The solid is therefore classified as an electrical conductor (Figure 2).

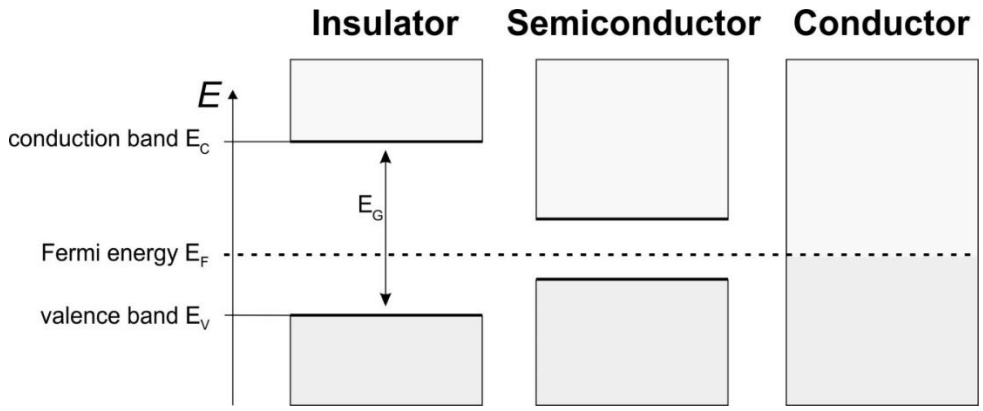

Figure 2: Band diagram for the three cases of an insulator, a semiconductor and a conductor. While for the Insulator the fermi level is within the band gap with a large ΔE towards the conduction band, for the semiconductor the band gap is smaller and the ΔE is narrow compared to the thermal energy. For the semiconductor the fermi level is located in an energy band, which results in the mobility of charges within the band.

If E_F is located within a band gap E_G there are two options:
First option is that the width of the band gap is large compared to the thermal energy, resulting in an absence of electrons within the conduction band and an almost completely occupied band underneath (valence band). This configuration ends in electrical insulating properties, hence an insulator.
Second option is a band gap which is comparatively narrow to the thermal energy. Therefore, an increase in temperature or generally the addition of energy to the system results in a significant probability to find mobile electrons within the conduction band, leading to semiconducting properties, hence a semiconductor.

When a semiconductor is exposed to photons with the wavelength λ with the corresponding energy $E_\lambda = \frac{hc}{\lambda} \geq E_G$, the photon can be absorbed by an electron in the valence band which will be subsequently excited to the conduction band. The excited electron leaves behind a positive charged electron hole in the valence band. The Coulomb interaction between the electron and the hole forms a neutral quasi-particle called exciton.

Exciton The total energy of the exciton is the sum of the energy gap E_G, the kinetic energy E_K and the binding energy E_B due to the Coulomb force. E_B can be described as

$$E_B = \frac{1}{2}\frac{\mu^* e^4}{(4\pi\varepsilon_0)^2\varepsilon^2\hbar^2}\frac{1}{n^2} \qquad (5)$$

with the effective mass μ^*, the dielectric constant of the semiconductor ε, the dielectric constant of vacuum ε_0 and the quantum state *n (n=1, 2...)*. Under the influence of an electric field or the addition of thermal energy, the charges can overcome the binding energy producing free electrons/holes. Without charge dissociation within the lifetime of the exciton τ_E, the exciton recombines again.

Exciton dissociation and the controlled transfer of the generated free charges in opposite directions are the basic mechanisms for the functionality of solar cell devices. In inorganic semiconductors, the exciton binding energies are low (*~10 meV*) compared to the thermal energy (k_BT = *26 meV at 25* °C). Free charges are already present within the inorganic semiconductor upon exposure with light of the proper wavelength making them a perfect candidate to harvest electrical energy from light.

2.1.1 Inorganic Solar Cell

After the absorption of a photon with sufficient energy and a resulting excited electron in the conduction band (hole in the valence band), the charge dissociation process relies on an electric field to efficiently transfer the electron (hole) towards the electrode and thereby generate a current. A fundamental way to integrate an internal electric field into a semiconducting device is to include a pn-junction.

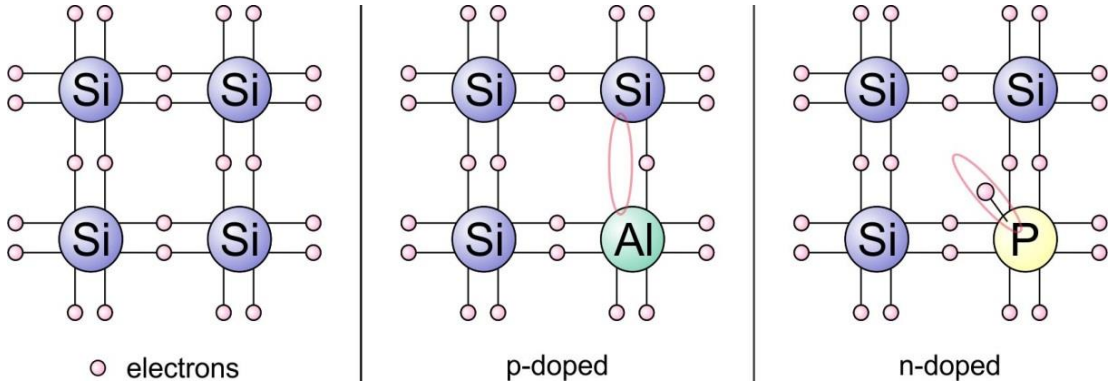

Figure 3: (a) Schematic silicon crystal scheme showing the atom cores and the respective electron bonds projected on a 2D plane. (b) Schematic silicon crystal scheme p-doped with an Al atom and thereby a missing electron for the respective crystal bonds. The missing electron is delocalized over the crystal and thereby mobile at room temperature. (c) Schematic silicon crystal scheme n-doped with a Phosphor atom and thereby an additional electron, which is delocalized over the crystal and thereby mobile at room temperature.

pn-Junction As silicon is the most common material in semiconductor industry, it serves as the example to explain the different steps it takes to assemble the pn-junction. In a silicon crystal, the valence electrons build covalent bonds with their next neighbors. Every silicon atom shares its four valence electrons respectively with the four surrounding silicon atoms (Figure 3a) to form a diamond cubic structure. When an atom of group III with three valence electrons replaces a silicon atom in the crystal lattice structure (in this case aluminum), one electron is missing to build the four respective covalent bonds (Figure 3b). Thereby holes are present at these impurities, whereas electrons from the neighboring bonds can change into this position. Since these impurities lead to an electron accepting affinity, the material is called p-doped or a p-type material. In case of an n-type material the crystal is doped with atoms of group V (Figure 3c - phosphor). With five valence electrons but only four necessary covalent bonds for the crystal structure, these impurities reveal one weakly bound electron which is already mobile at room temperature.

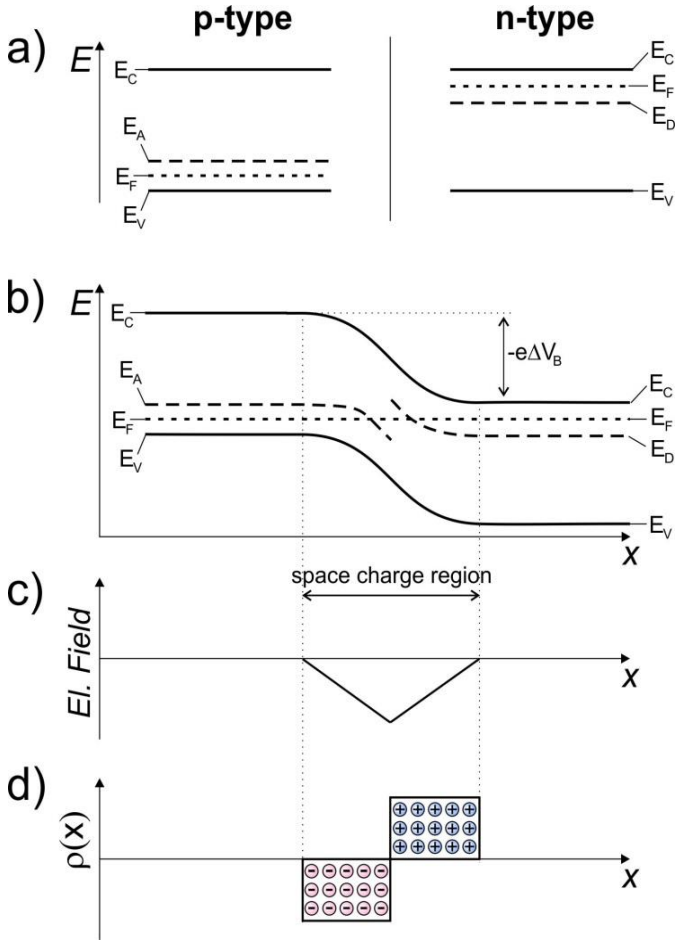

Figure 4: Schematic assembly of a pn-junction. (a) Energy diagram of the p-type semiconductor on the left and the n-type semiconductor on the right with the energy levels for the conduction band E_C, energy level of acceptor sites E_A, Fermi energy E_F, valence band E_V and energy level of donator sites E_D. (b) When the contact, fermi levels align via a shift of electrons from the donor to the acceptor. The charges arrange at the interface and hence form an electric field (c) & (d).

The weakly bound electrons of the n-type material locally create an extra "donator" energy level E_D within the band gap right underneath the conduction band E_C (Figure 4a). In the p-type material an additional "acceptor" energy level E_A is created where an electron can occupy the fourth covalent bond. Once the p-type and the n-type materials are connected, electrons at the interface start to diffuse from E_D to the energetically favorable state E_A. This diffusion current continues until the Fermi levels of both systems are aligned (Figure 4b) and the resulting electric field creates an equal sized drift current. With the alignment of the Fermi levels the band levels shift with respect to each other. The resulting energy difference is proportional to the built-in potential ΔV_B and develops across the space charge region (also called depletion region). Hence, an electric field develops across the depletion region (Figure 4c).

p-i-n-Junction Different from the pn-junction in the p-i-n junction an intrinsic, or undoped region is sandwiched between the oppositely doped layers (Figure 5). With no free charges within the intrinsic region and the Fermi level alignment due to the contact, the band bending only appears at the interfaces towards the intrinsic region. As a result, a constant electric field is generated within the intrinsic layer.
In order to create a functional photovoltaic device, the pn or p-i-n junction is sandwiched between two electrodes. Photo excited electrons that reach the depletion region, are directed towards the p-type material and the respecting electrode, while the respective holes are directed towards the n-type material and hence the other

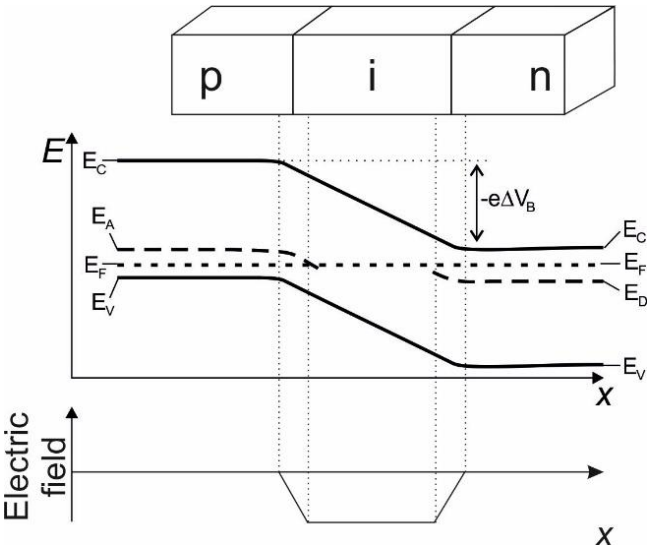

Figure 5: Band diagram for a device (e.g. 'a-Si:H' type solar cell)[4, 5] with a p-i-n junction. The electric field develops across the whole intrinsic layer, forming a constant electric field.

electrode. Under open circuit conditions, both electrodes charge up and a potential difference (open-circuit voltage V_{OC}) builds up that matches with the built-in voltage V_B. In case of closed-circuit conditions and no external load, both electrodes are directly connected, the device is shorted and a current is flowing (short-circuit current I_{SC}). However, in both cases the power output, which can be calculated as the product of the voltage times the current, is zero. To find the maximum power output and thereby the power conversion efficiency of a device, it is necessary to measure the current (I) while sweeping the voltage (V).

Characteristics of a Solar Cell An IV measurement is performed while illuminating the device with "1 sun" under air mass 1.5 (AM1.5) conditions. 1 sun thereby refers to the emission spectrum of a black body at a temperature of approximately 5800 K with an intensity of 1000 W/m², while the air mass coefficient includes the amount of wavelength dependent intensity drops on the light's intensity, due to the absorption and scattering within the earth's atmosphere. Hence, the illumination of 1 sun at AM1.5 under lab conditions resembles the realistic case. While an external voltage is applied to the device, the photocurrent is measured. With varying the external voltage up to the open circuit voltage, the full IV-curve can be recorded (Figure 6). By multiplying the current with the applied bias, the power output can be calculated and the maximum power point P_{MAX} identified.

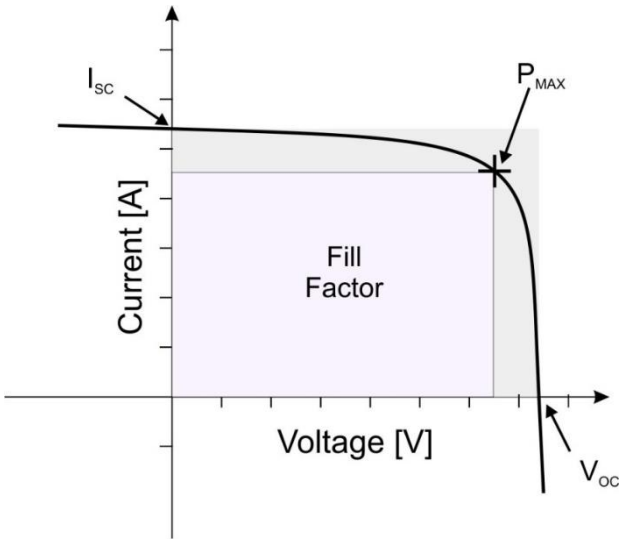

Figure 6: IV characteristics of a solar cell with the parameters short circuit current I_{SC}, open-circuit voltage V_{OC}, maximum power point P_{MAX} and the fill factor. The IV-Curve is measured in order to find the maximum power output of the solar cell and thereby the efficiency of the device.

With the maximum power point and the power input P_{IN} of the solar simulator, the power conversion efficiency (PCE) can be calculated as

$$PCE = \frac{P_{MAX}}{P_{IN}} = \frac{V_{Max} \cdot I_{Max}}{A \cdot E_E} \qquad (6)$$

whereas A is the illuminated active area of the solar cell and E_E is the irradiance of the incoming light. Another important parameter to characterize a solar cells performance and furthermore to get a number for the internal losses within the device is the fill factor (FF). The fill factor gives the ratio of the maximum power point to the highest attainable voltage (V_{OC}) and current (I_{SC}) (see Figure 6)

$$FF = \frac{V_{Max} \cdot I_{Max}}{V_{OC} \cdot I_{SC}} \qquad (7)$$

Internal losses hereby result from imperfect contacts at the interfaces, which result in a series resistance as well as shunt paths within the device and therefore additional paths for the charge carriers to move across the device.
The fact that only photons with a minimum energy above the semiconductor's band edge can contribute to the energy conversion, every solar cell system has a distinct theoretical efficiency limit connected with the illumination conditions, called the Shockley-Queisser limit.[6] Photons with lower energy E_{Ph} compared to E_G cannot participate in the energy conversion. Only photons with higher energy can excite the electron from the valence into the conduction band (hot carrier), whereas the additional energy $E = E_{Ph} - E_G$ will dissipate when the electron is transferred towards the respective electrode (Figure 7). Taking into account radiative losses, the theoretical limit for crystalline silicon with a band edge of $E_G = 1.12\ eV$ is found to be 29.8% under AM1.5 conditions.[7]

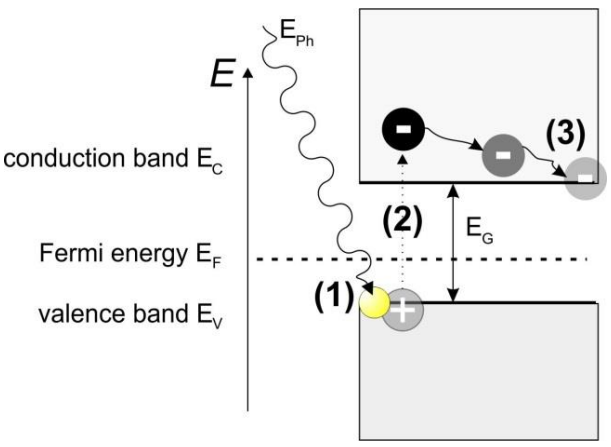

Figure 7: (1) When a photon of sufficient energy $E_{Ph} \geq E_G$ excites an electron in the valence band, (2) the electron can overcome the barrier of the band gap and jump towards the conduction band. (3) Additional energy $E = E_{Ph} - E_G$ will dissipate while the electron moves across the layer.

To optimize photovoltaics means to push the existing technology towards its theoretical efficiency limit. At the same time, it is necessary to reduce the production costs as well as the fabrication energy input. Finally, to meet new requirements for integrating photovoltaic systems into flexible, transparent or colored devices, additional challenges are faced in the development of the next generation photovoltaic device. To understand the historical background as well as the recent progress in device engineering, the next section covers the evolution of the most relevant photovoltaic technologies.

2.1.2 Emerging Photovoltaics

While the first discoveries of the photovoltaic effect and practical applications were already setup in the 19th century, the first theoretical concept of the pn-junction was introduced in 1949 by William Bradford Shockley.[8] In the following years scientist within the Bell laboratories worked on the fabrication of crystalline silicon solar cells and already achieved record efficiencies of 6% PCE in the year 1954. This was the start for the commercialization of the silicon solar cell with a design for small applications and later in 1958 also for extraterrestrial use.

In 1977 the National Renewable Energy Laboratory (NREL), located in Golden Colorado, began operating and started with systematically studying and testing efficiencies of a variation of photovoltaic device systems (Figure 8). Silicon single crystal technology started with a certified PCE of 12.5% in 1977.

The rise in efficiency exhibited a steady increase until 1994 however with no significant progress in the last 20 years. A major drawback of the silicon single crystal technology is the energy cost for growing sufficient large single crystals and

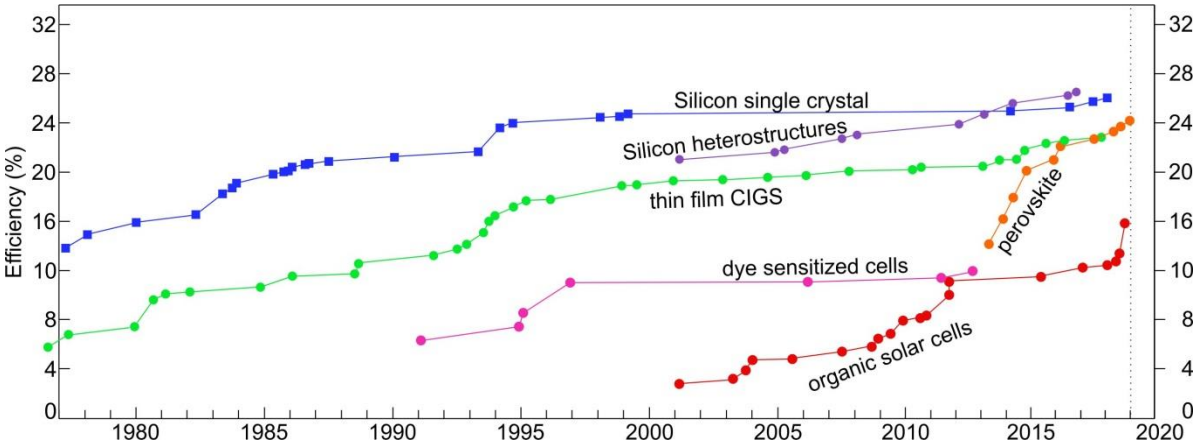

Figure 8: Solar cell efficiency chart showing the evolution of different photovoltaic systems and their certified record efficiency values from 1977 until today. The red colored toned circles represent the emerging photovoltaic systems. (Adapted from the national renewable energy laboratory (NREL) efficiency chart - http://www.nrel.gov/ncpv/images/efficiency_chart.jpg)

incorporate them into panels. Thereby the energy pay-back time of the system as well as the price of the product increases.

Later in 2001, the first PCE of a heterostructured silicon-based technology was certified (Figure 8 – purple dots). The silicon heterostructured technology combines the production of high efficiency devices and lower costs in fabrication technology, with depositing an amorphous silicon layer upon a crystalline silicon wafer.[9]

Devices which use silicon wafers as the underlying substrate are typically referred to as the first generation of solar cells. A prominent candidate of the second-generation type of solar cells is called the thin film technology-based copper indium gallium selenide solar cell (CIGS). With the advantage of a high absorption coefficient, only thin films (a few μm in thickness compared to a few hundreds of μm for the first generation of solar cells) of the materials are needed in the architecture, aiming for reduced costs and flexibility. Even though less material is needed for producing the device, the complexity within the manufacturing process still prevented the technology from accessing a bigger market.

The third-generation of solar cells are also called emerging solar cells. The first representative device structure in this segment was the dye sensitized solar cell, which had its breakthrough in 1991 with the work of Brian O'Regan and Michael Grätzel.[10]

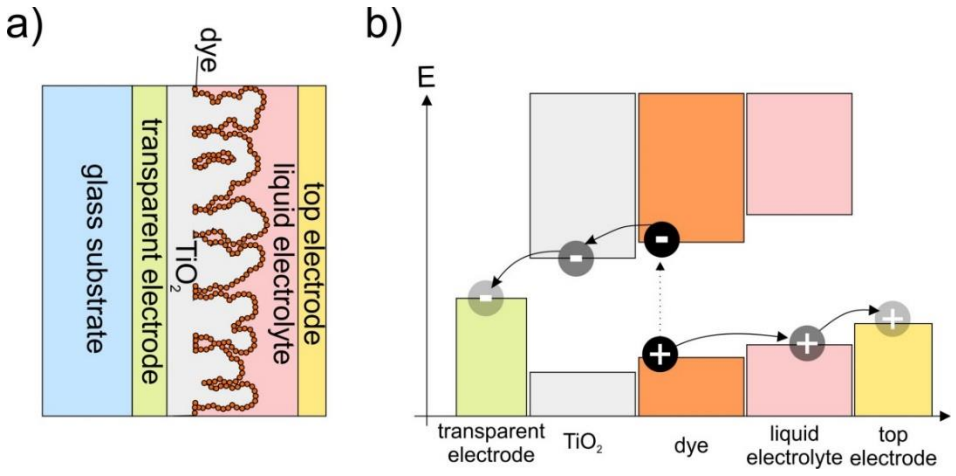

Figure 9: (a) Schematic drawing of the layer structure in a dye-sensitized solar cell. Starting from left to right with the glass substrate (blue), the transparent electrode (green), the combination of a flat and a mesoporous TiO_2 electron selective contact (grey), the nanometer sized photo absorbing dye particles (dark red), the liquid electrolyte (light red) and the reflective top electrode (yellow). (b) Schematic drawing of the energy diagram for a dye-sensitized solar cell with respective energy levels of the different layers. When light is absorbed in the photoactive dye, an electron is excited from the highest occupied molecular orbital (HOMO) into the lowest unoccupied molecular orbital (LUMO). With an energetically more favorable energy level in the conduction band of the TiO_2, the electron is injected into the TiO_2 and subsequently travels to the transparent electrode. The unoccupied state, which is left behind (hole) is subsequently filled with an electron from the liquid electrolyte. Thereby the hole is transferred from the dye to the liquid electrolyte and subsequently to the reflective top electrode.

The cell architecture consists of several layers with different functionalities, which are stacked on top of each other (Figure 9a). While a glass layer builds the substrate, two electrodes enclose the active part of the cell. This active part consists of a mesoporous TiO_2 scaffold (5-20 μm) covered with light absorbing sensitizer nanoparticles, which are anchored to the surface of the TiO_2, while a liquid electrolyte fills the whole system.[11] When a photon of proper energy is absorbed by the sensitizer dye, an electron can be excited and thereby an exciton is formed (Figure 9b). The energetic offset between the conduction bands of the dye and the TiO_2 is designed in a way to create an energetically favorable scenario for the electron to be injected into the TiO_2 and subsequently to the bottom electrode. The exciton can thereby be dissociated, with the electron extracted over the pathway towards the transparent electrode. The hole which is left behind is injected into the selective liquid electrolyte and further moves to the top electrode. Hence, the mesoporous TiO_2 scaffold was necessary to create a higher surface area and thereby a higher efficiency in dissociating excitons at the interface of the sensitizer with the TiO_2.[10] When O'Regan and Grätzel included the mesoporous TiO_2 scaffold into the dye-sensitized solar cell architecture in 1991, they received a jump in PCE from less than 1% to over 7%.[10] As a result this new device, based on low-cost fabrication techniques via solvent methods, was a promising start to build cheap devices, which have a short energy pay-back time.

Even though the community achieved promising developments within the first years after the introduction of the dye-sensitized solar cell, the PCEs did not reach a level attractive for commercial applications. Furthermore, the thermal degradation and thereby stability issues hindered devices to reasonably operate for a long time under ambient outdoor conditions.[12]

One of the most recent emerging device architectures, which aroused interest in the community for over two decades, is the organic solar cell. A complete device based on organic materials opens the door for various applications like fully printable devices on flexible substrates. Again, stability issues and the relatively low efficiency compared to commercial solar cells on the market were the downside of the technology.

To sum it up, the great hope in the third-generation of solar cells is to find a cheap and versatile alternative, which would open new fields for applications on flexible substrates or with partial transparence for an integration into windows. So far, the most dominant disadvantage of all emerging solar cells which has been discussed, is their relatively low efficiency compared with the silicon solar cell technology (Figure 8). The newest and most promising candidate of emerging photovoltaics is the perovskite solar cell.

With a steep positive slope of increasing certified power conversion efficiencies (Figure 8) the fast progress within the last six years is outstanding. Latest certified efficiencies already prove to be comparable with the Silicon based technologies. But what actually is a perovskite solar cell?

2.2. Perovskite, a "Game Changer"[13] in Photovoltaics

2.2.1 What is Perovskite?

In 1839 Gustav Rose, a German mineralogist and professor at the University in Berlin, discovered a new mineral with the chemical composition $CaTiO_3$. The calcium titanate mineral was embedded in a druse of a rock sample from Achmatowsk (Ural/Russia). He named the new mineral after the Russian politician and mineralogist Lev Aleksevich Perovski and the name "Perovskite" was born. For almost 80 years, the name was particularly connected to that specific mineral calcium titanate, until Victor Moritz Goldschmidt appeared. Between 1924 and 1926 he was the first to synthesize and study a large number of different crystals with the composition of the same ABX_3 "perovskite-type" structure.[14] From then on the name was shared for the family of materials with the perovskite-type crystal structure, as well as the composition $CaTiO_3$ itself.
The perovskite structure (ABX_3) is illustrated in Figure 10.[14] In the ideal case it has a cubic crystal structure with the A cation in the center, B cations located at the corners and corner sharing octahedrons of the X anions, surrounding the B cations.

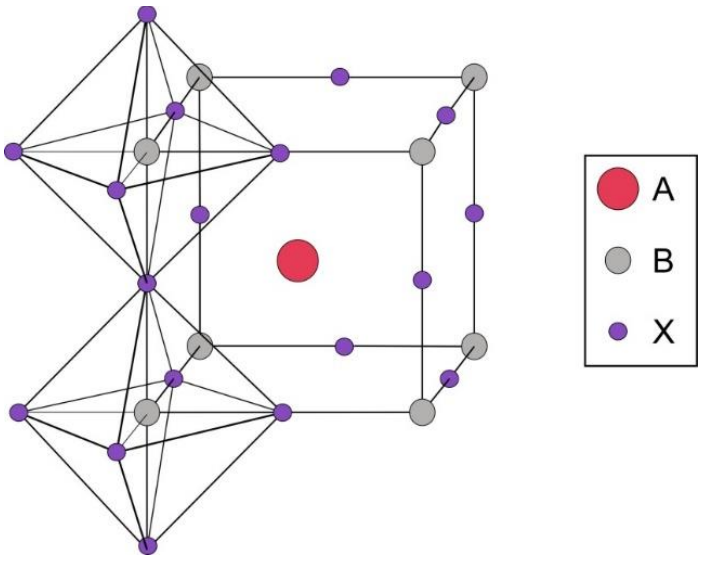

Figure 10: Sketch of the perovskite crystal structure with the cation A in the center of the unit cell and corner sharing octahedrons of the X anions around the B cations.

However, in most cases the structure is not simple cubic. Even when the structure is slightly distorted, it is regarded as a perovskite-type structure. With the help of the Goldschmidt tolerance factor t (equation 8), we can directly find and classify suitable ions which are able to arrange in the perovskite structure:

$$t = \frac{(R_A + R_X)}{\sqrt{2}(R_B + R_X)} \qquad (8)$$

With R_A, R_B and R_X indicating the radii of the corresponding ions, only tolerance factors of about 0.75-1.0 are stable in the perovskite structure. Furthermore, only tolerance factors between 0.95-1.00 are cubic, while compositions with lower tolerance factors are slightly distorted.

2.2.3 The Evolution of Perovskite Solar Cells

Based on the architecture of a dye-sensitized solar cell, Kojima et al. was the first one to use organic-inorganic hybrid perovskite nanoparticles $CH_3NH_3PbI_3$ (MAPI) as the sensitizer on top of a mesoporous scaffold of the electron transporting TiO_2 (Figure 11a).[15] The methylammonium cation ($CH_3NH_3^+$) thereby refers to the A cation in the crystal center, while the lead (Pb^{2+}) refers to the B cation and the iodide (I^-) to the X anion. Filled with a liquid electrolyte and sandwiched between a transparent and a reflective electrode, the best device of this first study reached a remarkably PCE of 3.81 %. However, the main issue with this dye-sensitized device architecture was its low stability. With the perovskite nanoparticles dissolving in the liquid electrolyte, the device only survived for a few hours. Nevertheless, as an emerging photovoltaic system a first study reaching a considerable PCE of 3.81 % was already a promising result. Though, it took two years until Im et al. showed new results with the same device configuration.[16] Concluding that the best efficiencies were attained with thinner mesoporous TiO_2 scaffolds (<4 µm), they achieved a record efficiency of 6.5% leading to subsequent systematic studies and the beginning of an optimization process in the device engineering of perovskite solar cells.

An important development came in 2012, when Kim et al. introduced a perovskite based all solid-state solar cell.[17] While the rest of the device architecture remained unchanged, the liquid electrolyte was exchanged with a solid-state organic hole transporter (spiro-MeOTAD). The use of the solid spiro-MeOTAD on top of the perovskite nanoparticles led to a record efficiency of 9.7 % and an increase in stability (>500 h).[17] With a band gap of E_g=1.5 eV the light absorbing perovskite proved to be the perfect match for the spectrum of the sun[17]. With this improvement, the solid-

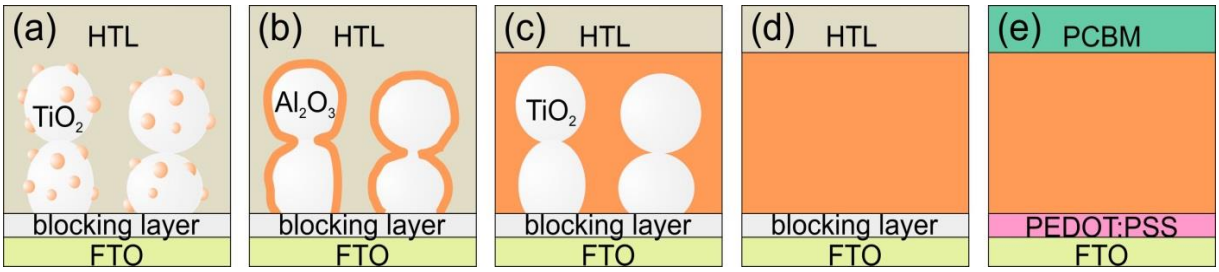

Figure 11: Different device configurations for perovskite solar cell architectures. a) Dye-sensitized approach, with perovskite nanometer sized particles anchored to the mesoporous TiO_2 particles, surrounded by the hole transporting layer (HTL). b) Super-mesostructured device architecture with a mesoporous Al_2O_3 scaffold, which is covered by the perovskite. c) Mesostructured device architecture with a scaffold of mesoporous TiO_2 and perovskite filling the mesoporous structure with an additional perovskite capping layer on top. d) Flat-junction or planar device architecture with a flat layer of perovskite between the selective contacts. e) "Inverted" device architecture with organic selective contacts, while the hole selective contact is on the bottom and the electron selective contact is on top.

state device architecture became the predominant perovskite solar cell configuration. Advantages in the fabrication and an increase in device stability, created new ideas for further systematic studies. For example, Etgar et al. showed that it is possible to build a working device with the complete removal of the additional hole transporter.[18] Under standard conditions this device showed a PCE of 5.5 %, proving that the perovskite $CH_3NH_3PbI_3$ can act both as the photo absorber and the hole conductor. Next, Lee et al. showed that it is also possible to keep the functionality of a device, when replacing the electron-accepting scaffold of TiO_2 with an insulating scaffold of Al_2O_3.[19] Whilst replacing only the mesoporous part of the device, the interface between the photo absorbing perovskite ($CH_3NH_3PbI_2Cl$) and the electron accepting TiO_2 was dramatically reduced to the interface where perovskite covered the bottom TiO_2 contact (Figure 11b). The so-called super-mesostructured device still showed a remarkable PCE of 10.9 % and an open-circuit voltage of more than 1.1 volts, questioning the role of the perovskite as simply being a sensitizer for the mesoporous electron accepting TiO_2. With an absorption onset of 800 nm they assumed the band gap of the absorbing perovskite material to be E_g=1.55 eV, and could finally conclude, that the energy loss inside the device is at a minimum level. The conclusion of these two studies led to the suggestion that the perovskite material exhibits ambipolar charge transport behavior. To receive a sufficient PCE, it is neither necessary to have an additional hole transporting material, nor a large interfacial area between the perovskite and the electron acceptor. The latter conclusion also led to the fabrication of efficient planar heterojunction perovskite solar cells.[20] When Ball et al. stepwise reduced the thickness of the mesoporous scaffold of Al_2O_3, an additional thin perovskite layer (capping layer) formed on top of the scaffold (Figure 11c).

With completely removing the mesoporous scaffold, the "flat-junction" device architecture (Figure 11d) still delivered PCEs of up to 9.1%. Flat-junction devices are of high interest as they benefit from the ease of fabrication with a reduced processing temperature compared to the mesoporous devices, making them processable via printing techniques. However, the major challenge with the solution processed "flat-junction" devices is the controlled growth of the perovskite crystals.[21] While the solution processed method produces large crystals (>1 μm), the layer thickness is inhomogeneous, which can result in direct contacts (pinholes) between the electron and the hole transporting layer. Such pinholes create a shunting path, which can reduce the fill factor and hence the open-circuit voltage. By using a dual source thermal evaporation system, Liu et al. could simultaneously deposit the organic and inorganic components to receive a homogenous perovskite layer on top of the compact TiO_2.[21]

In comparison with the solution processed films, the vapor deposition produced smaller crystal sizes (>100 nm), which resulted in the controlled growth of the perovskite layer. With a homogeneous film thickness of 330 nm, they received record efficiencies of over 15%.[21] Besides the progress in the device fabrication process, Liu et al. could also draw an important conclusion from their studies of the "flat-junction" on the charge transport mechanism.[21] In order to gain sufficient charge extraction, the diffusion length of the free hole/electron has to be long enough to reach the corresponding selective interface. Assuming that the exciton is dissociated at one of the selective interfaces, the corresponding lower limit of the other species diffusion length must be the film thickness with at least 330 nm. Soon other studies confirmed this conclusion, showing that the charge diffusion lengths in perovskite films are up to several hundreds of nanometers.[22, 23] Furthermore, it turned out that free charges are already present within the perovskite itself.[24] Using transient THz spectroscopy Wehrenfennig et al. could observe characteristic shapes of the transient, incompatible with excitonic absorption.[24] Later on, Miyata et al. used high-field interband magneto absorption to reveal an exciton binding energy of a few millivolts concluding that free charge carriers are generated through thermal dissociation already at room temperature ($k_BT = 26\ meV$).[25] Without the necessity of dissociating excitons at a selective interface, the advantage of an increased area of the perovskite-electron acceptor interface remained questionable. However, devices with the mesoporous scaffold of TiO_2 resulted in higher efficiencies and thereby set the benchmark for perovskite solar cells.[26]

Furthermore, the combination of a mesoporous scaffold of TiO_2 filled with the perovskite absorber and an additional compact perovskite capping layer on top proved to be the most efficient device architecture.[27] Up until now the combination of

mesoporous electron transport layer, with a perovskite capping layer on top is leading in the run for the record of power conversion efficiency exceeding 20% [28, 29] with a current leader of >24%.[30] The latest progress in the fabrication of devices with up to date highest efficiencies is the intermixing of methylammonium/formamidinium (MAI/FAI) as the organic cations and iodide/bromide as the halides to form the compositional mixed-cation perovskite crystal structure.[28, 31, 32] Furthermore, Bi et al. added the polymer (poly(methyl methacrylate), (PMMA)) for a controlled growth of the perovskite crystals and thereby produced smooth films with reduced pinholes resulting in reduced charge recombination.[28]

Within six years, from the first systematic optimization studies in 2012 until now, the perovskite solar cell reached a record efficiency which is comparable to the silicon-based market leading technology. According to the Shockley-Queisser theory,[6] the optimum bandgap of the perovskite materials (for $CH_3NH_3PbI_3$ ~1.5 eV [33]) even gives a theoretical efficiency limit of over 30%.[34] Industrial upscaling of the device architecture could make the perovskite solar cell a future competitor to the silicon solar cell or by combining both systems in a tandem cell, even a partner for the technology used in today's photovoltaic market.

However, there are still multiple challenges to face like an uncontrolled reproducibility in fabrication,[35] stability issues[36-39] or the hysteresis in current-voltage characteristics.[40, 41] All these major issues emphasize a crucial upshot, that various details about the underlying device physics of perovskite solar cells still remain unclear. One of the most prominent examples of the last years, which reveals the open questions about the device physics more than any other, is the hysteresis in the current-voltage characteristics.[40, 41]

2.2.4 Hysteresis

Usually a current-voltage scan is performed starting from above the open-circuit voltage all the way to below 0 V (backward scan) and subsequently from below 0 V back to the initial value (forward scan). However, for perovskite solar cells it turned out that for most of the scan conditions the forward and backward curves did not overlap (Figure 12). A systematic hysteresis was measured, which depends on various parameters like scanning speed, scanning range, scanning sequence, illumination time, temperature, device degradation and device architecture.[40-45]

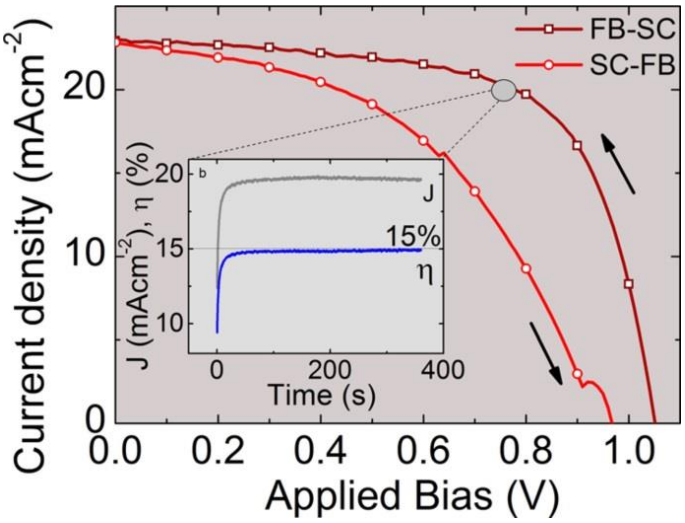

Figure 12: JV-Curve showing the "Anomalous Hysteresis in Perovskite Solar Cells" for a super-mesostructured Al_2O_3 device, starting with the backward scan and subsequently performing the forward scan. The backward scan shows significantly more current output than the forward scan. The inset shows the stabilized current output and the stabilized efficiency against time. "Reprinted with permission from (J. Phys. Chem. Lett. 2014, 5 (9), 1511-1515.). Copyright (2014) American Chemical Society." [40]

The most distinct hysteresis was found in the planar device architecture with TiO_2 compact layer. In comparison the hysteresis in mesostructured TiO_2 based devices were found to be less pronounced and almost negligible for inverted devices (with fullerene as the organic selective contact; "hysteresis free").[40, 46]

O'Regan et al. described the hysteresis more general with the concept of a device preconditioning.[44] A preconditioning scenario could be an applied bias or a previous illumination of the device. The resulting preconditioning state of the device is also time-dependent. For a JV-scan this includes the scanning speed, scanning range, scanning sequence and illumination time. More general the actual state of the device depends on the device history. Depending on the history of the device, the current-voltage dependency can be changed (compared to a device coming from equilibrium) and have an effect on the current output under an externally applied bias. If a device is preconditioned under illumination and with applying an external voltage V_{prec} with $V_{prec} > V_{OC}$ and then subsequently measured at the maximum power point, it will show a current transient, which decays in the time scale of seconds.[44] The device is thereby preconditioned in a way which gives a higher current response than in the steady state. Furthermore, such a preconditioned device has a higher efficiency for the backward scan in a JV-curve. The dependency of the scanning rate is directly correlated to the relaxation process, which is observed in the steady state measurement.

If an external voltage $V_{prec} > V_{OC}$ is applied and then subsequently a fast backward scan (1 V/s) performed, the maximum apparent efficiency is measured. The opposite happens if the scan is started at short circuit conditions without any preconditioning. After a fast forward scan (1V/s) the minimum apparent efficiency is measured. A long-term measurement however, with the applied voltage, determined from the maximum power point, results in a saturation of the current and the steady-state output is measured.

Additionally, Bryant et al. observed that the hysteresis of an actual "hysteresis free" device can be significantly pronounced, when cooling the device to low temperatures.[43] The underlying relaxation process is slowed down ($0.6\ s \rightarrow 15.15\ s$) at low temperatures ($298\ K \rightarrow 175\ K$). Furthermore, the device can be "frozen" at the most favorable condition, when preconditioning the device under a forward bias of 1.2 V while cooling it to 77 K. The conclusion of their study was that the underlying processes are not removed or suppressed for device architectures with less hysteresis, but the time-dependency of the underlying process is shifted and thereby does not affect the JV-scan anymore.

Another significant observation about an exception of the direction for hysteresis was made by Tress et al..[45] For some of the mixed cation perovskites (FAI/MAI) the forward scan of the JV-scan showed a higher efficiency than the backward scan. Preconditioning the device with a bias $V_{prec} > V_{OC}$ thereby led to a lower current output, compared with the steady state value, which was named "inverted hysteresis".

Summing up, the measurements of device performance for preconditioned perovskite solar cells can lead to false conclusions. Furthermore, by taking advantage of the hysteresis, a measurement protocol can be optimized in order to make a bad cell look good. Hence, it is necessary to perform a measurement based on a standard measuring protocol for consistent and comparable PCE values.[47]

Equally it is important to identify the underlying mechanisms which cause the hysteresis, in order to get a fundamental understanding. The device performance could then be optimized by regulating internal processes of the preconditioning state, similarly to the method used by Bryant et al. when "freezing" the most favorable condition.[43]

Since the first study which reported about the observation of the hysteresis, three major suggestions about the underlying mechanisms of the hysteresis were made:[40]

(1) A large defect density resulting in trap states and/or interfacial defects. When applying a bias and/or illuminating the device these trap states are filled, resulting in optimized charge extraction at the interfaces, while under short circuit conditions traps are emptied.
(2) The perovskite material exhibits a ferroelectric property, which can be switched under the influence of an electric field.
(3) Mobile ions or vacancies are able to migrate through the device under the influence of an electric field.

In order to systematically study and identify the underlying mechanism of the hysteresis, one needs to measure internal processes of the device to answer the following open questions:

- How does the internal electric field look like?
- How does it change from one device architecture to the other?
- What is the effect of light illumination?
- Are there any space charge regions/accumulated charges within the device?
- Can we localize any trap states within the device?
- How does an external bias affect the internal electric field?
- How does the charge distribution change in time under operating conditions?

The systematic differences in the strength of hysteresis between the various device architectures already leads to the conclusion that the underlying mechanisms originate at the internal interfaces.

In order to study internal processes within a perovskite solar cell device and answer the questions named above, it is necessary to find the proper characterization method. The field of perovskite solar cells thereby benefited from the previous extensive studies on dye-sensitized and organic photovoltaics. Measurement techniques which had previously been optimized in these fields helped to gain a rapid increase of knowledge and the fast development of perovskite solar cells. In following, techniques are presented which are frequently used in order to systematically study photovoltaic devices. Furthermore, we will focus on the advantages and disadvantages of these techniques when making use of these to take part in the process of answering the open questions mentioned above.

2.2.5 Techniques for Characterization

From a simple IV-setup, the time dependent response of the current can be measured, when systematically applying external biases while illuminating with a light source. Time constants of decay processes can be analyzed by checking the transients of the open circuit voltage or the short circuit current.[44] Thereby, we can already get an idea about the timescales as well as different processes for a complete device. However, we are not able to correlate the processes with their exact location and thereby we cannot localize and distinguish these processes.
So far, following advanced methods have been used to get more detailed information about the general device physics or even separately localized processes:

Impedance Spectroscopy (IS) became one of the most powerful techniques for characterizing dye-sensitized solar cells. A device is thereby connected to an electrical circuit. While an AC voltage, $\hat{V}(\omega)$, with an angular frequency ω is applied to the system, the resulting AC Current, $\hat{I}(\omega)$, is measured. By varying ω and calculating the Impedance

$$Z(\omega) = \frac{\hat{V}(\omega)}{\hat{I}(\omega)} \qquad (9)$$

the dependency of the Impedance with respect to the frequency can be studied. With an exact physical model of the system, the shape of the curve gives information about the physical processes within the device. In such a physical model the device is composed of resistors, capacitors, etc. which represent the interfaces, recombination channels, etc.. Characteristics in the impedance-frequency dependency can thereby be correlated with the electrical components of the model.
However, the fundamental approach to study a system with IS, is the existence of the exact model for the system.[44] Furthermore, the model neglects the surface roughness of the interfaces, which ends in simplified conclusions for local processes.

Photoluminescence Spectroscopy (PL) is a common technique to study electronic processes within the photoactive film, by detecting the time-dependent emission of the recombination. A short light pulse creates excited states, which subsequently recombine. With the information about the diffusion constant, the time constant of the decay process gives the diffusion length.[22]
By comparing different combinations of stacked layers, e.g. quenching the photoexcitation with a selective interface, recombination is suppressed and the mobility of different charge species can be separately identified.

Furthermore, the combination of a confocal PL and a scanning electron microscope (SEM) can be used to study the structure function relationship.[48] Thereby, it is possible to scan the surface and correlate the film morphology with the recombination decays.
However, PL measurements are restricted to the detection of radiative decay processes and thereby cannot detect non-radiative processes, neither localize accumulated charges. Furthermore, the resolution is limited to the beam width.

Transient-Absorption (TA) is used to study the evolution and decay of fast electronic processes. In TA measurements first, an ultrafast laser pulse (pump) is used to initiate excited states within the sample and a second laser pulse (probe), to detect the time dependent changes in absorbance. The time dependent difference between the excited and the initial absorbance

$$\Delta A(t) = A_{Probe}(t) - A_{Pump} \qquad (10)$$

gives information about the evolution of the electronic processes in the photoactive material, e. g. further excitation of already excited states. Thereby even non-radiative relaxation processes and lifetimes can be studied. By varying the wavelength, the complete spectrum of processes can be mapped.
However, local information about the distribution of charges at interfaces and the processes under working conditions for complete devices cannot be covered with this technique.

Electron-Beam-Induced-Current (EBIC) uses a focused electron beam to locally excite electrons within the device, which leads to charge dissociation and transfer to the respective electrode. Thereby the surface is scanned and the resulting current is mapped. By applying the technique to the cross section of a device, the relation of effective charge dissociation over the complete thickness of the photoactive layer can be studied.[5, 49] This relation gives local information about the transport mechanism inside the device.
However, the method is dependent on a flowing current and can only simulate "operating" conditions. Furthermore, the consequences of side effects, caused by the electron beam excitation, remain unclear.

All of the above-mentioned techniques can be used to study open questions about the device physics for photovoltaic devices. However, none of the above-mentioned techniques has a direct access to the distribution of the local potential within a

device. In order to answer the questions, which were raised in the hysteresis-section (2.2.4), it is necessary to use a technique which can locally study the topography and the electrostatic properties at the same time. **Scanning-Probe-Microscopy (SPM)** is known to be an effective tool, to image surfaces on the nanometer scale, and characterize features such as topography, mechanical, magnetic, electrostatic or piezoelectric properties. With the **Kelvin-Probe-Force-Microscopy (KPFM)** technique, which is sensitive to the contact potential difference (CPD), it is possible to locally resolve the electrostatic interaction between a reference probe (cantilever) and the surface underneath, while at the same time map the topography. The method is thereby a perfect candidate to characterize a device concerning the open questions about the internal electrical processes. In the next chapter, I will focus on the evolution and the experimental details of KPFM and the setup, which I optimized and used during my thesis to study internal electric process in perovskite solar cells and correlate them to the interfaces of the device.

3. Experimental

"If we knew what it was we were doing, it would not be called research, would it?"
— Albert Einstein

3.1. Scanning Probe Microscopy

The successful story of microscopy methods based on probe-sample interaction started with the invention of the scanning tunneling microscope (STM) by Binning et al. in 1982.[50] In STM the sample is scanned by the measuring probe, while a feedback regulates the probe-sample distance in order to keep a defined tunneling current under a constant externally applied bias. The method proved to be so powerful that four years later, Gerd Binnig and Heinrich Rohrer received the Nobel Prize in Physics for their work on the STM. A drawback of the STM was that it could only measure the morphology of conductive samples. To overcome this limitation, the underlying principle of the probe-sample feedback loop inspired the scientific community to develop a variety of methods, which were sensitive to different probe-sample interactions.

By transferring the scanning principle of the STM onto measuring the mechanical force between the probe and the sample, Binning et al. developed the atomic force microscope (AFM) in 1985.[51]

3.2. Atomic Force Microscopy

The atomic force microscope is sensitive to forces on a nanometer scale. With the help of a needle shaped tip at the end of a cantilever arm (Figure 13), the morphology of surfaces can be scanned. A direct approach of using the repulsive force of the tip in contact with the surface is called "static mode". In static contact mode the tip is brought into contact with the surface, causing a deflection of the cantilever arm. With a laser-deflection system, the elongation of the cantilever can be recorded by a photodetector. While the sample is scanned in the xy-plane, a feedback mechanism regulates the height in z-direction in order to keep a constant force of the tip acting on the surface. By recording the adjustment of the z-height, the topography of the surface can be mapped during the scan. A major drawback of the contact mode is that the constant interaction force during the scan can cause damage to the surface structure and the tip. A way to reduce the tip-sample damage is to use the "dynamic mode".

In dynamic mode, the cantilever is excited at its resonance frequency, while a lock-in amplifier detects the amplitude and the phase shift of the detection signal for the oscillation. The motion of the cantilever can be described by a forced harmonic oscillator with damping: [52]

$$F_{dr}\cos(\omega t) = m\ddot{z} + \frac{m\omega_0}{Q}\dot{z} + kz \qquad (11.1)$$

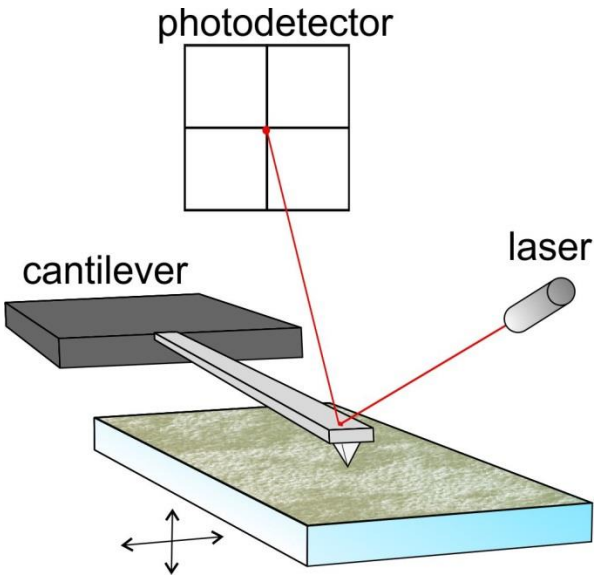

Figure 13: Atomic force microscopy basic working principle. By focusing a laser on the backside of the cantilever arm with the needle shaped tip underneath, the interaction between the tip and the sample can be measured with the deflection detected by the photodetector.

with the driving Force F_{dr}, excitation frequency ω, spring constant of the cantilever k, eff. mass of the cantilever m, resonance frequency of the cantilever ω_0 and the quality factor Q. After an intermediate state of motion, the amplitude of the oscillating cantilever $A(\omega)$ can be described by the steady state solution of equation 11.1:

$$A(\omega) = \frac{\frac{F_{dr}}{m}}{\sqrt{\left[\left(\omega_0^2 - \omega^2\right)^2 + \left(\frac{\omega\omega_0}{Q}\right)^2\right]}} \tag{11.2}$$

When bringing the oscillating cantilever in close range to the sample surface, the tip-sample interaction results in an additional force on the cantilever F_{TS}. The influence of F_{TS} results in an additional term in the effective cantilever spring constant k_{eff} and thereby a shift of the cantilever resonance frequency (linear approximation for small amplitudes).

$$k = -\frac{\partial F}{\partial z} \Rightarrow k_{eff} = -\left(\frac{\partial F}{\partial z} + \frac{\partial F_{TS}}{\partial z}\right) \tag{11.3}$$

$$\omega_{eff} = \sqrt{\frac{k_{eff}}{m}} = \sqrt{\frac{k - \frac{dF_{TS}}{dz}}{m}} \tag{11.4}$$

By adjusting the height in order to keep a constant oscillation amplitude (amplitude-modulation AFM) or adjusting the height in order to keep a constant resonance frequency shift (frequency-modulation AFM) the height information can be used to

map the topography of the surface. Local material contrast, even though exhibiting the same height profiles, can be detected with the phase shift between the excitation and the detection signal.

$$\phi = \arctan\left(\frac{\frac{\omega\omega_0}{Q}}{\omega_0^2-\omega^2}\right) \tag{11.5}$$

Instead of the local mechanical force and the resulting interaction of the tip-sample system, other interaction forces can be triggered as well to measure surface properties with the AFM technique.

3.3. Kelvin Probe Force Microscopy

The early days of scanning probe microscopes (SPM) was dominated by researchers in the company of "Internal Business Machines Corporation" (short IBM). While the STM was developed at IBM Zürich[50] and the AFM in a collaboration of Stanford University (former IBM co-worker) and IBM San José,[51] a group in IBM Yorktown Heights focused on the development of more advanced force microscopes.[53, 54] In 1987 the group around Kumar Wickramasinghe developed an SPM to image the magnetic properties of a surface with 100 nm resolution.[53] In the following year the same group reported on an SPM to image surface electric properties.[54] By applying an AC voltage to the tip which is positioned a few nm above the surface, the electrostatic force leads to an oscillation of the cantilever. With the feedback adjusting the tip-sample distance in order to keep the oscillation amplitude constant, Martin et al. could image a sample with respect to the tip-sample capacitive gradient.[54] However, in order to make quantitative measurements, the system needed to be improved.

With the development of Kelvin probe force microscopy (KPFM), it became possible, to study the surface potential quantitatively on a nm scale, based on the local contact potential difference.[55]

3.3.1 Basics

Contact Potential Difference (CPD) The CPD between two materials is generated, whenever two materials are brought into electrical contact. After contact, charge carriers transfer at the interface in order to align their fermi levels (Figure 14).

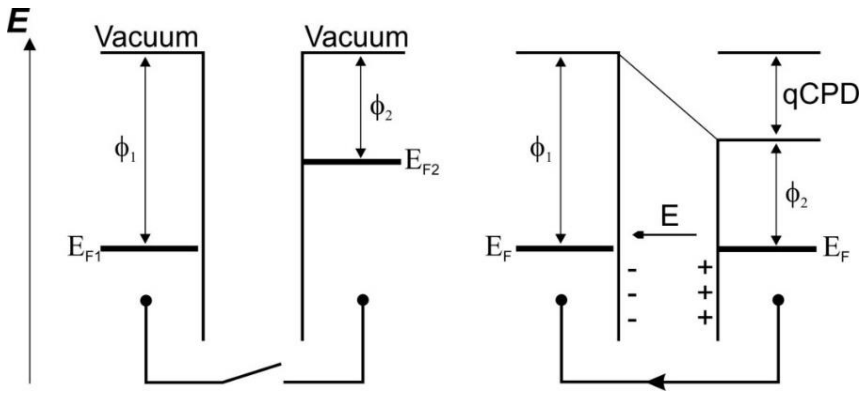

Figure 14: Energy diagram of two materials, showing the respective contact potential difference. When the materials are brought into contact, charges will transfer in order to align the fermi levels E_F. While the work functions stay constant, the vacuum level shift exhibits the contact potential difference.

Since the difference between the fermi and vacuum level has to stay constant, the alignment results in a shift of the respective vacuum levels (Figure 14). In case of a KPFM experiment the resulting voltage, which matches the contact potential difference U_{CPD}, represents the difference in work function ϕ between tip and sample:

$$q \cdot U_{CPD} = \phi_1 - \phi_2 \Longrightarrow U_{CPD} = \frac{\phi_{sample}}{e} - \frac{\phi_{tip}}{e} \tag{12}$$

Kelvin Method By using the Kelvin method, the CPD between two materials can be measured. With the setup of a plate capacitor, where two plates are being separated by a small distance d, charges will transfer in order to create the fermi level alignment. By vibrating one of the plates with a small amplitude *a*, the distance and thereby the capacity between the plates changes accordingly:

$$C = \varepsilon_0 \frac{A}{d + \mathrm{acos}\,(\omega t)} \tag{13}$$

Thereby the CPD leads to an alternating current in the electric circuit:

$$I(t) = \frac{dQ}{dt} = \frac{d}{dt}(C \cdot U_{CPD}) = U_{CPD}\frac{dC}{dz}\frac{dz}{dt} = U_{CPD}\frac{dC}{dz}\omega \cdot a \cdot \sin(\omega t) \tag{14}$$

With an external bias applied to the system, the potential difference between the plates can be nullified and the current becomes zero:

$$I(t) = (U_{CPD} - U_{DC})\frac{dC}{dz}\omega \cdot a \cdot \sin(\omega t) \tag{15.1}$$

When the current becomes zero the external bias U_{DC} equals U_{CPD} and therefore the CPD.

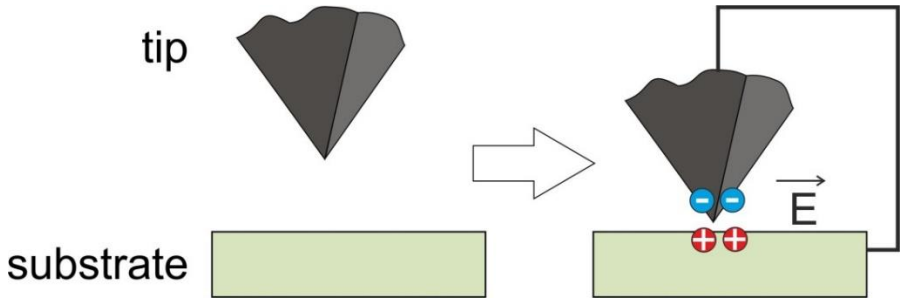

Figure 15: The CPD builds up when the tip and the sample are connected, resulting in an electric field, an electrostatic force and thereby a deflection of the cantilever arm.

Kelvin Probe Force Microscopy For KPFM the principle of the Kelvin method gets integrated into a scanning probe microscopy setup.

When the tip is brought close to the sample surface, the CPD creates an exchange of charges through the electrical connection. With a potential difference between tip and sample U_{CPD}, an electric field E and consequently an electrostatic force F_{el} is created (Figure 15):

$$F_{el} = -\frac{\partial E}{\partial z} = -\frac{1}{2} U^2 \frac{\partial C}{\partial z} \tag{16}$$

Besides the intrinsic U_{CPD}, an external voltage $U = U_{DC} + U_{AC}$ is applied to the tip, resulting in the oscillation of the cantilever.

$$U = U_{CPD} + U_{DC} + U_{AC} \cdot \sin(\omega t) \tag{17}$$

$$F_{el} = F_{stat} + F_{\omega} + F_{2\omega} \tag{18}$$

$$F_{stat} = -\frac{1}{2}\frac{\partial C}{\partial z}\left[(U_{CPD} + U_{DC})^2 + \frac{{U_{AC}}^2}{2}\right] \tag{18.1}$$

$$F_{\omega} = -\frac{\partial C}{\partial z}[(U_{CPD} + U_{DC}) \cdot U_{AC} \sin(\omega t)] \tag{18.2}$$

$$F_{2\omega} = \frac{1}{4}\frac{\partial C}{\partial z}\left[{U_{AC}}^2 \cos(2\omega t)\right] \tag{18.3}$$

The idea to identify the CPD is to apply a DC bias U_{DC} of the same magnitude, but different sign and thereby nullify the force F_{ω} which alternates with $\sin(\omega t)$. The technical implementation to measure the CPD and scan the surface at the same time can be achieved via different lock-in feedback routines.

3.3.2 AM-/FM-KPFM

Amplitude-Modulation KPFM (AM-KPFM) In AM-KPFM the amplitude of the deflection signal at the excitation frequency ω serves as the reference feedback signal to nullify the force F_ω and thereby to identify the CPD.

The most commonly implemented AM-KPFM routine in commercial AFM's is a dual pass technique. In dual pass the scan to measure the topography and the scan to measure the CPD are seperated. In two separate scans, the excitation is performed for both the mechanical and electrical modulation at the cantilever's resonance frequency ω_{Res} to reach the maximum amplification of the signal. In a first scan the morphology is measured, while in a second scan the cantilever follows the height profile with a constant distance above the sample surface to detect the CPD.

A different routine for AM-KPFM is to perform and readout the mechanical excitation at the first resonance and generate the electrical excitation at the second resonance (or off resonance) at the same time (single pass).[56]

Frequency-modulation KPFM (FM-KPFM) The most common routine under ambient conditions to perform FM-KPFM is the sideband modulation technique. In following, the formation of these modulation sidebands is explained.

In sideband modulation FM-KPFM the cantilever is mechanically excited at its resonance frequency ω_{Res}, while additionally an AC voltage is applied to the tip at a modulation frequency ω_{mod} . The additional electrostatic force at ω_{mod} causes a shift of the cantilever's effective resonance frequency ${\omega_{Res}}^*$ given by:

$$ {\omega_{Res}}^* = \sqrt{\frac{k - \frac{\partial F_{el}}{\partial z}}{m_{eff}}} \tag{19} $$

with k being the spring constant and m_{eff} being the effective mass of the cantilever. For small modulations we get:

$$ {\omega_{Res}}^* \approx \omega_{Res}\left(1 - \frac{1}{2k}\frac{\partial F_{el}}{\partial z}\right) \tag{20} $$

Accordingly, the electric force gradient for F_ω (equation 18.2) causes an oscillating shift of the effective resonance frequency with the modulation frequency ω_{mod}:

$$ {\omega_{Res}}^*(t) = \omega_{Res} - \underbrace{\frac{1}{2k}\frac{\partial^2 C}{\partial z^2}(U_{CPD} - U_{DC})U_{AC}}_{\omega_p}\cos(\omega_{mod}t) \tag{21} $$

with ω_p being the peak of the frequency deviation of the oscillating resonance frequency shift. For the time dependent effective resonance frequency, the amplitude of the oscillating system can be described by:

$$s(t) = A\cos(\int {\omega_{Res}}^* \, dt) = A\cos\left[\omega_{Res}t + \underbrace{\left(\frac{\omega_p}{\omega_{mod}}\right)}_{h}\sin(\omega_{mod}t) + \varphi\right] \tag{22}$$

With the addition theorem for the cosine we get:

$$s(t) = A\cos(\omega_{Res}t)\cdot\cos(h\cdot\sin(\omega_{mod}t)) - A\sin(\omega_{Res}t)\cdot\sin(h\cdot\sin(\omega_{mod}t)) \tag{23}$$

We can now build a function $\tilde{s}(t)$ with $s(t)$ being the real part of the function:

$$\tilde{s}(t) = A\cdot f(t)\cdot\exp(i\omega_{Res}t) \tag{24.1}$$

$$f(t) = \exp\,(ih\cdot\sin\left(\underbrace{\omega_{mod}t}_{\tau}\right)) \tag{24.2}$$

Since $f(\tau)$ is a periodic function, we can expand it in a Fourier row:

$$f(\tau) = \sum_{n=-\infty}^{\infty} C_n \exp\,(in\tau) \tag{25.1}$$

with the coefficients:

$$C_n = \frac{1}{2\pi}\int_{-\pi}^{\pi}\exp\,(ih\cdot\sin(\tau))\cdot\exp(-in\tau)\,d\tau \tag{25.2}$$

$$= \frac{1}{2\pi}\int_{-\pi}^{\pi}\exp\,(-i(n\tau - h\cdot\sin(\tau))\,d\tau \tag{25.3}$$

With a transition $\tau \to -\tau$ the coefficients equal the integral presentation of the Bessel functions and we get:

$$\tilde{s}(t) = A\cdot\sum_{n=-\infty}^{\infty} J_n(h)\cdot\exp\,(in\omega_{mod}t)\cdot\exp\,(i\omega_{Res}t) \tag{26}$$

For small h we can stop the Fourier row from $|n| > 1$ and receive for the real part of $\tilde{s}(t)$:

$$\begin{aligned} s(t) = A \cdot J_0(h) \cos(\omega_{Res} t) \\ + A \cdot J_1(h) \cos\big((\omega_{Res} + \omega_{mod})t\big) \\ + A \cdot \underbrace{J_{-1}(h)}_{-J_1(h)} \cos\big((\omega_{Res} - \omega_{mod})t\big) \end{aligned} \quad (27)$$

While $s(t)$ represents the amplitude of the oscillating system, we see that the modulation frequency results in additional peaks at $\omega_{Res} + \omega_{mod}$ and $\omega_{Res} - \omega_{mod}$ (sidebands). In order to measure the CPD, the feedback mechanism in FM-KPFM takes the amplitude of the sidebands as the feedback reference. When applying a DC voltage of same magnitude like the CPD, the oscillating shift in the effective resonance frequency vanishes (equation 21) and thereby the amplitudes of the sidebands get nullified.

Although the FM-KPFM method is technically advanced and mostly not implemented in commercial systems, it reveals an important advantage compared to the AM-KPFM method. The modulation sidebands appear due to the electrically modulated oscillation of the mechanically excited resonance frequency. The shift of the resonance frequency changes with the electrical force gradient (eq. 20). By regulating the modulation sidebands with the DC voltage, the feedback of the FM-KPFM method is sensitive to the electrostatic force gradient $\left(\frac{\partial F_{el}}{\partial z} \sim \frac{1}{z^3}\right)$. In comparison, the feedback of the AM-KPFM method directly regulates the feedback on the amplitude of the electrostatic force $\left(F_{el} \sim \frac{1}{z^2}\right)$.

The faster decline of the electrostatic force gradient compared to the electrostatic force itself, results in a higher lateral resolution for FM-KPFM (~50 nm), while AM-KPFM measurements suffer from an averaging effect over larger areas due to cantilever-surface crosstalk (Figure 16).[57-62]

I therefore chose to use FM-KPFM for my measurements. In order to highlight the necessity of using FM-KPFM, I will compare results from both methods in the last section of the results chapter (4.5).

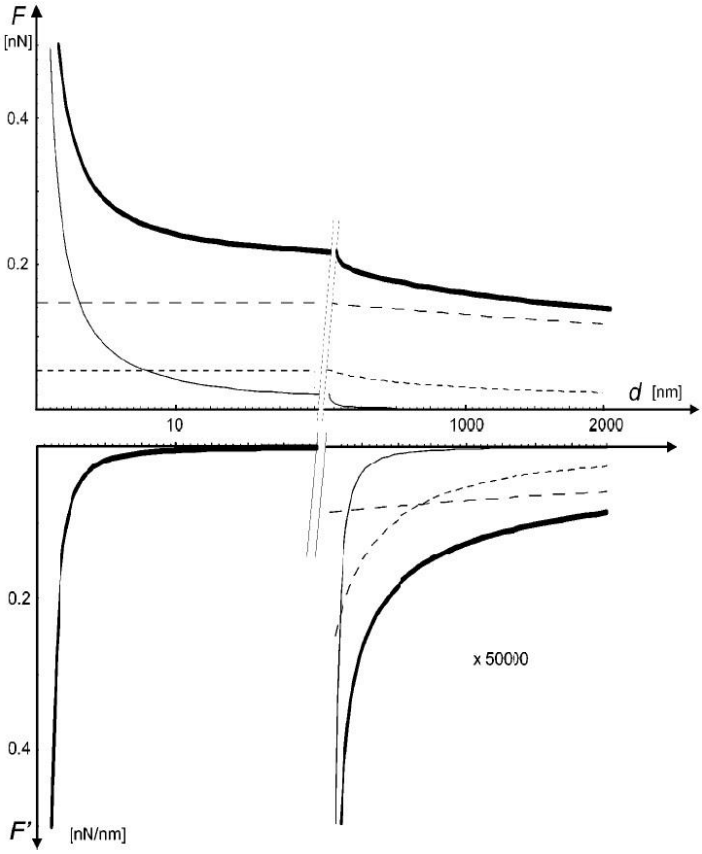

Figure 16: (top) Electrostatic force between a typical KPFM cantilever and a flat metallic surface as a function of tip-sample distance. The thick line corresponds to the total force, while the thin line represents the contribution of the tip apex, the long-dotted line represents the contribution of the cantilever and the short-dotted line represents the contribution of the tip cone. The contribution of the tip apex becomes dominant for distances <5 nm. (bottom) Electrostatic force gradient between a typical KPFM cantilever and a flat metallic surface with the same specifications. The lines represent the same contributions as in the upper part. For the electrostatic force gradient, the contribution of the tip apex becomes dominant for distances <50 nm. As a typical KPFM measurement in air is performed with oscillation amplitudes >> 5 nm (in our case ~70 nm), the contribution of the cantilever and the tip cone leads to an averaging effect when using AM-KPFM (crosstalk). "The figure is adapted with permission from (Phys. Rev. B 2001, 64 (24), 245403.). Copyright (2001) American Physical Society."[57]

Still, Kelvin probe force microscopy is a surface sensitive technique. In order to receive information about the distribution of charges within a closed device structure it is necessary to get an access to the inner layers.

3.3.3 Cross-Sectional KPFM on Solar Cells

The direct way to get access to the inner layers is to cleave a device and thereby expose the structure to the surface. As a next step the cross section of the device can be studied via KPFM under working condition, e.g. illumination (Figure 17).

In 1992 Nonnenmacher et al. studied a p- and n-doped silicon surface under illumination.[63] Six years later, Usunami et al. used cross-sectional KPFM to study quantum wells of GaAs/AlAs and InAlAs/GaAlAs structures.[64] The first study to combine both cross sectional imaging and illuminating was Mizutani et al..[65] They used cross sectional KPFM to study GaAs pn-junctions during illumination.

In 2001 Ballif et al. used cross sectional electrostatic force microscopy (~KPFM without a potential feedback – DC bias) on operating thin-film solar cells.[66] With the preparation of a cleaved, but still operating full device architecture, they were able to apply different working conditions and study the response of the potential distribution, e.g. open circuit conditions under illumination or an external bias.

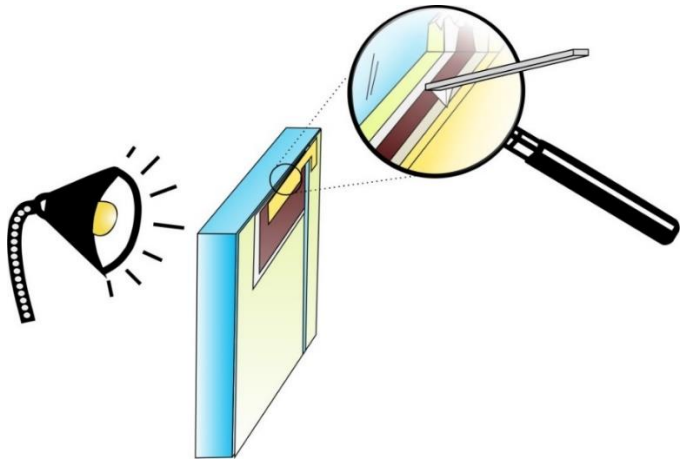

Figure 17: By cleaving a device in two parts, the cross section of the device can be studied via SPM techniques. Further, via cross-sectional KPFM it is possible to study the potential distribution on an operating cell, e.g. illumination with a light source.

Many more studies followed, measuring KPFM on different types of solar cells for working conditions.[67-81] However, the systematic optimization of the method to combine cross-sectional KPFM under operating conditions was still lacking.

A crucial point for the cross-section to be able to obtain detailed local information about the charge distribution is the sample preparation. While the cleavage of the structure results in a high surface roughness[66, 82] and thereby ends up in a reduced lateral resolution of the KPFM measurement, a post surface treatment can be used to smoothen the surface.[67] Post-surface treatments involves ion beam milling of the cleaved cross-section[67, 80] or microtome cutting.[80] However, post treatment is also discussed to end up in surface contamination and thereby misleading effects like defects and charge trapping.[72]

To guarantee that a smooth cross-section is provided and at the same time reducing the possibility of surface contamination to a minimum, a three-step preparation for all devices was applied, which included cleaving, contamination protection and fine-polishing. These preparation steps, which were used to receive a smooth and clean surface, had already been optimized for organic photovoltaics during my diploma thesis and have also been applied to all the different devices I studied in this thesis.[83] The device fabrication however, changed according to the architecture and collaboration partner and is explicitly described for each series of measurement in the appendix.

3.3.4 Sample Preparation

As a basic step the devices were cleaved into two parts. To be able to measure cross-sectional KPFM under operation, one of the resulting parts still needed to include the full device structure while at the same time exposed the layer structure to the surface.

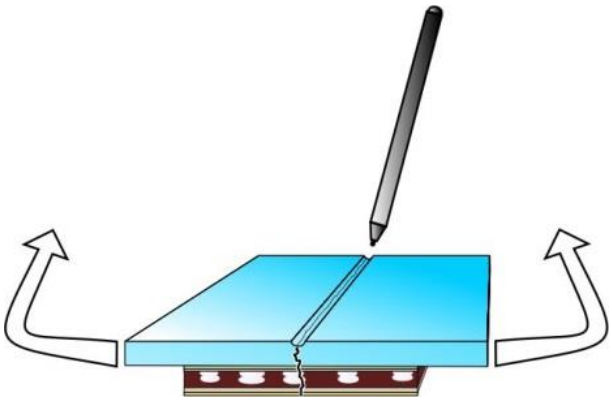

Figure 18: It is essential to perform a controlled crack of the device to receive a fully operating cross-section. By scratching the backside with a diamond cutter and subsequently breaking the device with pulling both ends and applying pressure to the cut, the device breaks in a controlled manner.

In order to perform a controlled crack, the backsides of the devices were scratched with a diamond cutter (Figure 18). By pulling at both ends, while at the same time applying pressure to the cut, the devices broke in a controlled fashion. However, the surface of the cross-section revealed a relatively high surface roughness, exceeding the thickness of the different layers.

In order to overcome the unfavorable surface roughness, the fresh cuts were subsequently prepared in a dual beam focused ion beam (FIB) setup (FEI Nova 600 Nanolab). Immediately after cleaving, the samples were transferred into the focused ion beam chamber.

As the pure surface treatment with ion beam milling of Ga^+ ions could possibly lead to surface contamination, the first step of the smoothening process was to deposit a platinum protection layer onto the top layer. The Pt layer was placed between the layers and the beam source and thereby prevented additional Ga^+ ions to enter the layer structure (Figure 19). Hence, contamination with Ga^+ ions was confined to the protection layer and the backside of the glass (see chapter 4.1.1 – energy-dispersive x-ray spectroscopy (EDX) measurements).

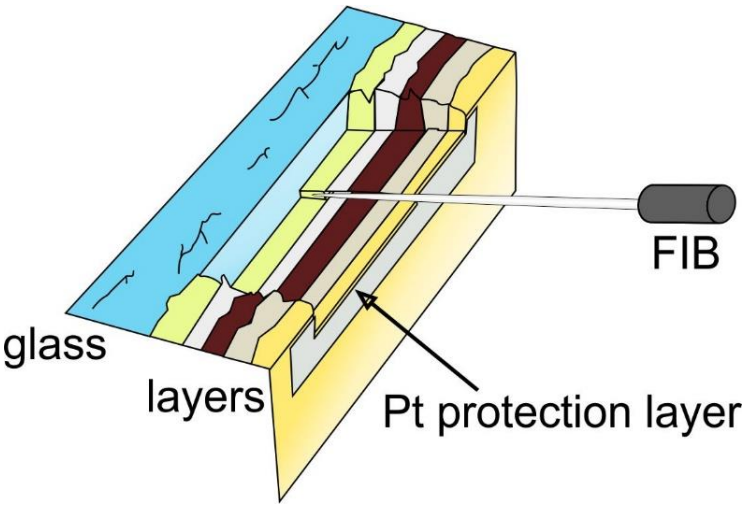

Figure 19: The roughness of the surface makes it necessary to apply a post treatment in order to receive a smooth cross-section. Using a focused ion beam (FIB), the surface can be milled with nanometer resolution. To protect the layer structure from contamination during the Ga^+-ion beam milling, a Pt protection layer is deposited on top of the structure.

In order to deposit the Pt on top of the structure a gas injection needle was inserted into the setup and placed in front of the gold layer. By injecting a precursor gas flow and at the same time focusing the ion beam, platinum could be deposited on the structure in a controlled fashion.

To provide a smooth and contamination-free transition between the gold and the platinum, the deposition was performed in two steps. The first step was the deposition of 50 nm platinum in an area of 60*5 μm^2 with a low current beam of 50 pA at an acceleration voltage of 30 kV. The low current guaranteed that the Ga-ions did not penetrate into the top electrode. The second deposition step was the deposition of a thick Pt layer of 2 µm directly on top of the thin 50 nm layer, with a reduced area of 50*4 μm^2 at a higher current of 1 nA and an acceleration voltage of 30 kV. With the higher current, thicker layers could be deposited in a finite amount of time. The thick layer ensured more protection from the following ion beam polishing step. Furthermore, the 2 µm thick platinum layer prevented the nm sized tip of the cantilever to fall over the edge when scanning the layer structure on top of the cross-section.

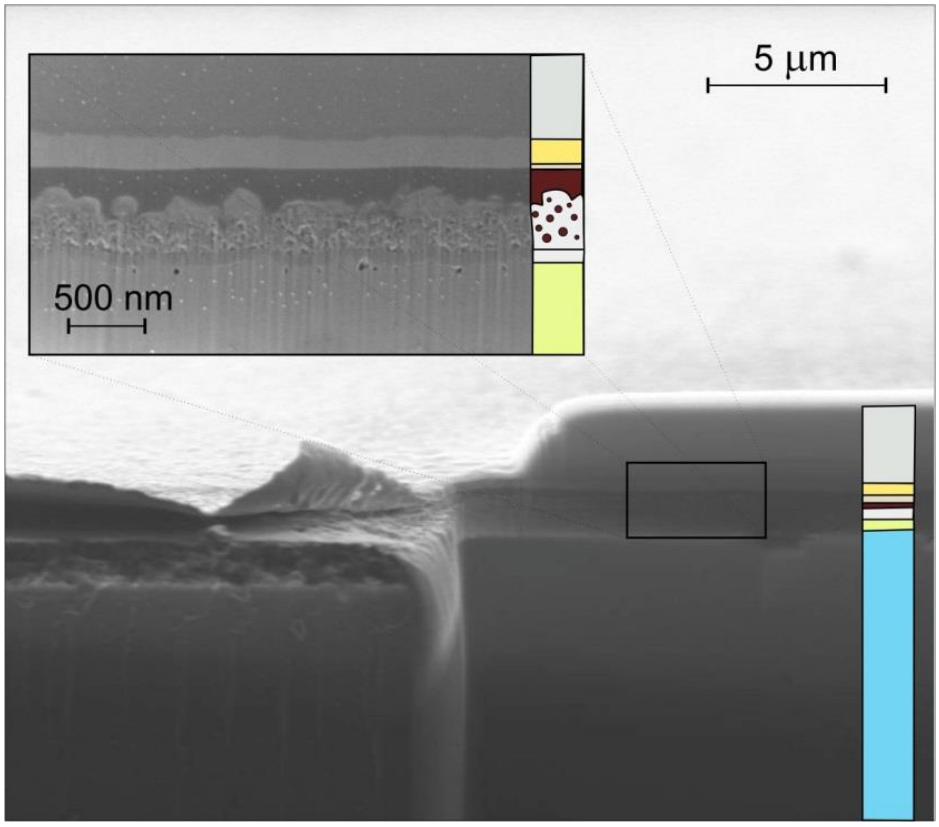

Figure 20: The scanning electron microscope (SEM) reveals the rough surface without post-treatment by ion beam polishing (on the left) and the smooth surface after FIB treatment (on the right). The inset shows a zoom-in which all layers can clearly be identified. From top to bottom the Pt protection layer (silver), Au (gold), Spiro-OMeTAD (very thin bright layer), perovskite MAPI (dark red), mesoporous TiO_2 with perovskite MAPI filling (silver with dark red dots), compact TiO_2 (silver), fluorine tin oxide (green) and glass (blue) can be observed.

The polishing process included two steps as well. The first step was a coarse-polishing, to create enough space for the cantilever approach. Therefore, more than 20 µm of material was milled in an area of 60*6 µm² with a high current of 3 nA at an acceleration voltage of 30 kV. The second step was a fine polishing step to provide a smooth and contamination free surface. Therefore, 5 µm of material was milled in a smaller area of 30*1.5 µm² with a low current of 100 pA at an acceleration voltage of 30 kV.

The resulting fine polished area provided a smooth surface and thereby optimized conditions for the cross-sectional KPFM measurements (see SEM Figure 20 inset).

After the preparation of the cross-section the device was directly transferred to the SPM setup, which was enclosed in a glove box under nitrogen atmosphere.

3.3.5 Setup

The setup consisted of a Standalone Molecular Force Probe 3d (MFP3d) from Asylum Research in an acrylic glass glove box (type P10R180T2, GS Glovebox Systemtechnik GmbH) with a constant dry nitrogen flush.[84] A controlled atmosphere with dry nitrogen is essential for the measurements on the cross-section under working conditions, since the perovskite MAPI ($CH_3NH_3PbI_3$) is known to degrade in air, especially under humidity.[37-39]

A UVICO-VIS broadband white light source (120 W; spectra see Appendix Figure 77) was placed next to the SPM head, providing the possibility to illuminate the device from the side while measuring on the cross-section. The white light was focused on the sample and filtered through a bandpass filter (Schott KG3 transmission >50% from 350 to 700 nm) in order to reduce the heat transfer and thereby drift during the measurement.

In order to perform cross-sectional KPFM, the sample was fixed in a special sample holder in an upright position. Furthermore, electrical plugs were integrated into the sample holder, to independently control the connections to both electrodes. These connections were accessible from the outside of the glove box to change the operating conditions during the measurement, e.g. short to open circuit conditions or an external bias.

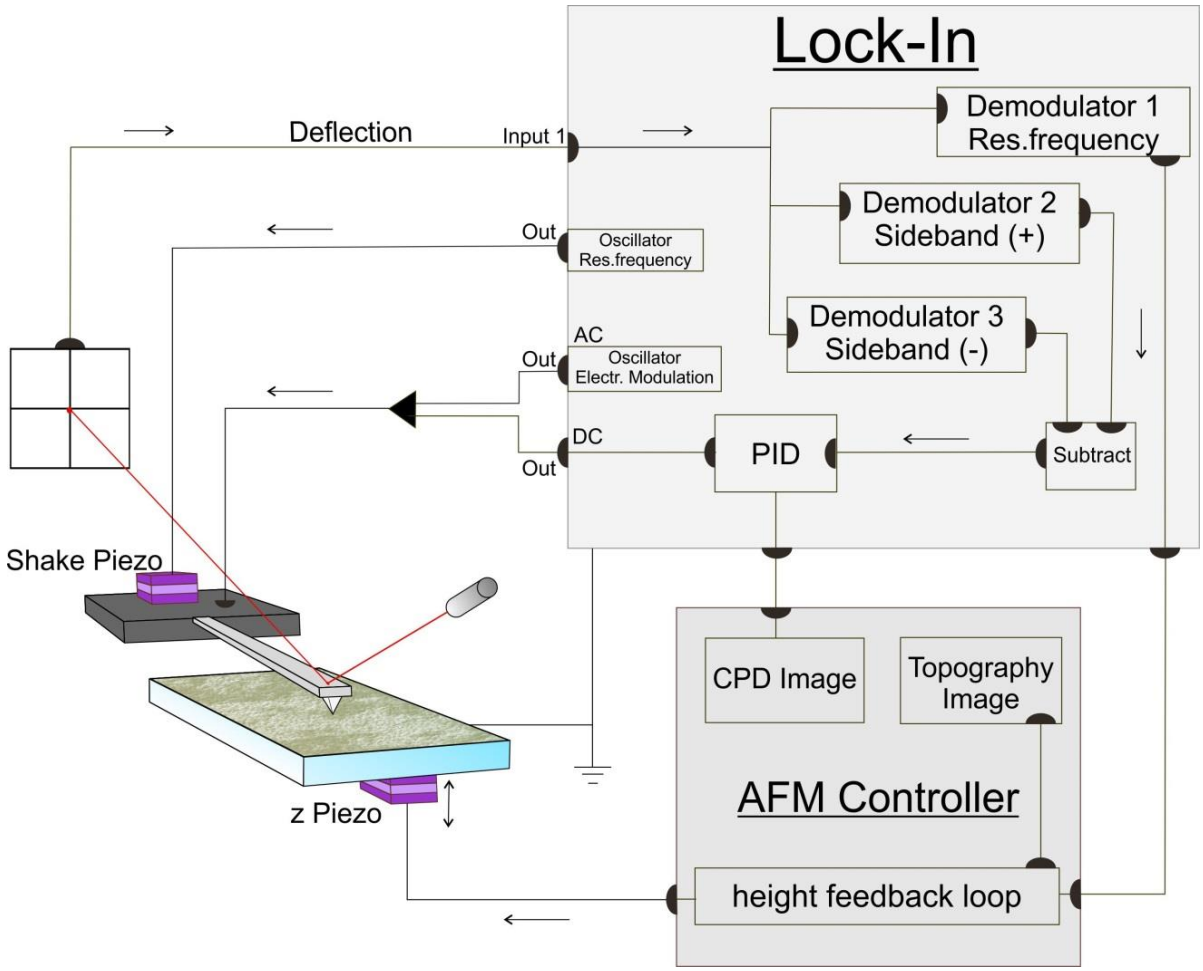

Figure 21: The setup for the FM-KPFM measurements, which shows the steps of the signal processing with an external lock-in amplifier in combination with the AFM controller.

Signal processing for the FM-KPFM measurements was performed with an external lock-in amplifier. In following the exact operating sequence is explained (Figure 21):

The shake piezo (which drives the mechanical oscillation of the cantilever) is excited at the cantilever's resonance frequency, while the modulation AC voltage (which produces the sideband peaks) is applied directly to the cantilever. The deflection signal is fed to the input of the lock-in amplifier. The lock-in amplifier measures the amplitude at the resonance frequency (demodulator R) and both modulation sidebands (demodulator X +/-).

Demodulator R: The change between the free oscillation amplitude and the oscillation amplitude during the measurement is fed to the MFP3d controller. The controller uses the signal as its feedback reference to adjust the distance between the tip and the sample and thereby images the topography.

Demodulator X: By subtracting the real part of both lock-in measured sideband amplitudes (the components have a phase shift of 180° and thereby opposite sign, see

equation 27) the resulting signal serves as the feedback to identify the contact potential difference U_{CPD}. The proportional-integral-derivative (PID) feedback loop applies a voltage U_{DC} to the tip, whereas the sidebands disappear when U_{DC} is equal to U_{CPD} (compare equation 21) The same signal is also fed into the controller, which displays the CPD parallel to the topography.

By following this procedure, it is possible to perform an FM-KPFM measurement. In order to prepare the reader for the analysis of the cross sectional KPFM measurements on MAPI perovskite solar cells with different device architectures and under various conditions, I will first introduce a simple exemplification on a model structure.

3.3.6 Exemplification

As a first example, I consider a simple structure with a conductive FTO (fluorine tin oxide) electrode connected to a gold electrode (Figure 22a - top). A single KPFM line scan records the contact potential difference between the materials of the layered structure. Considering the work functions of the different materials in the example to be $\phi_{tip} < \phi_{Au}\ (\sim -5.1\ eV) < \phi_{FTO} (\sim -4.4\ eV)$ the resulting CPD line profile is shown in Figure 22a (see equation 12).

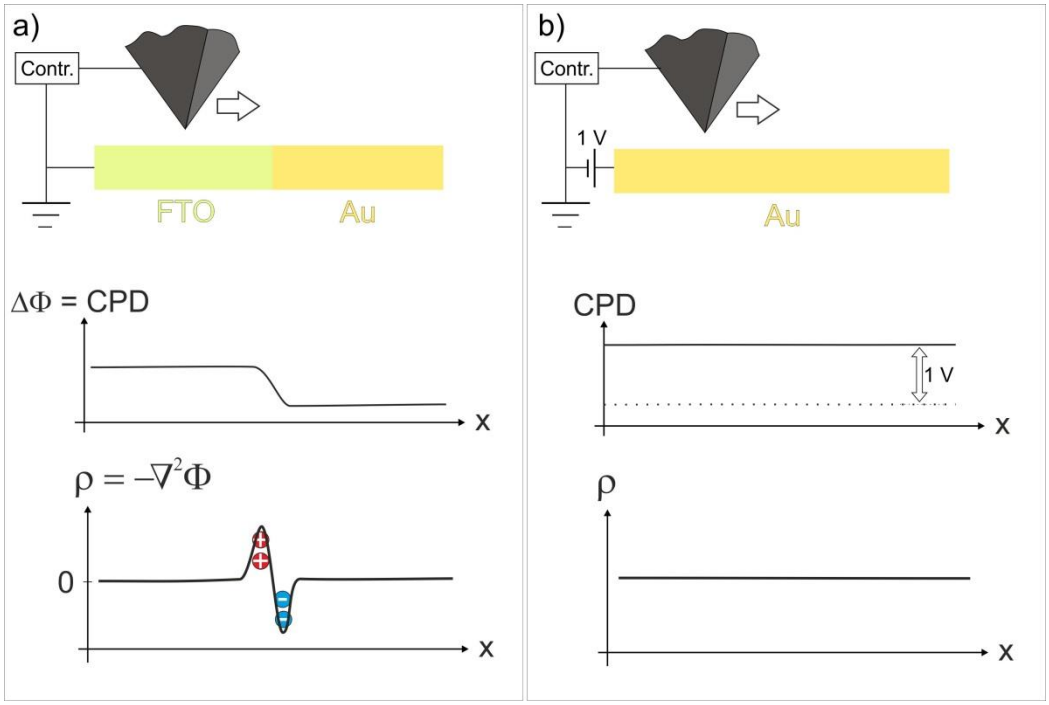

Figure 22: Example for the KPFM measuring routine and data evaluation for two simple model structures. (a) The first model structure consists of an FTO (fluorine tin oxide) layer and a gold layer. The resulting CPD profile shows the unperturbed scenario. By using the Poisson equation, the charge distribution can be calculated, with charges accumulating at the interface to align the Fermi levels. (b) A bias of 1 V is applied to a single gold electrode. The resulting CPD profile shows the increase in potential upon the bias. However, the calculated charge density distribution is not influenced by the external potential, even though positive charges are spread on the device (see explanation in text to understand the constraints for using the Poisson equation).

By using the Poisson equation, the charge density distribution $\rho(x)$ within the structure can be calculated:

$$-\nabla^2 U_{CPD} = \underbrace{\nabla^2 \frac{\phi_{tip}}{e}}_{=0} - \nabla^2 \frac{\phi_{sample}}{e} = -\frac{1}{e}\nabla^2 \phi_{sample} = \frac{1}{e\varepsilon}\rho \tag{28}$$

The resulting charge density distribution of the model structure is shown in Figure 22a bottom. The accumulation of charges is confined to the interface, where the charges redistribute in order to create the fermi level alignment.

In the next example an external potential of 1 V is applied to a single gold layer (Figure 22b). The CPD profile shows an overall increase of 1 V on the device structure. However, the charge density distribution still remains zero, even though additional positive charges must be present on the surface. This special example highlights the restrictions, for the conditions on how the Poisson equation can be used to study the distribution of charges from the potential distribution.

The general requirement to use the Poisson equation and calculate the charge distribution within a certain region is that charges are confined in space and the density of charges converges against zero for big distances (reference, e.g ground potential). In case of an external potential applied to a homogeneous surface, the charge density is higher compared to the equilibrium state with no external potential. But with the charges spreading all over the surface the Poisson equation cannot be used to calculate the charge distribution from the potential distribution within the area, as it doesn't converge against a reference within this area. In this scenario it would only be possible to calculate the charge distribution from the change in potential in vertical direction between the tip and the surface. In the vertical direction the charges are again confined to the surface, with the tip being the reference. However, in the lateral direction there is no reference, with charges homogenously spreading over the surface.

In the following measurements there is always a reference electrode, which is grounded and thereby the requirement for using the Poisson equation is fulfilled. Further, in case of a realistic measurement, small but sharp changes within the signal due to detection noise create a huge alternating error for the calculation of the charge density distribution. In order to receive the proper information about the charge density, the line profiles first need to be smoothed. The line profiles are therefore analyzed with OriginPro 8.5.1 G, which provides the Savitzky-Golay smoothening process.[85] The process fits a local polynomial regression of second order to a defined number of data points. Variations on a length scale smaller than 50 nm (mostly due

to noise) can thereby be sufficiently suppressed. However, towards the outer boundaries of the electrodes, the charge distribution is not exact anymore, caused by the second order polynomial regression at the edges.

4. Results

“A physicist is just an atom's way of looking at itself.”
— Niels Bohr

In chapter 2.2.4 – "Hysteresis" I summed up the relevant open questions about the internal device physics of perovskite solar cell. It was further necessary to systematically address the questions for each set of cell types, as there have been various uncertainties about the exact processes within an operating cell, depending on the cell type.

The **first step (4.1.)** was to study the internal potential distribution and thereby the electric field within a device for dark conditions representing the unperturbed **equilibrium state**. Results for devices of different types of cell architectures were compared to study the effect of the different internal interfaces and the influence on the charge density distribution.

As a **second step (4.2.)**, the potential distributions for one limiting case of operating conditions were examined by comparing results for **short-circuit conditions** under dark conditions and under **illumination**. Again, the results for different types of device architectures were analyzed and compared.

The **third step (4.3.)** was to study **open circuit conditions** and thereby the exact development of the open circuit potential across the interfaces. A detailed time-dependent examination of the charge distribution under open circuit conditions gave an insight into the charge shift under a precondition scenario.

The **fourth and final step (4.4.)** was to study the effect of an **external applied voltage** on the CPD distribution. The external potential thereby represented an external load and hence **actual working conditions** with a power output. To directly correlate the external measured current with the internal processes, the time-dependent charge dynamics were directly compared for both the current and the CPD.

4.1. CPD Distribution within Perovskite Solar Cells – Equilibrium State

4.1.1 Mesostructured Perovskite Solar Cell

The first device I will introduce is the mesostructured TiO_2 device, fabricated following the protocol of Burschka et al..[86] Back in January 2014, when the project started, these devices were state-of-the-art and showed the highest efficiencies and stabilities.

Parts of the results, which are discussed have already been presented in my manuscript "Real-space observation of unbalanced charge distribution inside a perovskite-sensitized solar cell", published in Nature Communications in 2014.[87] The exact procedure for the fabrication of the device is simply transferred from the manuscript and can be found in the appendix-1. The devices were fabricated at the École polytechnique fédérale de Lausanne (EPFL) by my collaboration partner Javier-Francisco Ramos under the supervision of Shahzada Ahmad, Mohammad Khaja Nazeeruddin and Michael Grätzel.

J-V Device Characterization For the current density versus voltage analysis directly after fabrication, my collaboration partner Javier Ramos used a setup consisting of a 450 W Xe lamp (Oriel) with a Schott K113 Tempax sunlight filter (Praezisions Glas & Optik) as a light source. A digital source meter (Keithley Model 2400) was used to apply the voltage to the cell while the current was recorded with at the same time. The active area was fixed to 0.2025 cm^2 using a metal mask. For the J–V curve after the measurements, a 150 W Xe lamp (Oriel) with a UVB/UVA dichroic mirror (280–400 nm) was employed as the light source.

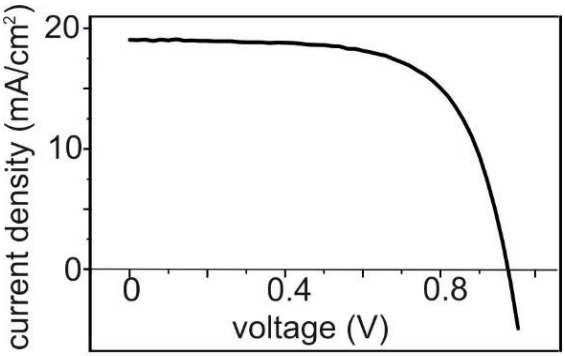

J_{SC}	V_{OC}	FF	PCE
19.05	0.97	0.66	12.54

Figure 23 JV-characteristics showing the backward scan for the device with the thick mesoporous TiO_2 layer structure. The table shows the device parameters with a resulting PCE of 12.5 %.

Notice: At the time when the measurements were made, there was no common knowledge about the hysteresis in JV curves. Thereby, we were not aware about it and no data about the forward scan of the JV-curve and therefore about the hysteresis has been captured for this device, even though the device most certainly exhibited a mesostructured device type JV-hysteresis.[40] The JV-characteristics for the device resulted in a PCE of 12.5 % for the backward scan (Figure 23).

As already specified in the sections 3.3.3 and 3.3.4, the preparation of a smooth cross section is essential to get reliable local data from the KPFM measurements afterwards. When applying the focused ion beam (FIB) polishing process, a smooth and therefore defined surface for the SPM measurement can be provided. A concern for the validity of the KPFM results on polished cross-sections under operation however, was a possible Ga^+ contamination during the FIB treatment. This contamination could have created surface defects and thereby misleading results for the KPFM measurement. In order to exclude the changes in surface potential from Ga contamination, it was necessary to check the elemental distribution for the polished cross section. Therefore, Dr. Ingo Lieberwirth from the group of Prof. Katharina Landfester performed an **elemental analysis** with scanning transmission electron microscopy (STEM) in combination with energy dispersive X-ray spectroscopy (EDX) on a separated cross section thin lamella (Figure 24). Secondly, in order to exclude a possible Ga^+ contamination on the prepared surfaces, Gunnar Glasser from the project group of Dr. Lieberwirth performed **EDX-measurements** on the actual cross sections (Figure 25). Both measurements were performed after all the KPFM measurements to not alter the cell before the actual study.

Elemental Analysis For this purpose, Maren Müller prepared a thin lamella of the prepared cros-section with the FIB and subsequently transferred it onto a TEM grid. The elemental analysis by STEM-EDX (Tecnai F20 FEI/EDAX) was in agreement with the suggested cell structure: a bulk TiO_2 layer on top of FTO, followed by a mesoporous layer (Figure 24). This mesoporous layer contained Ti at a lower concentration than the compact layer.

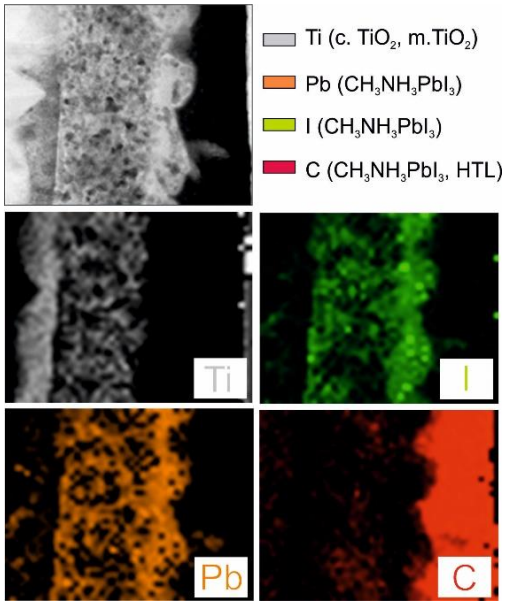

Figure 24: Cross-sectional elemental analysis using scanning transmission electron microscopy. The STEM micrograph and corresponding elemental maps show the relative distribution of Ti, Pb, I and C in agreement with the expected theoretical device architecture. Particularly, the perovskite MAPI (Pb & I) infiltrates the pores of the mesoporous scaffold down to the compact TiO_2.

Furthermore, Pb was homogeneously distributed throughout the mesoporous layer, representing the perovskite MAPI. The highest Pb concentration corresponded to the perovskite capping layer. In this layer, no signal from Ti was recorded. The upper Spiro-OMeTAD hole transport layer (HTL) contained the highest concentration of C.

EDX-Measurement For the EDX-measurement, Gunnar Glasser transferred the polished cross-section into the SEM to measure combined SEM/EDX on top (Hitachi SU 8000 SEM equipped with a Bruker X-Flash silicon drift detector). Within the accuracy of the measurement (typically around 1 µm for a qualitative analysis),[88] the Ga concentration was restricted to the Pt protection layer on the front of the device (Figure 25a – purple profile). Furthermore, by comparing the distribution of the significant elements representing the different materials in the device structure, the technique proved to be able to correctly localize the respective interfaces and therefore correlate it with the Ga signal (Figure 25b). The additional Pt protection layer on the front of the device successfully served its purpose by preventing Ga^+ ions from contaminating the lower layer structure during the polishing process.

By optimizing the preparation routine and with checking the elemental analysis on top it could be ensured that no significant contamination was impacting the inner layer structure of the cross-section. Further, I could continue with analyzing the SPM measurements. The first important part of the KPFM measurement was to check the topography scan whether the interfaces can be identified with this technique as well.

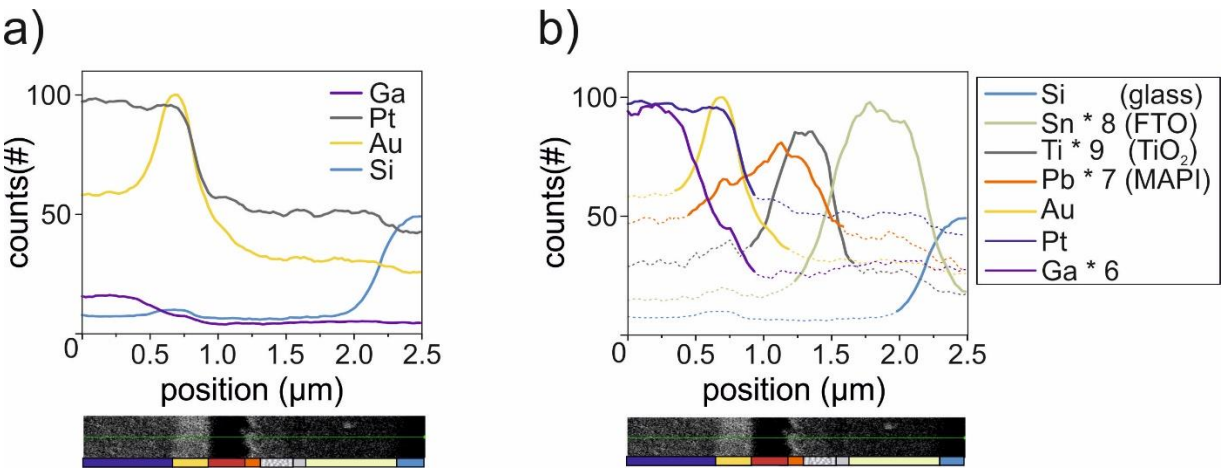

Figure 25: (a) EDX raw data line profiles (top) scanned over the green line across the layer structure (bottom). From left to right Pt (protective layer), Au (top-electrode) and Si (glass). The purple curve represents the Ga, which only has a significant magnitude within the Pt protective layer. (b) Line profiles for selected elements and partially scaled to visualize the location within the layer structure. Starting from left with the Pt, Au, perovskite (Pb), mesoporous TiO_2 and compact TiO_2, then FTO (Sn) and glass (Si).

SPM-Measurements For the SPM measurement, a PPP-EFM cantilever (PointProbe Plus Electrostatic Force Microscopy; Nanosensors) with a resonance frequency of 68.587 kHz and an oscillation amplitude of ~70 nm was used. Double sideband frequency modulation KPFM was performed with a modulation frequency of 1 kHz and an AC tip voltage of 3 V in single scan mode. The scan rate was set to 0.6 Hz. From analyzing the height image of the SPM-scan, the root mean square roughness of 2.6 nm was calculated (Figure 26a).
With such a relatively flat surface (surface roughness is much smaller than the layer thicknesses), the interfaces of the different layers could be identified from both height and phase images (Figure 26a/b), in accordance with the SEM (Figure 20 inset) and STEM-EDX measurements (Figure 24/25). From the height and the phase images, the locations of the interfaces could be reconstructed (Figure 26c) and in a second step directly correlated with the CPD data gained by KPFM.

Before the results for KPFM measurements could be analyzed, it was necessary to first elaborate what was actually expected to be measured in the CPD distribution across a device. The important question I wanted to address with the first set of KPFM cross-section measurements was:

➔ How does the internal field within a perovskite solar cell look like?

With a band diagram detailed information about the condition of the electronic device structure can be checked. The band diagram includes the energies of the valence and the conduction band for the different semiconducting layers, as well as the energy levels corresponding to the work functions for the conductive layers (Figure 27a).

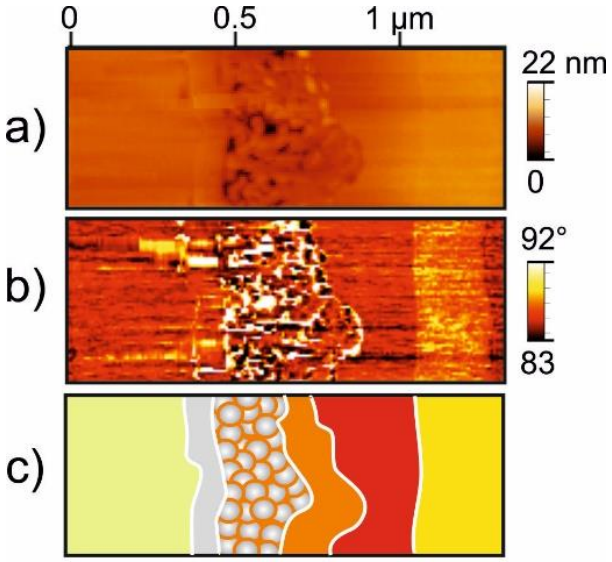

Figure 26: SPM topography images of the focused ion beam polished cross section for the thick mesoporous device architecture using intermittent mode. (a) Height image with a surface roughness of 2.6 nm. The different layers are already visible with (from left to right) FTO – compact TiO_2 – mesoporous TiO_2 – perovskite capping layer – Spiro-OMeTAD – Au. (b) Phase contrast between the excitation and the cantilever oscillation, which changes due to the material dependent tip-sample interaction (c) Sketch of the device architecture recreating the interfaces, which are observed in the topography images.

The energy levels of the band structure thereby play an important role for the charge transport of the dissociated charges. With the offsets between conduction bands, a free electron can be extracted from the perovskite MAPI to the energetic favorable TiO_2 and finally to the FTO, while the offsets between valence bands attracts the hole from the MAPI to the energetic favorable HTL and finally to the Au.

However, the band diagram only considers the layer structure prior to the contact generated fermi level alignment in the device. This fermi level alignment results in a redistribution of charges at the interfaces and hence an internal electric field developing across the device. Consequently, the exact redistribution of charges, corresponding to the respective locations of the fermi levels, is the crucial factor for the development of the electric field and therefore the electric potential across the layer structure (exemplification in Figure 27b – see vacuum level shift). Especially the perovskite MAPI layer, which is expected to undergo an unintentional self-doping (n- or p-type) during the fabrication process,[89-91] majorly defines the electric potential distribution with the shift of Fermi level.

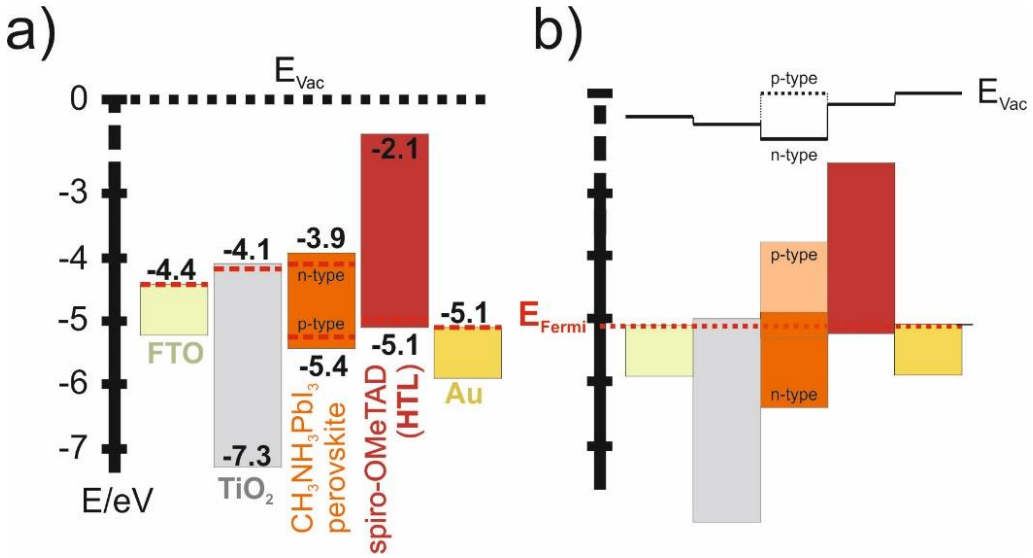

Figure 27: (a) Theoretical band diagram for the mesostructured device structure before layers are in contact.[87] The Fermi level in the perovskite layer depends on the stoichiometry of the respective ions and thereby can exhibit p- or n-type doping.[92] (b) After bringing the layers into contact the alignment of the Fermi levels results in a shift in vacuum levels (see 3.3.1 Contact potential difference). For the KPFM measurement with the tip scanning above the layer structure, the resulting CPD profile matches the vacuum level within the layer structure, with the offset of the vacuum level shift of the tip. As the work function of the tip is constant, the CPD directly corresponds to the potential distribution across the device. Note: Band bending at the interfaces within the device is not considered in the sketch. The resulting band structure will show a continuous curve at the interfaces and throughout the device.

So far, indirect measurements of the potential distribution of the layer structure led to confusion.[5, 93] While Laban et al. used a Mott-Schottky analysis to reveal the formation of a pn-junction at the TiO_2/ MAPI interface,[93] Edri et al. used electron beam induced current measurements (EBIC) on cross sections to conclude the presence of a p-i-n junction.[5] Furthermore, measurements from X-ray photoelectron spectroscopy (XPS) and ultraviolet photoemission spectroscopy (UPS) also gave inconsistent data about the location of the fermi level within the band gap of the perovskite.[94-96] With cross sectional KPFM measurements the exact potential distribution within the device can be analyzed.

KPFM-Measurements Both electrodes were grounded, and the device was kept in dark conditions to keep the device in the equilibrium state without any external influence. A CPD line profile was extracted from the KPFM image (Figure 28b) and plotted in a graph (Figure 28c). The dashed grey lines mark the position of the interfaces for the line profile extracted from the topography scan (Figure 28a). The green and the yellow box located at both ends of the curve highlight the positions, where the CPD saturated on the electrodes. Assuming that the work function of the tip stayed constant during the scan, the CPD difference between the two highlighted areas reflects the built-in potential of the device. With work function values for FTO (~ -4.4 V)[97] and for Au (~ -5.1 V),[98] the difference ΔCPD in the measurement of about ~0.6 V corresponded well with the values from literature.

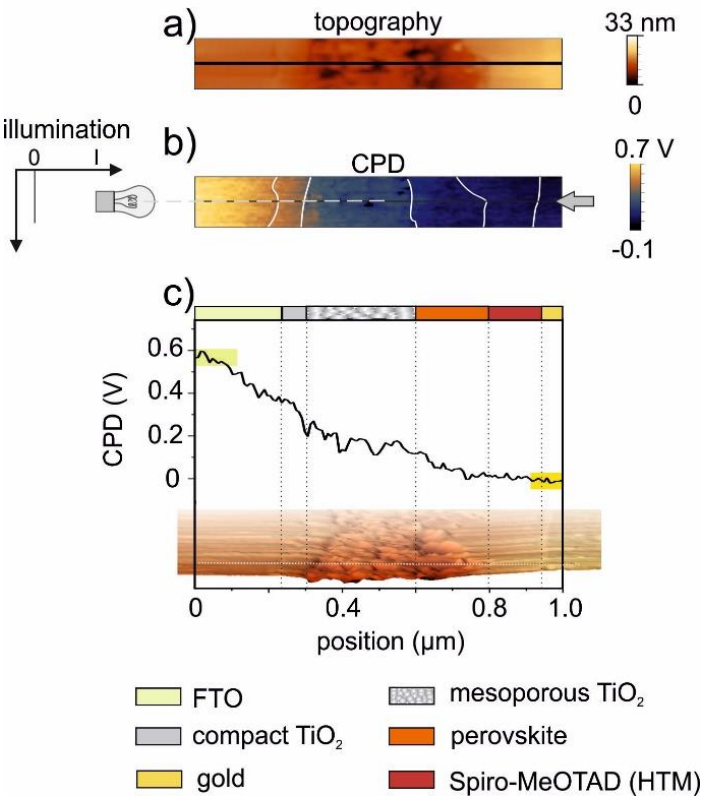

Figure 28: Mesostructured device under short-circuit conditions without illumination with (a) the SPM topography image and the corresponding (b) KPFM contact potential difference measurement. The interfaces, which are observed in the height image, are marked as white lines in the KPFM image to correlate the CPD distribution with the positions of the interfaces inside the device. The line profile marked with the grey arrow is plotted in (c).

The CPD profile developed an almost monotonous decay from the FTO all the way to the Au electrode, creating a p-i-n junction (Figure 5). The intrinsic layer hereby refers to the TiO_2/perovskite MAPI active area, while positive charges were present at the FTO/TiO_2 interface and negative charges were present at the Au/Spiro interface. The constant decay within the intrinsic layer is thereby solely generated by the built-in potential. Within the p-i-n junction, the monotonous potential decay of the intrinsic layer, results in a constant electric field. With the electric field spreading over the whole absorber, charge carrier collection is supported by drift, guiding the photo-excited charges to their respective electrode.[99] The result of a p-i-n junction, with a monotonous decay in electrical potential within the intrinsic layer, is in agreement with the results obtained by EBIC measurements.[5] However, small drops in potential at the selective interfaces as suggested by Edri et al., were not observed for the mesoporous device.

J-V Device Characterization In order to confirm the operational condition of the processed cross-sectional solar cell during the measurements, the PCE of the JV-characteristics was checked again after the measurements. This time a 150 W Xe lamp (Oriel) with a UVB/UVA dichroic mirror (280 – 400 nm) was employed as the light source. A digital source meter (Keithley Model 2400) was used to apply the voltage to the cell while the current was recorded. The active area was 0.24 cm^2. The analysis of the JV-characteristics resulted in a PCE of 8.49% (Figure 29). The processed device thereby exhibited a loss in charge extraction, caused by degradation effects during the processing and measurements. However, no drop in open circuit voltage was measured and therefore, operational conditions during the KPFM measurements were confirmed. Before further conclusions are made from the results of the measurements on the mesoporous device, two planar devices and an intermediate mesoporous/planar device are analyzed. By comparing these results, the influence of the mesoporous and planar interfaces at the electron selective contact can be checked and an overall conclusion based on the statistics of analyzing diverse device structures can be drawn.

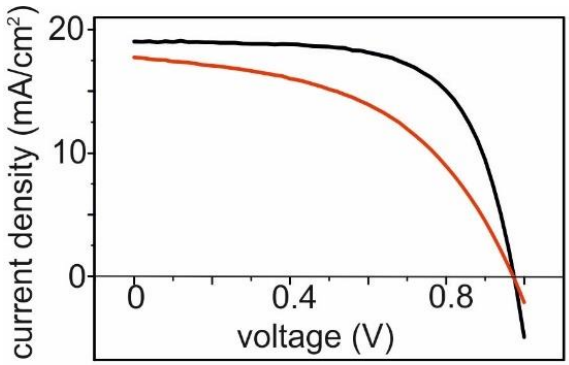

	J_{SC}	V_{OC}	FF	PCE
before	19.05	0.97	0.66	12.54
after	17.80	0.97	0.48	8.49

Figure 29: JV-characteristics measured before the sample preparation (black curve) and after all preparations plus measurements (red curve). The cleaved and processed device still exhibited 76% of the initial PCE. Losses appeared only from a reduction in the current, but not from losses in open circuit voltage.

4.1.2 Flat-Junction Perovskite Solar Cells

Parts of the results, which are discussed have already been presented in my manuscript "Local Time-Dependent Charging in a Perovskite Solar Cell" published in ACS Applied Materials & Interfaces in 2016.[100] The devices were fabricated at the University of Tokyo, by my collaboration partner Yunlong Guo under the supervision of Hideyuki Tanaka and Eiichi Nakamura. The exact procedure for the fabrication of the flat-junction devices was directly transferred from the manuscript and can be found in the appendix-2.

J-V Device Characterization The JV-characterization was performed with the same setup as used for the second measurements of the mesostructured device after KPFM imaging, described in the section before. Two planar devices were chosen for the measurements, which had distinct differences in their hysteresis. The first and more efficient device (flat-junction #1) had an inverted[45] hysteresis (Figure 30a). The forward scan (black arrow) resulted in a PCE of 8.1% while the backward scan (red arrow) resulted in a lower PCE of 7.1%. The second and less efficient device (flat-junction #2) had a more pronounced standard hysteresis (Figure 30b). Here, the backward scan (red arrow) resulted in a PCE of 4.8 %, while the forward scan (black arrow) resulted in a lower PCE of 3.3%. These devices were explicitly chosen for the study, since they had opposite hysteretic characteristics. Hence, significant differences were expected to be observed in the CPD distribution as well. Any observations made on the internal field distribution could possibly be linked to the performance of the respective devices, when comparing these results.

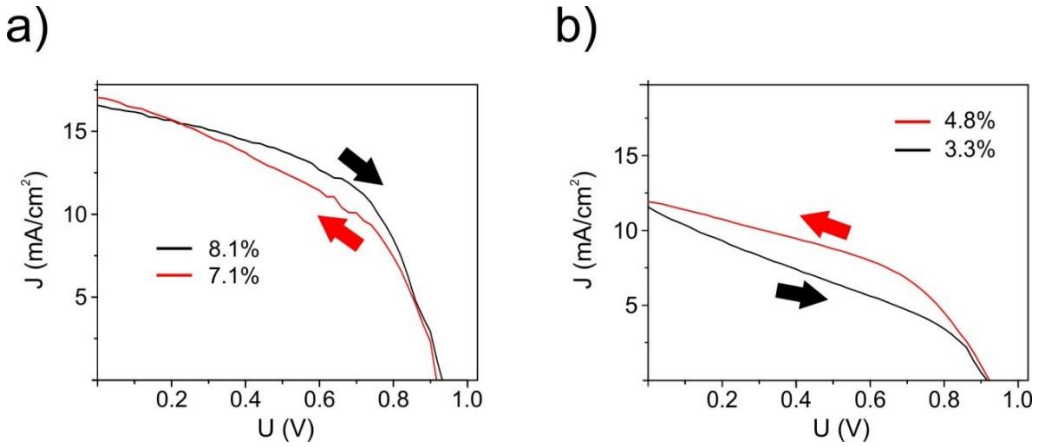

Figure 30: JV-characteristics of two different flat-junction devices with opposite characteristics in hysteresis. (a) Flat-junction device #1 with a higher efficiency of the forward scan with 8.1 % (black curve), compared to the backward scan with 7.1 % (red curve), the device exhibited an inverted hysteresis. (b) Flat-junction device #2 with a lower efficiency and more distinct standard hysteresis with 3.3% PCE for the forward scan and 4.8% PCE for the backward scan.

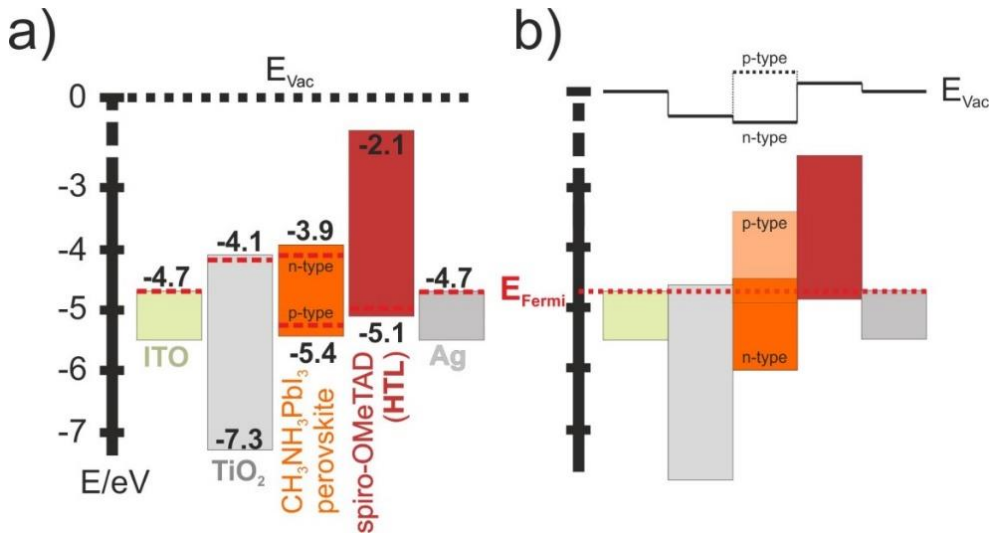

Figure 31: (a) Theoretical band diagram for the planar device similar to the one for the mesostructured device (Figure 27). The differences in the energy diagram compared to the one for the mesostructured device are the electrode materials (ITO, Ag). (b) After connecting all the layers, the difference between the fermi levels in electrode materials also results in a variation of the shift in vacuum levels, when compared to the mesostructured device. The difference from the electrode materials is then expected to result in a different CPD line profile for the cross sectional KPFM measurement.

Compared with the previous device architecture of the mesoporous cell, the band diagram of the flat-junction devices has some small differences with the exchange of the electrode materials to indium tin oxide (ITO) and Ag (Figure 31). Hence, the resulting distribution of the potential after Fermi level alignment was expected to differ compared to the mesoporous device. Furthermore, the absence of the mesoporous layer results in a defined homogeneous TiO_2/MAPI interface. Again, a self-doping of the perovskite MAPI would result in a shift of the Fermi level and therefore the alignment with the correlated vacuum level shift.

KPFM-Measurements Similarly to the first measurement, a PPP-EFM cantilever was used and excited at a mechanical excitation frequency of 69.78 kHz with an excitation amplitude of ~70 nm and an electrical modulation frequency of 1 kHz (V_{AC} = 3 V). For both flat-junction devices a difference in CPD of ~100 mV was measured between the ITO and the Ag electrodes (Figure 32), which is consistent with work-function values from literature (ITO and Ag both have a work function of -4.7 eV for the corresponding deposition technique of the fabrication process).[101, 102]
For the device flat-junction #1 (Figure 32a) an increase in CPD from left to right of about ~ 180 mV from the ITO towards the TiO_2 was observed. At the TiO_2/MAPI interface (blue arrow) the CPD dropped about ~ 270 mV over a width of ~100 nm. Next, a ~120-nm-wide region of almost-constant CPD extended through the MAPI layer. Towards the interface between the hole-transport layer (HTL) and the Ag, the CPD dropped around 50 mV (orange arrow) over a width of ~ 100 nm.

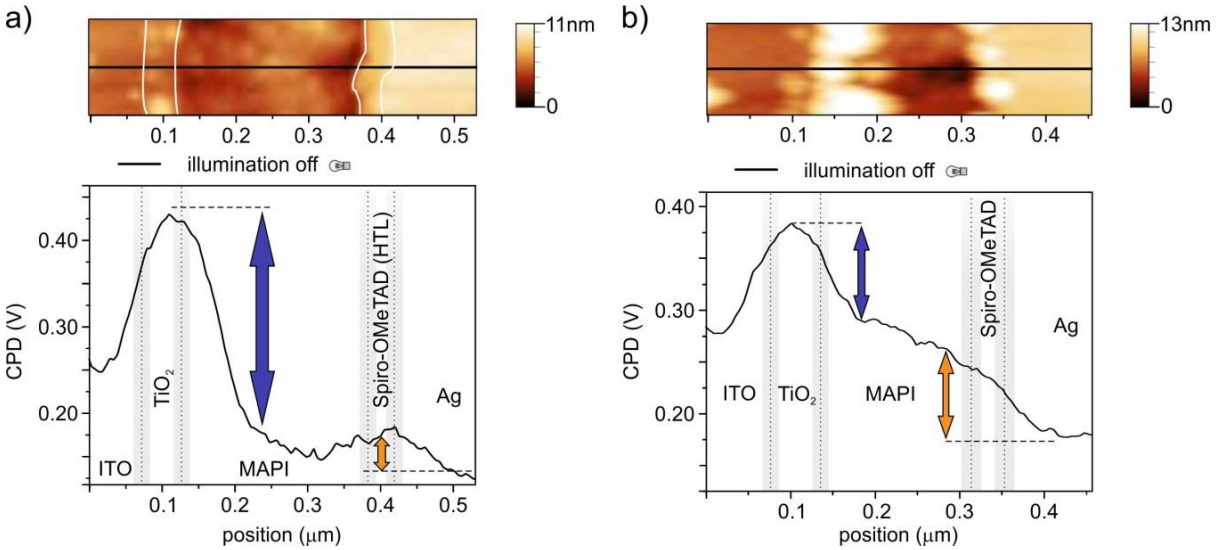

Figure 32: SPM topography images and their corresponding CPD profiles (black line) for (a) the flat-junction device #1 which had a higher efficiency and an inverted hysteresis and (b) flat-junction device #2 which had a lower efficiency and a standard hysteresis (compare Figure 30). For clarity, the positions of the interfaces were illustrated with gray bars in all diagrams. While the blue arrows mark the drops in CPD at the electron transport layer (ETL) interface, the orange arrows mark the drops in CPD at the HTL interface. Notice: (b) The topography image of the less efficient device had a slightly rougher surface which might ended up in a reduced lateral resolution of the KPFM measurement. However, the differences in the trend of the CPD profiles is not supposed to be affected by this.

In comparison for the device flat-junction #2 (Figure 32b) a smaller increase in CPD from the ITO to the TiO_2 with ~ 120 mV was observed. Next to it, a drop of ~ 90 mV developed at the TiO_2/MAPI interface over a width less than 90 nm. Within the perovskite MAPI, the CPD stayed almost constant (with a tendency of a slight decay). Across the MAPI/HTL interface, a second drop in CPD of ~100 mV was measured over a width slightly bigger than 100 nm.

Compared to the previous results for the mesostructured device, significant differences were observed for the CPD profiles of the flat-junction devices. The first difference was observed at the transparent electrode/TiO_2 interface with a corresponding increase in CPD from the ITO electrode to the TiO_2 contact. The increase in CPD can be explained by the initial position of the fermi levels, hence a transfer of electrons from the TiO_2 into the ITO, leaving holes within the TiO_2. The second difference was the drop in CPD at both selective interfaces to the perovskite (Figure 32 blue and orange arrows). In the previous section about the mesostructured device it was concluded, that a p-i-n junction with a monotonous decline in CPD from the FTO to the Au had formed. However, in case of the flat junction devices the CPD dropped at the selective interfaces, with a field free MAPI layer. That referred to an accumulation of negative charges within the MAPI layer at the TiO_2 interface (Figure 33), whereas for device #1 the accumulation of negative charges was shifted around ~50 nm from the interface into the MAPI layer (Figure 33a).

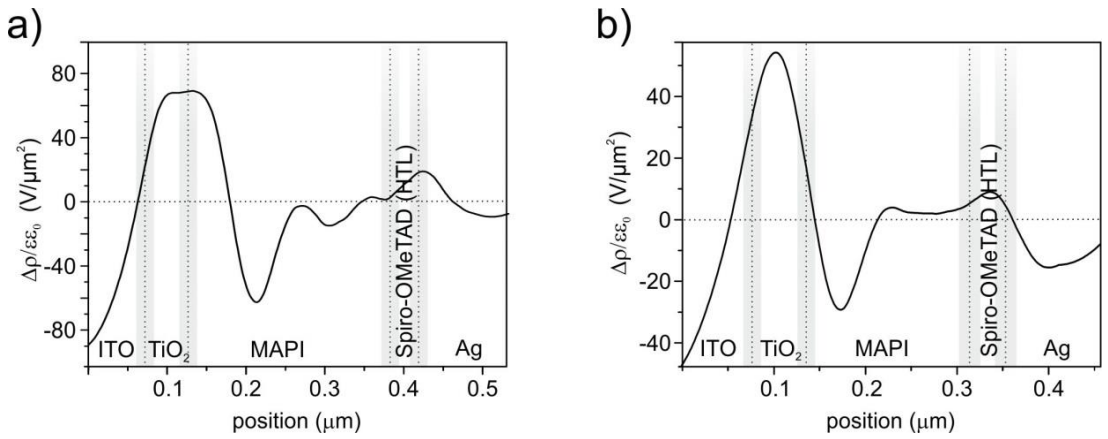

Figure 33: Charge density distribution profiles calculated from the CPD distribution showed in Figure 32 respectively. Both devices exhibit a positive charged region at the TiO_2 following a negative charged region in the perovskite layer, close to the TiO_2 interface.

While the mesoporous device formed a p-i-n junction with a monotonous decrease in potential, the flat-junction devices formed a field free MAPI layer. Therefore, the question arises, what is the role of the mesoporous layer and how is the build-up of a field-free MAPI layer in the flat-junction device possible?

The drop of the CPD at the TiO_2/MAPI interface with a charge depletion zone is actually in agreement with previous assumptions about a re-arrangement of mobile ions inside the perovskite MAPI.[103-105] In particular, the constant CPD in the MAPI bulk, showing a field-free MAPI layer with depletion zones at both sides was predicted in simulations performed by van Reenen et al..[106] Using drift-diffusion models, they could reproduce hysteresis loops in I-V efficiency measurements by considering the presence of mobile ions, which migrate through the device under the presence of an electric field and trapped charges, which are confined at the interfaces.[106] Richardson et al. used similar methods and could simulate hysteresis in perovskite solar cells by solely considering mobile ions, without any trapped charges.[107] According to these simulations, mobile ions redistribute at the selective interfaces under the influence of the electric field inside the p-i-n junction, resulting in a field-free MAPI bulk, which was also suggested by Eames et al. (Figure 34a)[108] and Azpiroz et al. (Figure 34b).[109] Possible candidates of mobile ions to rearrange within the MAPI are I^- vacancies, which redistribute in front of the HTL (p-layer) and/or MA^+ ions, which rotate and align (or also redistribute) in order to screen the electric field of the p-i-n junction.

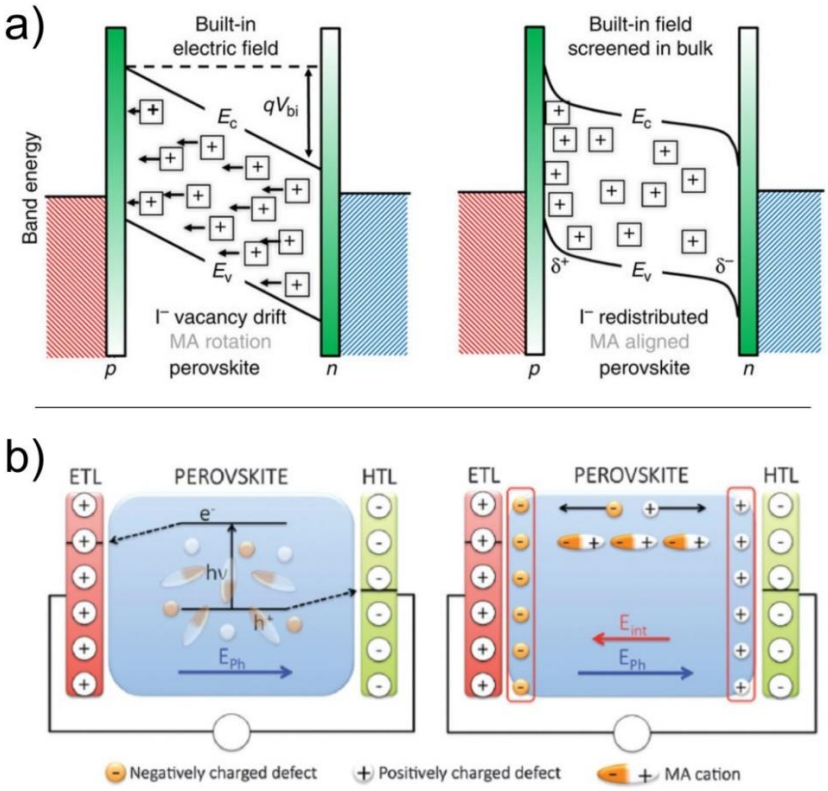

Figure 34 (a) I^- Ion migration under the influence of the built-in electric field, which screens the field within the intrinsic layer and causes band bending at the interfaces. "Reprinted with permission from (Nat. Commun. 2015, 6, 7497.). Copyright (2015) Nature Publishing Group."[108]). (b) Defect migration suggested by Azpiroz et al.[109] whereas the electric field E_{Ph} caused by the built-in potential is screened by the re-arranging ions causing an internal electric field in the other direction E_{int}. "Reprinted with permission from (Energy Environ. Sci. 2015, 8 (7), 2118-2127.). Copyright (2015) The Royal Society of Chemistry."

As mobile ions are expected to be present within the perovskite MAPI layer, the question rises why they have not been observed within the mesostructured device? Why was the electric field of the p-i-n junction not screened within the mesoporous device, with mobile ions accumulating at the interfaces? And could the mobility of the ions also have caused the differences of the CPD distribution and accordingly the device performances between both flat-junction cells?

Before I will address these specific questions, I want to show the results for a third device structure, which actually combines the mesostructured and the planar architecture with a thin mesoporous layer and a thick perovskite capping layer on top. The discussion about the differences of the CPD distributions and the correlation of the mobility of ions for different device architectures will follow at the end of the chapter to conclude the first part of "CPD distribution within perovskite solar cells – equilibrium state".

4.1.3 Thin Mesoporous Perovskite Solar Cell

As already described in the fundamentals chapter, today's efficiency record cells consist of a thin mesoporous TiO_2 layer with a thick perovskite capping layer on top.[28] Furthermore, with the intermixing of methylammonium/formamidinium (MAI/FAI) as the organic cations and iodide/bromide as the halides to form the compositional mixed-cation perovskite crystal structure, record efficiency devices with higher stability and less hysteresis were fabricated.[28, 110] In order to complete the chapter about the internal CPD distribution under equilibrium conditions, a state of the art device with the above mentioned architecture was studied. The materials section for the device fabrication can be found in the appendix-3.

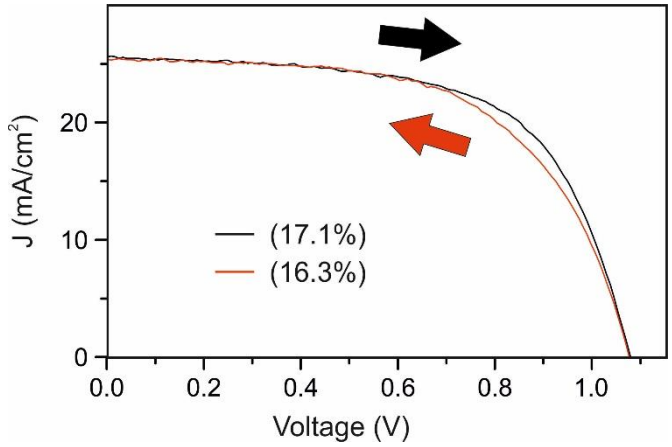

Figure 35 JV-characteristics for the thin mesoporous – thick perovskite capping layer device. The device shows a high efficiency with a slight inverted hysteresis.

J-V Device Characterization From the measurements of the JV-characteristics an efficiency of 17.1% for the forward scan and 16.3% for the backward scan was calculated (Figure 35).

Notice: The setup which was used for the JV-measurements of this specific device, later turned out to be not perfectly accurate. JV-characteristics of devices which were measured with the setup resulted in lower efficiency values, compared with numbers from the groups which fabricated the devices. An internal resistance of the reference cell, which was used to calibrate the setup beforehand was degraded and thereby followed in a false calibration. Therefore, the absolute value for the calculated efficiency of the device had a systematic error. From comparing efficiency values from the devices which were sent from collaborators at other labs, with the efficiency values measured with this setup, a maximum error of 20% was expected. Hence, the PCE for the device was 16.7% (±3.3%).

However, even though the absolute numbers of the JV-measurement had a systematic error, the quantitative shape of the JV-curve was still valid and showed an inverted hysteresis. Inverse hysteresis has already been reported for devices with the intermixing of MAI and FAI to form the mixed perovskite structure.[45] Tress et al. suggested that the accumulation of mobile ions in front of the TiO_2 creates an advantageous interfacial dipole at the electron selective interface (TiO_2/mixed perovskite). This dipole helps electrons to overcome an extraction barrier at the TiO_2 interface, which is supposed to result from the shift in the band structure when intermixing MAI with FAI. Thereby, an enhanced charge transfer exhibits at the forward scan for the inverted hysteresis phenomenon. Further, photoelectron-spectroscopy measurements revealed that the conduction band of the intermixed perovskite is ~0.3 eV below the conduction band of TiO_2 for the contact and thereby creates the unfavorable extraction barrier.[111]

KPFM-Measurements A distinct drop in CPD of about ~350 mV was measured at the FTO/TiO_2 contact, saturating in a constant CPD within the mixed perovskite layer (Figure 36).

Notice: The exact interface between the mesoporous TiO_2 and the perovskite capping layer was hard to distinguish from the topography image of the SPM measurement. This interface in the graph was marked in accordance with the information from our collaborators, that the total layer thickness of the compact TiO_2/mesoporous TiO_2 typically was ~200 nm.

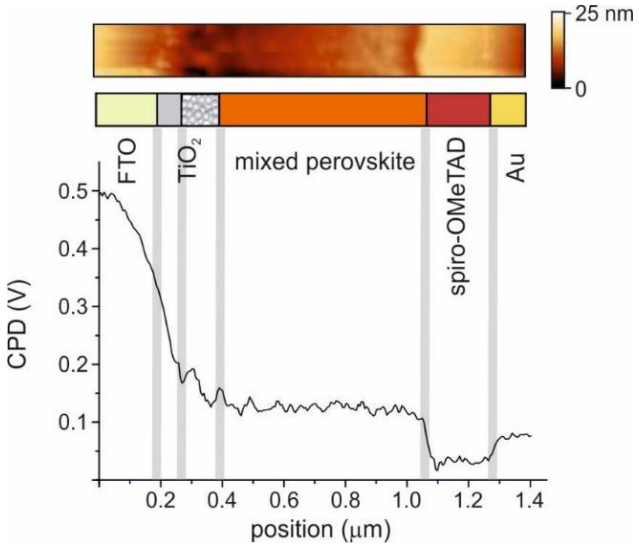

Figure 36: CPD line profile of the thin mesoporous device system. The CPD distribution shows a distinct potential drop at the TiO_2 with a constant potential inside the perovskite capping layer, similar to the CPD distribution inside the flat-junction devices. A smaller second potential drop is observed at the perovskite/HTL interface.

Another drop in CPD of about ~100 meV was observed at the perovskite/Spiro interface, while an increase of about ~50 meV was observed at the Spiro/Au interface.

With the corresponding charge density distribution profile, it could be concluded that opposite charges arrange at the FTO/TiO_2 and at the mixed perovskite/Spiro interfaces (Figure 37). The accumulation of positive charges at the FTO interface is in agreement with the results from the mesoporous device structure. However, similar to the flat-junction devices the CPD did not follow the CPD distribution of a homogenously decreasing p-i-n junction. With opposite charges accumulating around both selective interfaces, the thin mesoporous device exhibited a field-free perovskite bulk, similar to the flat-junction devices.

The overall CPD distribution of the device configuration can therefore also be explained by the formation of a p-i-n junction with a field free intrinsic layer. Following the explanation for the flat-junction devices, hence, the theoretical considerations made by van Reenen et al.[106] and Eames et al.,[108] the re-arrangement of ions within the perovskite layer is generated by electric field driven migrated ions.

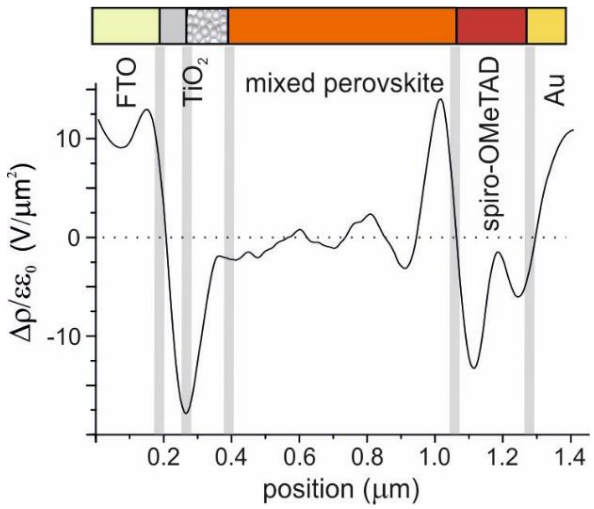

Figure 37: Charge density distribution profile calculated from the CPD distribution shown in Figure 36. A region of opposite signed charges is observed at the FTO (+) /TiO2 (-) interface and at the mixed perovskite (+) /HTL (-) interface. The observed charge distribution can be explained by the re-arrangement of ions/vacancies inside the mesoporous/perovskite layer, which screen the electric field of the p-i-n junction as shown in Figure 34.

The results of the CPD distributions across different device architectures (Figure 38) are in agreement with the tendencies of CPD distributions observed by Cai et al..[112] In their study they observed that the CPD is generally dropping across the compact TiO_2 layer, whereas a thick mesoporous TiO_2 layer can significantly stretch the drop in CPD over a larger width.

However, following the suggestion that a re-arrangement of ions is the underlying cause for the drop in electric potential and thereby the field-free perovskite layer, following questions arise:

- ➔ Why did the ion migration appear in the flat-junction and the thin mesoporous, but cannot be observed in the thick mesoporous architecture?
- ➔ Could ion migration be the cause for differences in CPD distributions for similar device structures? And is there a correlation between the CPD distribution and the device performance?

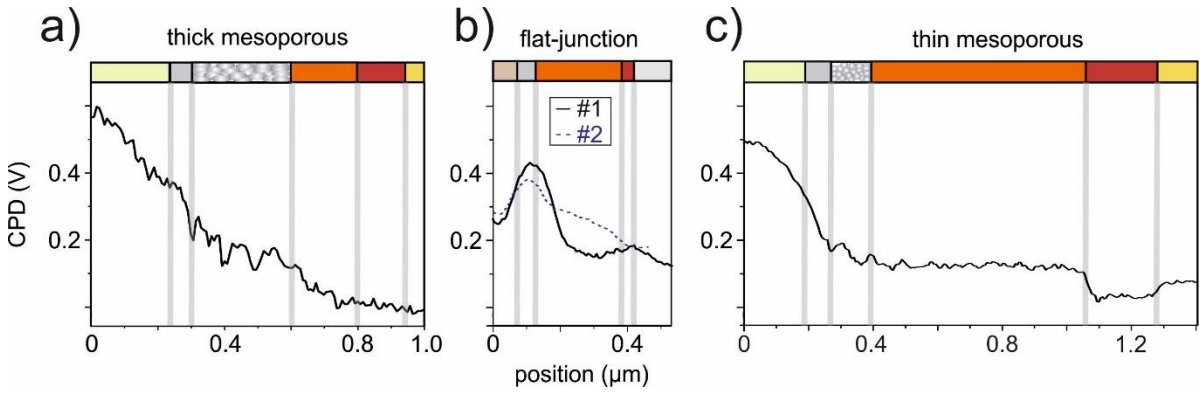

Figure 38: CPD distribution for equilibrium conditions of the (a) thick mesoporous, (b) flat-junction and (c) the thin mesoporous device structures. While the flat-junction and the thin mesoporous device structures exhibit distinct drops in CPD towards the charge selective interfaces, the thick mesoporous device exhibit an almost monotonous decrease over the full structure.

4.1.4 Discussion

In order to elucidate the differences in CPD distribution for the various device architectures and to discuss possible explanations, it is necessary to get more insights into what is known about the ion migration and its consequences on the hysteresis.

An electric field inside the device results in an electrostatic force on the mobile ionic species within the perovskite crystal lattice (Figure 39b). The re-arrangement of mobile ions at the interfaces, driven by the electric field, accordingly leads to the screening of the electric field within the layer (Figure 39c).[108, 109]

Accordingly, when an external bias is applied to the device (e.g. when performing a J-V scan), mobile ions are expected to re-arrange under the influence of the bias and hence the electric field inside. The re-arrangement of ions at the interfaces leads to band bending and therefore a time-dependent change in charge-extraction under illuminated operating conditions. This time delay explicitly depends on the mobility of the ions.

In case of the migrating ions, the kinetics is highly sensitive to the local crystal structure.[113] The pathways for the solid-state diffusion are defined by the distribution and concentration of vacancies/defects in the crystal lattice. The Schottky formation energy of defects is quite low with 0.14 eV per defect, which results in an overall defect density of 0.4 %.[114]

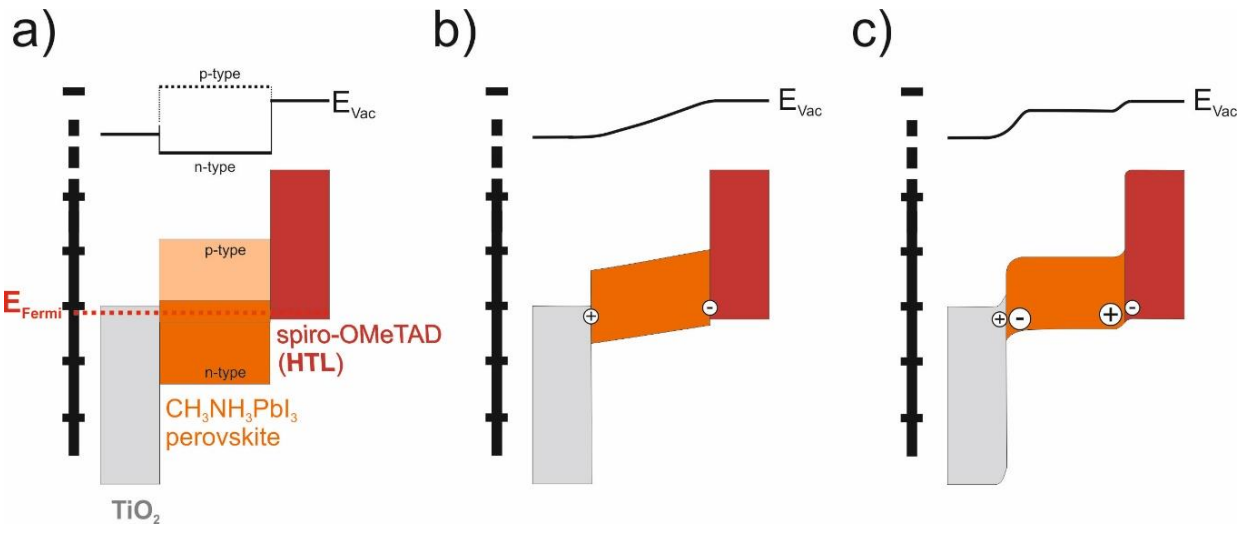

Figure 39 (a) Energy diagram of the perovskite layer, sandwiched between the charge selective layers (adapted from Figure 27 and Figure 31). (b) A n-i-p junction is formed with a monotonous electric field within the perovskite layer, which results in an electrostatic force on the mobile ions and charges within the perovskite layer. (c) Mobile ions then move towards the interfaces, leading to a screening of the electric field and band bending at the interfaces.

Possible candidates to migrate through the crystal lattice are:[113]

- protons[115]
- methylammonium[109, 116]
- iodide[108, 117]

Since all three species are likely to migrate through the device, the exact contribution depends on their specific activation energies. However, there is controversy about the exact activation energies for the different species. While KPFM cannot help to solve the problem by giving local chemical information and therefore directly detect the type of mobile species, the focus of the analysis of the measurements under equilibrium conditions stayed on the comparison of the local arrangement of ionic species or charges between the different device architectures.

The thick mesoporous TiO_2 layer seemed to suppress the ions from migrating under initial dark conditions. Considering that ion migration is the cause of the hysteresis, a general lower hysteresis for mesoporous devices compared to flat-junction devices[40] supports the hypothesis of a suppression of ion migration by the mesoporous layer.

Two possible scenarios that explain the suppression of ion migration within the mesoporous TiO_2 could be:

1. The mesoporous TiO_2 filled with the perovskite MAPI exhibits a decreased defect level concentration and therefore no pathways for the ion migration.

Defect levels are actually easily formed within the perovskite crystal, as the process of crystallization during the device fabrication is quick and thereby far from thermodynamic equilibrium.[118] Further, the processing method for the film fabrication defines the stoichiometric ratio and thereby the defect density.[119] The two-step fabrication method, which was used for the mesoporous device is known for both excessing PbI_2 and MAI, resulting in a self-doping of n-type or p-type respectively.[89, 90]
While, these findings could explain variations in defect level concentration for the perovskite layer between different devices or device architectures, it also implies that the exact potential distribution within such a device can change in one batch of samples. For the flat-junction cells, a difference was actually observed for the respective CPD (Figure 38b). Caused by unintentional doping during the fabrication process, the perovskite layer of the device with lower efficiency might exhibited a higher p-doping, compared to the perovskite layer of the device with the higher efficiency.[89, 91]

2. The perovskite crystals within the pores of the mesoporous exhibit higher activation energies due to smaller crystal sizes[120] and an extended impact of grain boundaries.

Insights into theoretical considerations about the defect physics are limited to the bulk crystal, with knowledge about the processes at grain boundaries still lacking.[118] However, an increase in activation energy at the grain boundary is highly likely, which makes it possible to slow down[120] or even suppress the ion migration within the mesoporous structure.

The explanation for the scenario of mobile ions redistributing under the influence of an external electric field is in agreement with other studies from literature and helps to understand the CPD measurements of the different devices.[40, 106-109] To gain more insight into the processes and find more reasonable validation for this suggestion it was necessary to study the CPD distribution under working conditions and the correlating time dependencies of internal processes.

4.2. Short Circuit Conditions

As a first step for studying the CPD distribution under working conditions, the effect of illumination under short circuit conditions was analyzed. Therefore, a broadband white light source was placed next to the setup (as explained in 3.3.5), which illuminated the vertically placed solar cell from the side, while measuring cross-sectional KPFM on top. Both electrodes were set to ground to keep the cell under short circuit conditions. Therefore, photo excited charges could be extracted, when reaching the corresponding electrode and the maximum current could flow through the cell (see 2.1.1 – Characteristics of a solar cell). Since the device was kept in the state with the limit in charge extraction under working conditions, any change of the CPD within the device compared to equilibrium would point to possible bottlenecks for the optimum in charge transport.

4.2.1 Mesostructured Perovskite Solar Cell

The measurements, which are presented in this section are the follow-up measurements for the experiments described in 4.1.1, with all the details about the device already mentioned in this section. Again parts of the results were published in my manuscript "Real-space observation of unbalanced charge distribution inside a perovskite-sensitized solar cell" published in Nature Communications in 2014.[87] As this structure is kept throughout the thesis, I will not further mention it anymore.

KPFM-Measurements For the unperturbed equilibrium state in dark, a monotonous decline in CPD distribution over the layer structure was measured, representing a p-i-n junction as already discussed in the chapter before (Figure 40b – black line profile).

For the illuminated case, an increase in the CPD was observed within the perovskite capping layer (Figure 40b – red line profile). The CPD profile exhibited a slight increase in the mesoporous TiO_2 of about ~30 mV and then increased rapidly at the mesoporous TiO_2/perovskite MAPI interface with a maximum difference of almost ~400 mV compared to the line profile measured under equilibrium. Inside the perovskite capping layer, the CPD kept a constant level following a decrease back to the initial equilibrium level across the perovskite MAPI/Spiro interface. The bump in the CPD profile was thereby mainly confined to the perovskite capping layer, which could also be directly observed in the KPFM image in Figure 40a.

After the CPD was measured with the illumination turned on, another scan was performed under dark conditions after the light was turned off again.

For the conditions after illumination, the CPD did not completely overlap with the initial CPD profile in equilibrium (Figure 40b – blue line profile).

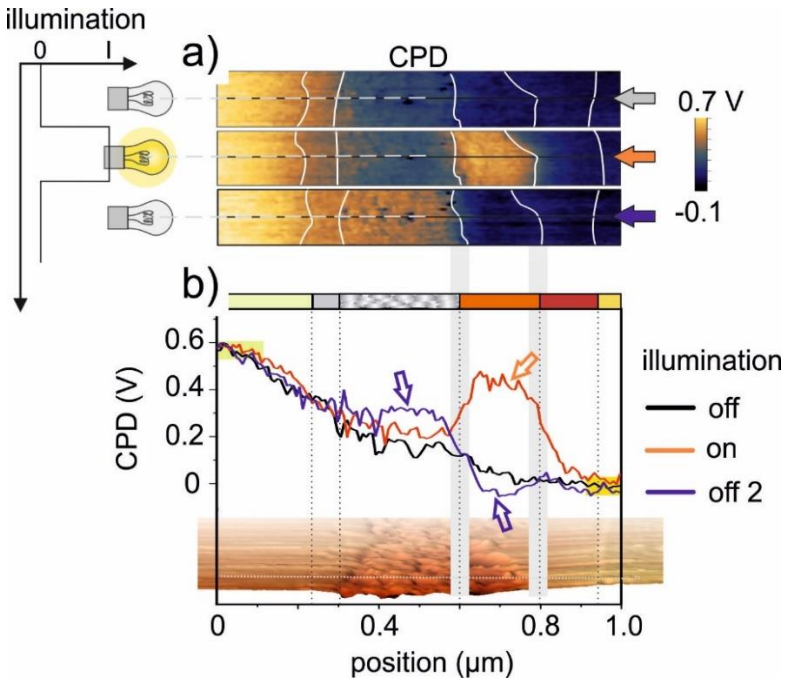

Figure 40: (a) KPFM images with the location of the extracted CPD profile for equilibrium (grey), illumination (red) and after illumination (blue) at the same scan position. The locations of the interfaces are marked in the images with white lines. In comparison to the image for equilibrium, in the illuminated case an increase in CPD is observed within the perovskite capping layer. After light is turned off again the mesoporous layer reveals a higher CPD compared to the initial equilibrium conditions. (b) The CPD line profiles for the three different conditions in equilibrium (black curve), under illumination (red curve) and after illumination (blue curve). The arrows mark the changes in CPD compared to the equilibrium state. While the CPD distribution under illumination increases within the perovskite capping layer, it does not return to equilibrium after illumination but remains with a positive offset in the mesoporous layer and a negative offset in the perovskite capping layer.

Compared to the CPD profile in equilibrium, a positive offset in CPD of +100 mV was measured in the mesoporous TiO_2 layer, while a negative offset of -50 mV was measured in the perovskite capping layer (Figure 40b blue arrows).

For the CPD distribution after illumination a positive offset for the mesoporous and a negative offset for the capping layer have been observed, compared to the equilibrium state. With these offsets a drop in CPD developed at the mesoporous/perovskite interface. However, after several minutes in dark, the CPD returned back to the initial equilibrium state (not shown).

Notice: Since the measurements on the device were performed without the consideration of observing a time dependent process, the measurement parameters were not optimized on analyzing a time-dependency. Measurements for different conditions were performed image by image. With a scan rate of 0.6 Hz and 256 lines per image, the time resolution of the measurement for a particular line profile was in the order of ~10 minutes. Furthermore, the rough surface of the mesoporous interface

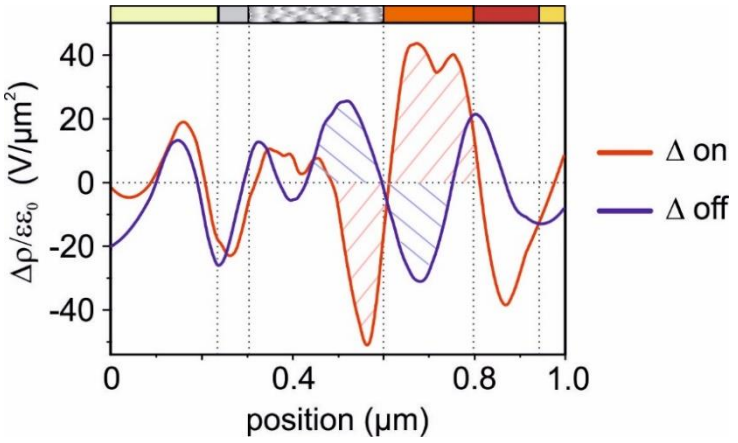

Figure 41: By using the Poisson equation, the exact positions for accumulated charges, which are responsible for the changes in CPD distribution, can be calculated. Charge density distribution for the respective CPD differences of the profiles shown in Figure 39. The red profile represents the difference in charge density between the illuminated and the dark case. Additional positive charges accumulate at both interfaces within the perovskite capping layer, while negative charges are present in the mesoporous TiO_2 and the HTL next to the perovskite capping layer interfaces. The blue line profile shows the difference between the charge density after illumination and the initial dark case. While positive charges are now present in the mesoporous TiO_2, negative charges remain in the perovskite capping layer.

hinders a time-dependent analyzation of the processes within the cell, since the effect of the topography and the CPD changes cannot be differentiated. The analysis of the CPD distribution on the effect of the illumination thereby has to be limited to the particular unspecific timeframes shown in Figure 40.

More detailed information about the location of charges inside the mesoporous device could be generated with the corresponding photo generated charge density distribution (Figure 41). Under illumination (red line profile) additional positive charges arranged at both interfaces within the perovskite capping layer, while negative charges arranged inside the mesoporous TiO_2 (at the interface to the perovskite capping layer) and within the Spiro-OMeTAD (at the interface to the perovskite). In my manuscript, I ascribed this accumulation of positive charges inside the perovskite capping layer to an unbalanced charge transport of holes and electrons towards their respective electrode.[87] With the charge extraction being unbalanced, one of the charge carriers remains longer inside the perovskite layer and thereby a higher density is present within the perovskite layer. In this case, the hole extraction would have been the bottleneck of the charge transfer inside the device, with holes accumulating in the perovskite.[87]

Several following studies mentioned an inefficient unbalanced charge transport as well.[111, 121, 122] However, all of them described a potential barrier from the perovskite MAPI to the TiO_2 and thereby a slower charge extraction of the electrons. They even explicitly mention a possible accumulation of electrons inside the perovskite at the

TiO_2 interface.[121, 122] However, no electron accumulation could be observed in the KPFM measurements.

What is clear so far is that when the light is absorbed inside the perovskite layer, charges dissociate and holes start to accumulate inside the perovskite capping layer. These holes arrange in front of the interfaces in order to screen the self-induced electric field. As a result, electrons arrange on the selective grounded transport layers and screen the field to the outside.

Back when the manuscript got published, the community was not aware of mobile ions. Still, from the static measurements it cannot be distinguished between an initial accumulation of electric charges or mobile ions. Hence, both scenarios must be considered for further analysis.

The charge density distribution after illumination revealed an opposite distribution compared with the illuminated case (Figure 41 - blue line profile). An accumulation of positive charges was observed in the mesoporous layer and an accumulation of negative charges was found in the perovskite capping layer. In the manuscript I proposed these excess charges to trap states.[87] Electron traps were filled during the light absorption, whereas they were screened by the accumulated positive charges.[87]

Residual positive charges in the mesoporous layer however could have also been present for a different reason. With the light induced charge accumulation of positive charges inside the perovskite capping layer and the negative charges at the mesoporous interface, a strong electric field was present at the mesoporous TiO_2/MAPI interface, which could have caused positive charged ions to migrate into the mesoporous perovskite layer (Figure 42). Since the measurements only included a single time frame, shortly after turning on the light, the time dependency of the process was not measured and potentially might have further evolved over time during the illumination. This explanation of light induced charge accumulation and a resulting electric field generated ion migration is in agreement with the studies presented by Wu et al..[122] Furthermore, an ion migration due to light induced charge accumulation could also be the reason for the general preconditioning of a device under short circuit conditions,[44] which is known from literature as "light soaking".[123] This suggestion is in agreement with the studies by Zhao et al..[124]

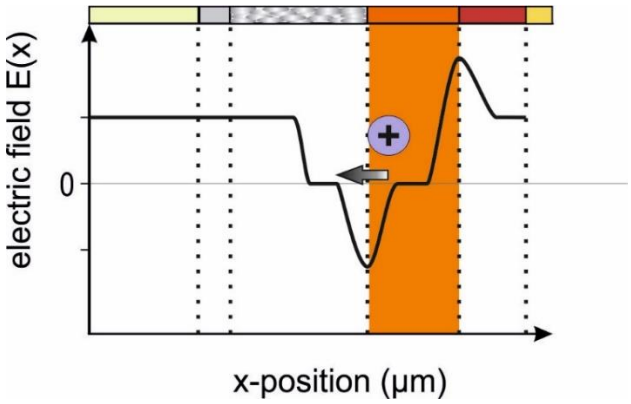

Figure 42: Sketch of the qualitative electric field distribution within the device for the illuminated case. The accumulation of positive charges in the perovskite capping layer and negative charges in the mesoporous TiO2 lead to the built up of a strong electric field at the mesoporous TiO_2 interface. Affected by the strong electric field, positive charge carriers (like I^- vacancies) migrate into the mesoporous layer during the illumination, resulting in the charge distribution shown in Figure 40 - blue line profile.

Besides the explanation of an unbalanced charge extraction, the increase in CPD upon illumination could also be referred to the formation of a surface dipole. A surface dipole might form when the device is exposed to light or under the influence of an external bias, such as an aligned orientation of molecules at the TiO_2/perovskite interface. Furthermore, the electric field of the surface dipole could then similarly induce the migration of ions. When the light is switched off, the relaxation process could then be referred to a slow recombination process[92] and the re-arrangement of the mobile ions. For now, these scenarios, namely an accumulation of positive photoexcited charges and the formation of a surface dipole, both connected with a re-arrangement of mobile ions are the most reasonable explanations to describe the observed phenomenon. A more detailed discussion about the expected underlying mechanism will follow at the end of the chapter after considering the results from all three device architectures.

4.2.2 Flat-Junction Perovskite Solar Cells

Parts of the results, which are presented in this section were again already published in my manuscript "Local Time-Dependent Charging in a Perovskite Solar Cell" in ACS Applied Materials & Interfaces (2016).[100] As this structure is kept throughout the thesis, I will not further mention it anymore.

Flat-Junction Device #1 The first flat-junction device which was studied under illumination, was flat-junction #1 with higher efficiency and slightly inverted hysteresis. Unlike the thick mesoporous device structure, no change in CPD upon illumination was observed for the corresponding measurement of flat-junction device #1 (Figure 43 compare black and red curve).

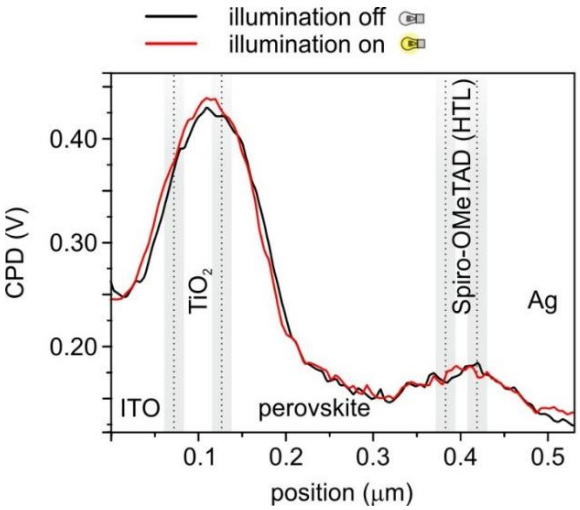

Figure 43: CPD profiles for dark condition (black line profile) and under illumination (red line profile) for the flat-junction device structure with higher efficiency. No significant change in CPD is observed, unlike the previous measurements on the thick mesoporous device structure, concluding no unbalanced charge transport for the device.

With no change in CPD upon illumination, the assumption was made that this device did not suffer from an unbalanced charge transfer or the formation of a surface dipole. When comparing the CPD distributions of the flat-junction device in equilibrium (Figure 43) with the thick mesoporous device after illumination (Figure 40b – blue line profile), a similarity in CPD distribution could be observed. Both CPD distributions had a drop in CPD at the MAPI/TiO_2 interface (in case of the mesoporous device towards the mesoporous TiO_2 scaffold) with a lower CPD within the perovskite and a subsequent increase towards the HTL. For the thick mesoporous device upon illumination, I previously suggested that a re-arrangement of charges changed the internal electric field until an optimum band bending for balanced charge transfer was reached. This re-arrangement compared to the equilibrium state was then observed, when the light was turned off.
Therefore, a possible explanation for flat-junction device #1 showing no charge accumulation under illumination, could be that the optimum field distribution for balanced charge transfer was already present under equilibrium conditions. With no changes in CPD upon illumination, the CPD also stayed on the same level when the light was turned off again (not shown).

Flat-Junction Device #2; Light on Unlike the response of device #1, for flat junction device #2 with lower efficiency and standard hysteresis an increase in CPD upon illumination was observed (Figure 44a). In order to record the time-dependent increase in CPD during the measurement without having the side effects of small inhomogeneities at the interfaces, the scan axis of the KPFM scan perpendicular to the interfaces was disabled. Therefore, the tip constantly scanned the same line profile over and over again, while the time-dependent, photo-generated changes were recorded.

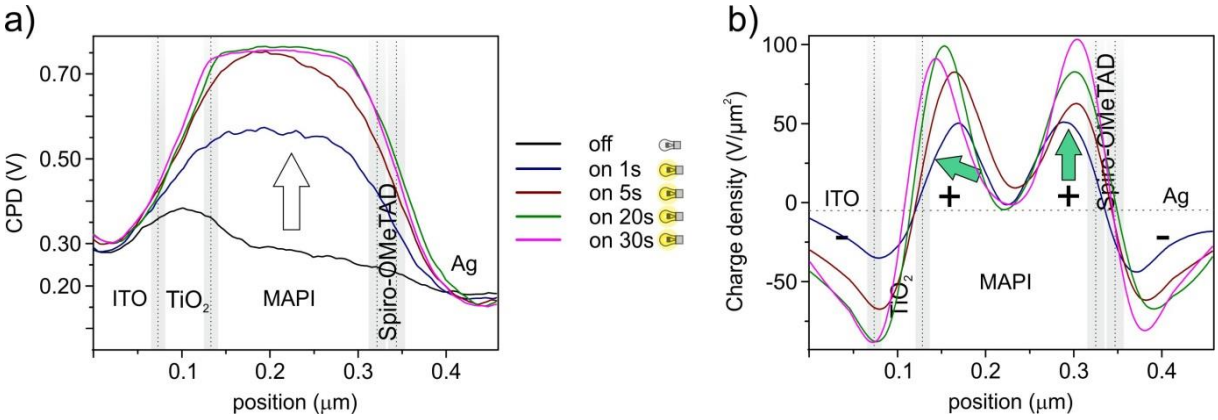

Figure 44: (a) CPD profiles for the flat-junction device structure with lower efficiency for dark conditions and distinct time steps after turning on the illumination. An increase in CPD during the illumination is observed, starting from the ITO/TiO_2 all the way to the HTL/Ag interface. After approximately 30 s the CPD is saturated and shows a flat potential from the TiO_2/MAPI interface up to ~50 nm in front of the HTL interface. (b) Positive charges accumulate in front of the selective interfaces, while negative charges are present on the selective interfaces/electrodes. The photo-generated charge distribution was calculated by using the Poisson equation. In order to extract the information about the changes in charge distribution appearing under illumination, the equilibrium profile was previously subtracted from the illuminated CPD profiles (photo-potential).

Upon illumination, the CPD within the perovskite MAPI directly increased by ~250 mV (Figure 44a) and then slowly (time scale of seconds) saturated up to an offset of +450 mV (after ~30 s).

By calculating the charge density distribution at certain time steps, the time-dependency for the distribution of charge accumulation upon illumination could be visualized (Figure 44b). After 1 s of light illumination, positive charges arranged in front of both selective interfaces, each causing a high density of positive charges in front of the interface inside the perovskite MAPI, while a higher density of negative charges screened these charges on both selective contacts. While the illumination was turned on, the charge density peak in front of the TiO_2 contact increased to almost double size and moved closer to the interface (approximately ~40 nm). Meanwhile, the charge density of positive charges in front of the HTL interface increased by a factor of 2 without any shift in location (Figure 44b – green arrows).

A fast increase in CPD, followed by a slow saturation could be explained by a combination of fast accumulating electric charges (or the formation of a surface dipole) followed by slower migrating ions. In particular, the migration of positive charged ions towards the TiO_2 interface correlates with the conclusions made when analyzing the measurements of the thick mesoporous device structure and the results from literature.[122, 124]

As the CPD distribution within the two flat-junction devices responded differently upon the illumination under short circuit conditions (namely with and without an

increase in the perovskite) there must have been a significant difference, which accordingly prevented the accumulation of holes or the formation of a surface dipole. Since these devices were fabricated in one batch, the surface was expected to be treated in the same way. However, unintentional self-doping could explain a difference in the respective CPD distribution and therefore also a shift of the respective band levels with changes in charge transfer properties. When considering the formation of a surface dipole, the alignment must have been quenched, whereas self-doping could have induced a surface coverage of the compact TiO_2 layer.

As a next step, the time-dependent dynamics of the charge re-arrangement upon illumination was calculated, by analyzing the respective increase in CPD over time.

The most intuitive way of calculating and locating the re-arrangement of charges upon external stimulation would have been the analysis of the changes within the charge density distribution. However, the calculation of the charge density distribution involved a smoothening step of the raw data (explanation see 3.3.6 Exemplification). Thereby, quantitative information about the magnitude of the exact charge distribution result in a loss in resolution during the calculation procedure. Therefore, a time-dependent analysis of the smoothed and calculated charge distribution data showed to be inaccurate (not shown).

In order to overcome the inaccuracy due to the small changes of noise within the CPD signal, but avoiding a smoothening process, an alternative way of analyzing the time-dependent processes was chosen. For each time step, the integral between the CPD profile for the time t and the initial dark profile at t = 0 was calculated and plotted versus time:

$$A(t) = \int CPD(x,t) - CPD(x,t=0)\,dx \tag{29}$$

The evolution of the integral within time is proportional to the re-distribution and accumulation of charges within the device. To get an estimation of the time constants, which represents the changes in CPD within the device, the data was then fitted with a single (A_{01}), a double (A_{012}) and a triple (A_{0123}) exponential decay fit.

$$A_{01,012,0123}(t) = a_0 + a_1 \cdot e^{-x/\tau_1} + a_2 \cdot e^{-x/\tau_2} + a_3 \cdot e^{-x/\tau_3} \tag{30}$$

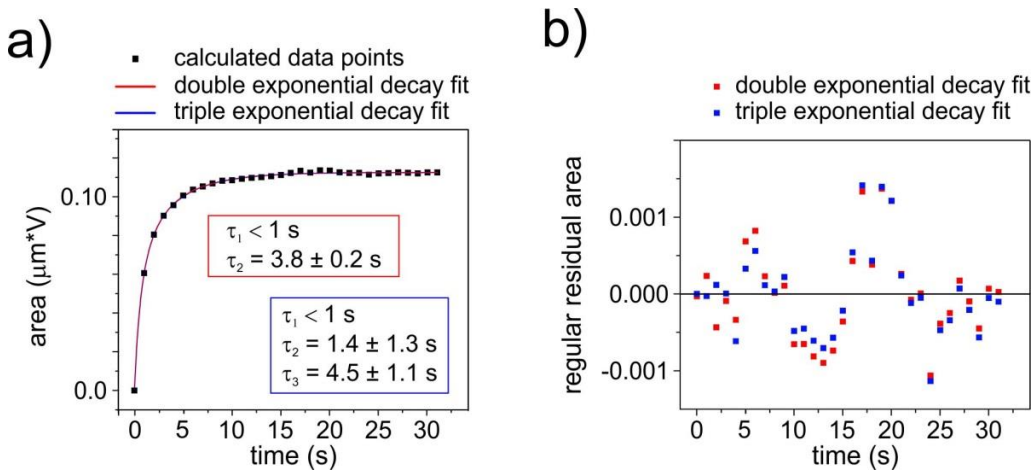

Figure 45: (a) The integrated area between the CPD profiles at time t and the initial dark profile is plotted versus time. The data is fitted with a double and triple exponential decay fit. The time constant τ_1 represents the fast electronic process and cannot be resolved since the time resolution of the measurement is 1s. The time constants $\tau_{2,3}$ represent a slower process, most likely an ion migration towards the interfaces. (b) Residuals for the corresponding exponential decay fits, with no significant improvement for the triple exponential decay fit.

While the single exponential decay fit did not converge (not shown) the double exponential decay fit did (Figure 45). Even though the double exponential fit already converged and gave a reasonable estimation of the data, it was still likely that even more processes in different time regimes could have occurred, which is why the triple exponential decay fit was also evaluated.[40, 44]

While the time resolution of the measurement was limited to the scanning speed of the 1 Hz line-by-line scan, the resolution for the evaluation of the time constants was 1 s accordingly. The first time constant τ_1 was lower than 1 s and thereby could not be resolved due to the limitation of the time resolution. Such a fast time constant was suggested to represent the fast-electronic process (accumulating photo-generated charges or the formation of a surface dipole), but it could also include a fast mobile ionic species.[113, 118] The other time constants $\tau_{2,3}$ were in the order of seconds and thereby represent a slower process, most likely connected with ion migration.
Both fits did not significantly differentiate (see residuals Figure 45b). When analyzing the residual sum of squares for both fits, the double exponential gave a value of $RSS = 1.17 \cdot 10^{-5}$ while the triple exponential fit gave $RSS = 1.05 \cdot 10^{-5}$. When considering the re-arrangement of ions, a process with two time-constants in the time scale of seconds could be related to ions with different mobilities. However, the errors (relative and absolute) of the time constants were significantly bigger for the triple exponential fit. Therefore, the analysis of the time-dependent increase in CPD was expected to be dominated by a fast process (electric charges or/and fast mobile ions) and only one slower process in the second regime (mobile ions).

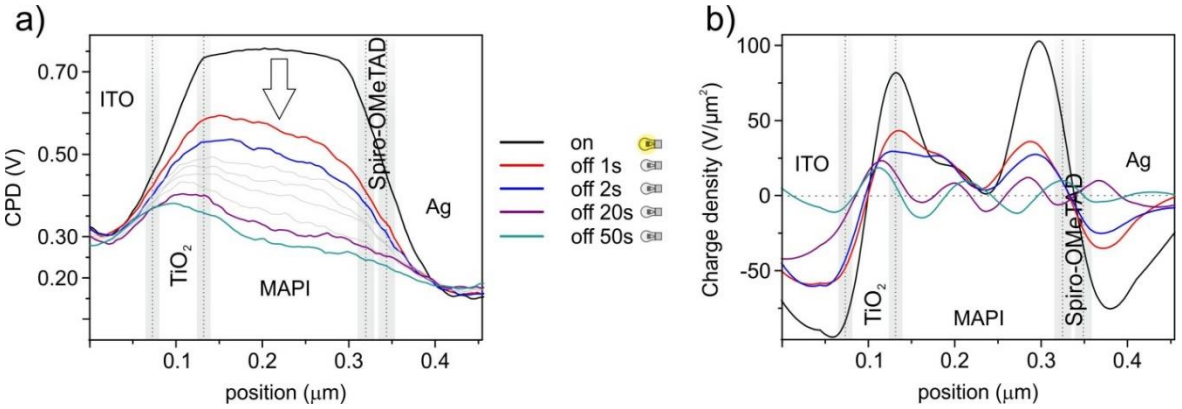

Figure 46: (a) CPD distribution for the scenario when the light is turned off. After a first pronounced drop in CPD, the decrease is slowed down and slowly saturates after ~50s. (b) The calculated charge distribution showing the excess charge carriers compared with the initial state. In font of both selective interfaces the amount of positive charges drops and then further slowly decays.

Light Off As a next step, the CPD profiles for a single line scan were recorded for the process of switching the illumination off again (Figure 46a). Within the first second, the CPD dropped about ~150 mV at the TiO_2 interface and ~250 mV in front of the HTL interface, which lead to a CPD distribution with a negative gradient within the MAPI layer. Afterwards, the CPD slowly decreased and saturated within ~50 s to the initial equilibrium distribution. The relaxation process thereby took around ~20 s longer than the charging process during illumination.
When switching off the illumination, the amount of positive charges in front of the selective interfaces significantly dropped already within 1 s and then further slowly decreased. This charge redistribution was suggested to be caused by a combination of charge extraction/recombination of electronic species at the interface (or the realigning dipoles) and a subsequent slow re-distribution of ionic species.
The time-dependent change of the CPD was again analyzed by first calculating the area between the CPD profiles for time t and the equilibrium dark CPD profile. A double and a triple exponential decay function were fitted to the data (Figure 47a). In this case, the triple exponential decay fit attained a three times lower residual sum of squares ($RSS = 2.19 \cdot 10^{-5}$) than the double exponential fit ($RSS = 7.60 \cdot 10^{-5}$) (compare Figure 47b). Hence, a tendency for three processes of charge re-arrangement, resulted from the analysis. In general, the time constants for the slower processes upon switching on the illumination appeared to be faster than the time constants for the relaxation process (compare Figure 45 & 47). An explanation could be that with the fast process of accumulating charges at the interfaces an electric field built up inside the perovskite layer and therefore the re-distribution process under illumination was influenced by drift, while the relaxation process was solely based on diffusion. Also a chemical reaction of mobile ions at the HTL interface was suggested to be the cause of a slowed down relaxation process.[92]

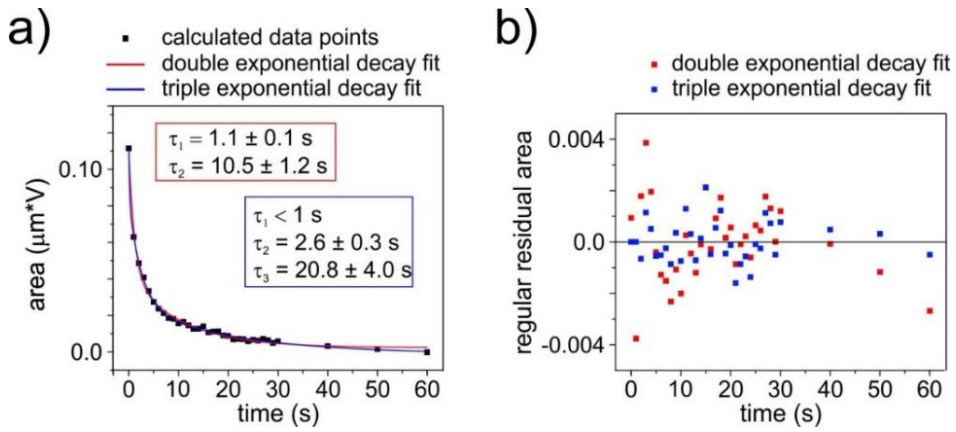

Figure 47 (a) Integrated area between the CPD profiles after illumination is turned off and the initial dark case versus time. The data is fitted with a double and a triple exponential decay fit. The fastest time constant represents the decay of electronic species and is expected to be significantly less than 1s. (b) Corresponding residuals for both fits with a lower residual sum of squares ($RSS = 2.19 \cdot 10^{-5}$) than the double exponential fit ($RSS = 7.60 \cdot 10^{-5}$). Therefore, the triple exponential decay fit is suggested to be representative for the time-dependency of the processes within the device.

The first process, represented by the fast time constant τ_1, must be connected with the fast-electronic decay of photo-generated charges or the re-aligning surface dipole. For the second and third process a re-arrangement of mobile ions is expected. As mentioned, the relaxation process is expected to be slower than the build-up. The second process could therefore be either related to trapped charges or a mobile ionic species with different mobility, which was too fast to resolve previously upon illumination (compare I^- and $CH_3NH_3^+$).[113, 118] The third and slowest process must thereby be the slower relaxation of the slow process, which was previously found during the time-dependent analysis upon illumination, most likely mobile ions.

4.2.3 Thin Mesoporous Perovskite Solar Cell

Light On Upon switching on the illumination for the thin mesoporous device structure, the CPD increased within the perovskite MAPI layer (Figure 48a), which was also observed for the thick mesoporous (Figure 40b) and the flat-junction device #2 (Figure 44a). However, the time-dependent increase of the CPD distribution inside the device showed to be more complex and had to be separated into different steps for the capping layer and the mesoporous layer.

Directly after the light was switched on, the CPD increased rapidly within the perovskite capping layer by ~450 mV, whereas a smaller increase of ~150 mV was observed within the mesoporous part (Figure 48a – red line profile). After that, the CPD increased further (another 100 mV) within the perovskite capping layer until it reached its maximum after about 5 s (Figure 48a – blue line profile).

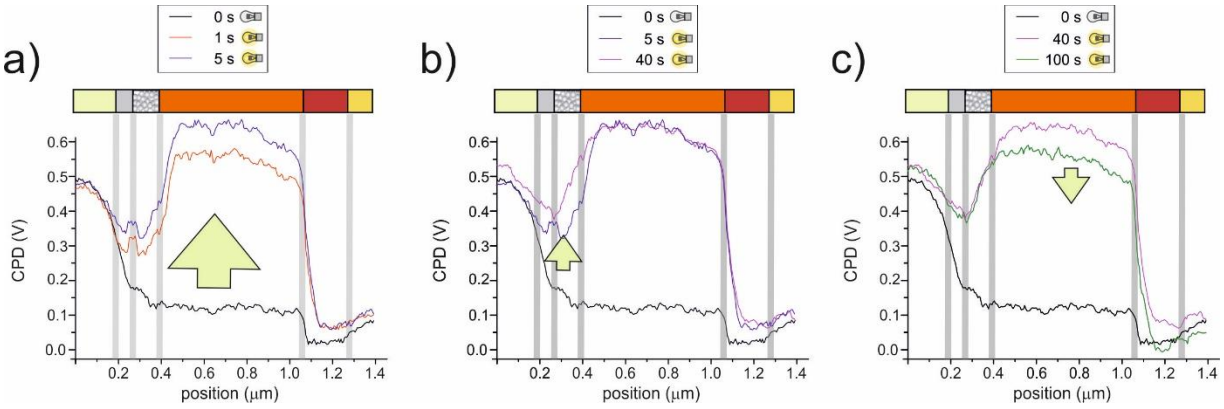

Figure 48: CPD profiles for the thin mesoporous device structure representing the dark case (black line profile) and the profiles measured for the illuminated case at certain time frames. (a) The CPD overall increases both in the mesoporous and the capping layer, which is pronounced with a big green arrow. (b) The CPD stays almost constant within the capping layer, while it increases within the mesoporous layer (small green arrow). (c) The CPD starts to decrease within the capping layer again.

In a second step the CPD stayed almost constant within the capping layer, whereas in the mesoporous part it increased by another ~50 mV until it saturated too after approximately 40 s (Figure 48b). In a third step, the CPD within the mesoporous layer stayed constant, while the CPD within the capping layer decreased again, saturating approximately after 100 s (Figure 48c).

In order to analyze the specific charge (re-)distribution for each part of the process, the photo-generated charge density distributions were calculated for the start and end of each interval which was mentioned previously (Figure 49). Within the first seconds (t = 5 s), positive charge carriers accumulated at both selective interfaces.

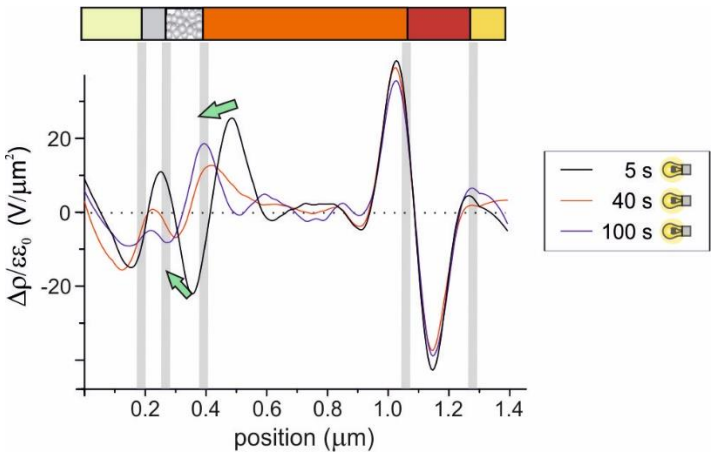

Figure 49: Photo-generated charge density distribution for turning on the light and after saturation. While positive charges accumulate at the perovskite/HTL interface within 5 s, the re-distribution of charges at the mesoporous/perovskite interface reveals a dynamic process. Positive charge carriers arrange in front of the mesoporous interface and within time slowly move into the mesoporous layer. Negative charges appear inside the mesoporous layer, close to the perovskite interface, but subsequently move towards the compact TiO_2 interface, while at the same time the amount significantly decreases.

While in the next tens of seconds, the positive charge carriers at the HTL interface only slightly increased, positive charge carriers on the other side were moving into the mesoporous layer (upper green arrow). After 100 s, the peak position of the positive charge density distribution at the TiO_2 side was exactly located on the mesoporous/capping layer interface, while the magnitude dropped by 20%. On the contrary, negative charges were already present within the mesoporous TiO_2 layer in the beginning (t = 5 s). This negative charge density almost completely descends, with only a marginal amount found at the compact layer/mesoporous interface for the subsequent time frames (lower green arrow).

The dynamics of the re-distributing charge carriers at the mesoporous TiO_2 interface can be explained, when taking the self-induced electric field distribution for the different time intervals into account (Figure 50). After the light was switched on, photo-generated positive charges accumulated within the perovskite capping layer, causing a strong electric field at each selective interface. This electric field then generated an electrostatic force on the mobile charges and therefore created a drift on positive charge carriers out of the perovskite capping layer. While holes could be extracted when they reached the Spiro-OMeTAD, positive ions were pushed into the mesoporous layer by the negative electric field, explaining the shift of the charge density peak positions of the positive charge density (Figure 49 - upper green arrow). The time intervals could thereby stand for the process of building up the electric field and a subsequent drift of ions towards the mesoporous/capping layer interface and finally into the mesoporous layer.

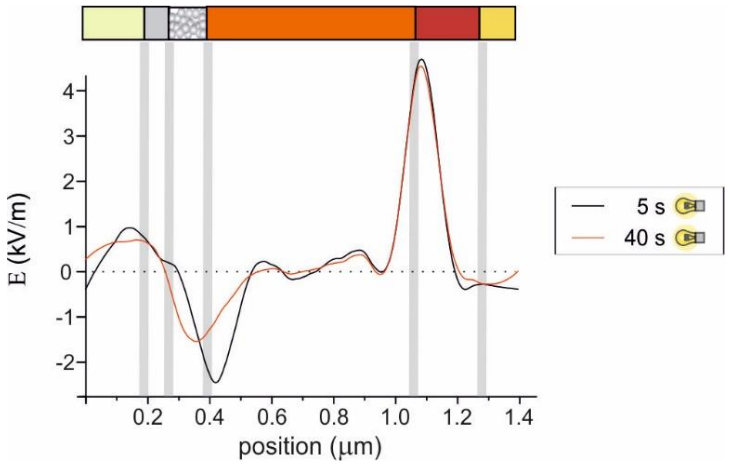

Figure 50: Electric field distribution for the characteristic time steps t = 5 s and t = 40 s. After 5 s a negative electric field of ~-2.5 kV/m developed at the mesoporous/capping layer interface, whereas a positive field of ~4.7 kV/m developed at the capping/HTL interface. After 40 s the negative electric field shifted into the mesoporous layer, which can be explained by a drift of positive charged ions.

The third process was the subsequent decrease of the CPD within the perovskite capping layer (Figure 48c). An explanation could be that ions which drifted into the mesoporous/MAPI layer were screened by additional electrons in the TiO_2. This screening effect then caused the potential drop across the TiO_2 to decrease. Hence, after 40 s of illumination, a higher ratio of ions started to drift into the mesoporous layer compared to ions that accumulate in front of the mesoporous interface. This process would then accordingly result in additional remaining positive ions within the mesoporous layer, when switching off the light, similar to the thick mesoporous device (Figure 40b). To elucidate the dynamics of the migration process, the integrals between the CPD profiles and the equilibrium dark profile was calculated for the first 40 seconds. After 40 s the screening of the migrating ions in the mesoporous scaffold hides this dynamic when analyzing only the integral. Therefore, only the data for the first 40 s was fitted with a double exponential decay function (Figure 51). The fit revealed a fast time constant $\tau_1 < 1$ s and a slower time constant $\tau_2 = 3.0 \pm 1.3$ s. The slower time constant was therefore suggested to represent the ion migration solely within the perovskite capping layer.

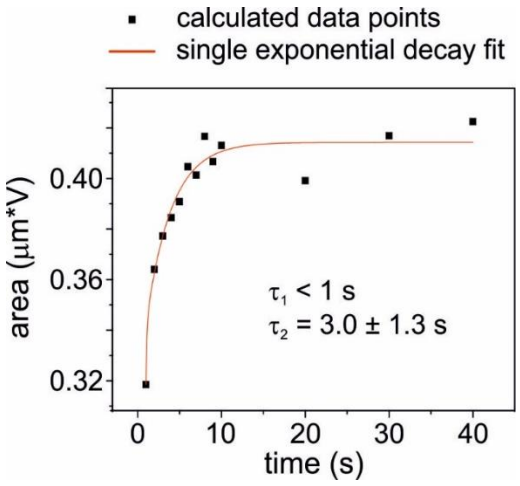

Figure 51: The data points represent the integrated area between the respective CPD profiles for each time step after the illumination was turned on and the dark case. The time period is limited to the first 40 s, to avoid a further overlap of the process leading to a decrease of the CPD after 40 s. The data is fitted with a double exponential decay fit, giving a time constant of $\tau_1 < 1$ s and a time constant $\tau_2 = 3.0 \pm 1.3$ s. A triple exponential decay fit was also used, but ended up in two almost identical time constants $\tau_2 \approx \tau_3$.

Light Off Directly after switching off the light, a rapid drop in CPD of about ~450 mV occurred in the perovskite capping layer (Figure 52), followed by a more monotonous decrease which homogeneously developed over the TiO_2/perovskite MAPI layer. A bump in CPD profile across the mesoporous TiO_2 layer was observed, which then slowly decreased within time. After 100 s the CPD almost returned to the equilibrium state over the complete layer structure.

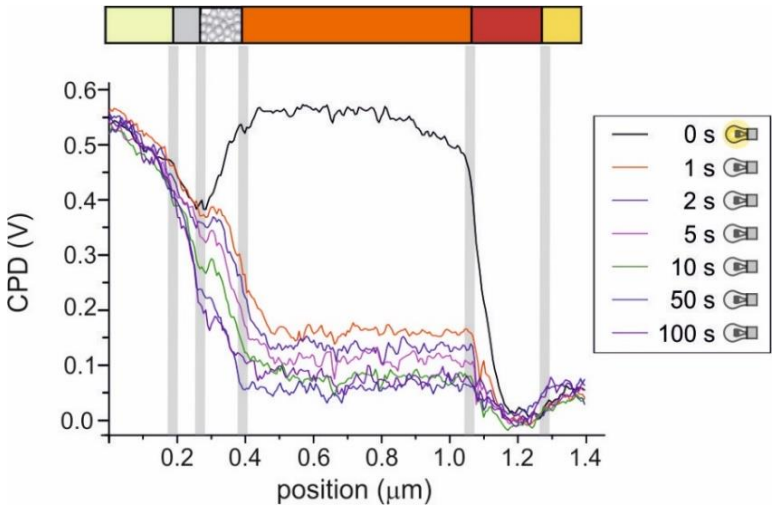

Figure 52: CPD distribution for the time after illumination. The CPD starts to decrease again, as soon as the light is switched off. While an rapid drop of ~450 mV is observed in the perovskite capping layer directly after 1 s, the further decrease happens on a much slower time scale throughout the device.

Upon switching off the light and the initial fast decay of the electric charges, positive charge carriers were observed in the mesoporous layer (~1s – Figure 53). These remaining positive charge carriers were expected to be the ions, which have previously migrated into the mesoporous layer explained in the third process (Figure 48c). The ions then slowly migrated out of the mesoporous layer by a combination of self-induced drift and diffusion (Figure 53 green arrow).

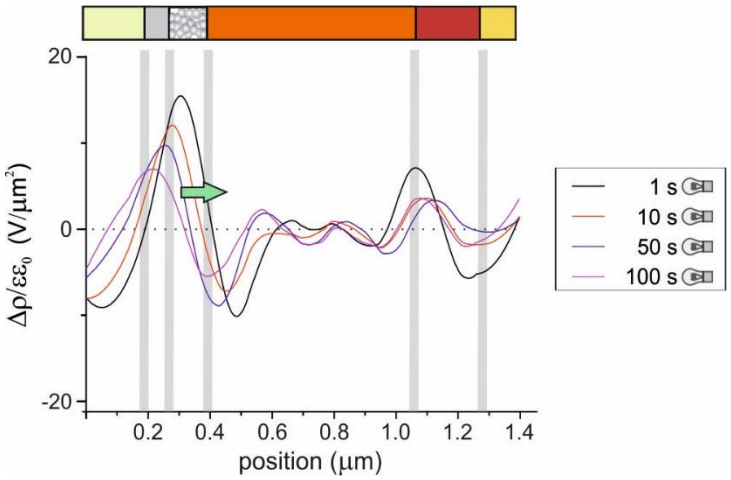

Figure 53: Charge density distribution for the remaining charge carriers after illumination, calculated by subtracting the equilibrium profile from the light biased profiles for each time step and subsequently building the second derivative (with each time smoothening). When the light is switched off and photo-generated charges are gone, remaining positive charges carriers are visible deep inside the mesoporous layer, close to the interface to the compact TiO_2 layer. These remaining positive charge carriers create a field, which slowly pushes out the excess charges starting at the mesoporous/perovskite interface. Thereby the amount of charges is reduced from right to left (indicated by the green arrow).

In order to analyze the time-dependency for the process of charge re-arrangement after the light was turned off the integral of the photo-potential was calculated for each time step and fitted with a double exponential decay fit (Figure 54). The process of charge re-arrangement after the light was turned off had a slower time constant (τ_2 = 8.5 ± 1.5 s) compared with the time constant representing the increase of CPD under illumination (τ_2 = 3.0 ± 1.3 s) (see Figure 51). The slower dynamics of the relaxation process compared with the re-arrangement under illumination could be again explained by the differences in the electrostatic force on the migrating charges due to the electric field for each state. In the illuminated case, the photo-generated charge carriers (or surface dipole) generated a field ($E \approx -2.5\ {}^{kV}/_{m}$) at the mesoporous/MAPI interface, whereas in the case after illumination remaining charge carriers in the mesoporous layer generated a self-induced field of only ($E \approx 1.7\ {}^{kV}/_{m}$), which then even further decreased in time with ions migrating back into the perovskite capping layer. Hence, less driving force was exerted on the ions when the light was turned off, causing the relaxation into the equilibrium to be slower than the initial re-arrangement.

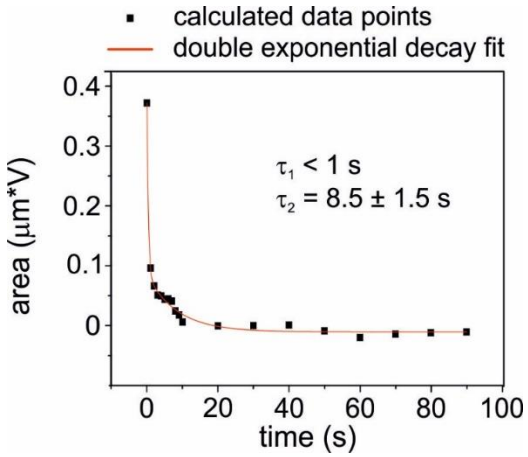

Figure 54: Time dependent change of the integral between the CPD profiles after illumination and the equilibrium state. A double exponential decay fit is used to fit the data and receive the corresponding time constants. A triple exponential fit was also tried, but generated time constants with errors bigger than the difference between the time constants itself. While the first time constant represents the fast electronic decay (extract/recombination) the second time constant represents the remaining excess positive charge carriers, which slowly migrate back into the perovskite capping layer with a time constant of τ = 8.5 ± 1.5 s.

4.2.4 Discussion

Short circuit conditions under operation were studied, by setting both electrodes to ground, while illuminating the device with a broad band white light source. For three out of four devices an increase in CPD was observed within the perovskite MAPI layer (Figure 55).

With the integral of the photo-potential for each time step, the time dependency for the increase in CPD could be studied. By fitting the data with a double (triple) exponential decay fit, time constants representing different processes on at least two timescales were identified (Figures 45/47/51/54):

1. a fast time constant in the sub-second regime represented a fast, initial electronic process

Two possible explanations for the fast increase in CPD upon illumination are the accumulation of holes, due to an unbalanced charge transport between holes and electrons and/or the formation of a surface dipole at the TiO_2 interface. Recently, the theory of unbalanced charge transport has been complemented with the assumption that unequal interfacial recombination rather than charge extraction is creating the accumulation of positive charges within the perovskite (Figure 56).[92]

With a higher interfacial recombination of electrons at the Spiro (HTL) compared to holes at the TiO_2 more holes than electrons are present within the perovskite. Holes directly accumulate at the HTL interface and further spread towards the TiO_2 to form a field-free perovskite bulk (see Figure 55).

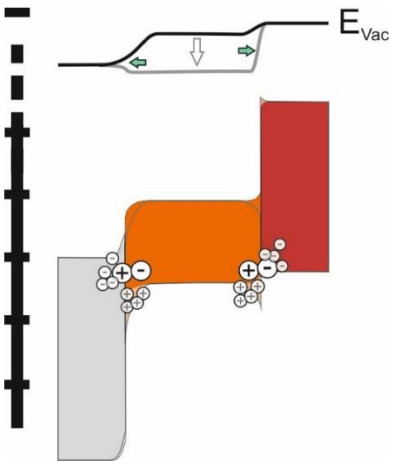

Figure 55: The energy diagram of the perovskite layer, sandwiched between the charge selective layers, with charge accumulation at the selective interfaces. With the additional positive charges within the perovskite layer, the vacuum level shifts (white and green arrows), which was observed as an increase in CPD for the KPFM measurement. Charge accumulation and a connected re-arrangement of ions results in an additional band bending at the selective interfaces. Negative charges on the selective layers screen the accumulated positive charge carriers towards the electrodes, which causes additional band bending (green arrows).

Subsequent to the fast increase in CPD a second slower process was observed:

2. the correlating slower time constant(s) in the time scale of seconds was suggested to represent a process of migrating ions/vacancies

The slower process suits the scenario of mobile ions re-arranging at the selective interfaces, within the perovskite layer. By calculating the charge density distribution at certain time steps a migration of a positive charge density peak towards the TiO_2 interface has been observed, which suits a confined accumulation of ions at that interface (Figure 44b/49). After turning off the light for the mesoporous device structures, excess positive charged ions remained in the mesoporous layer (Figures 41/53). A closer look on the charge density distribution revealed that after turning off the light these excess positive ions went back to the equilibrium state by migrating out of the mesoporous layer (Figure 53).

To sum it up, unbalanced interfacial charge recombination, which is leading to an accumulation of holes at the interfaces inside the perovskite layer, is expected to be the cause of the initial fast increase in CPD upon illumination.[92] In addition, the unbalanced interfacial recombination could be controlled by small variations in the self-doping of the MAPI, as well as the conditions of the selective contacts. With the accumulation of the longer living positive charges in front of the selective contact and respective negative charges at the interface of the grounded electrode an electric field is formed during illumination on each selective interface (Figures 42/50).

This electric field could then be strong enough to induce the second slower process of ion migration e.g. towards the TiO_2 interface or even into the mesoporous perovskite phase, as previously suggested by Wu et al..[122]

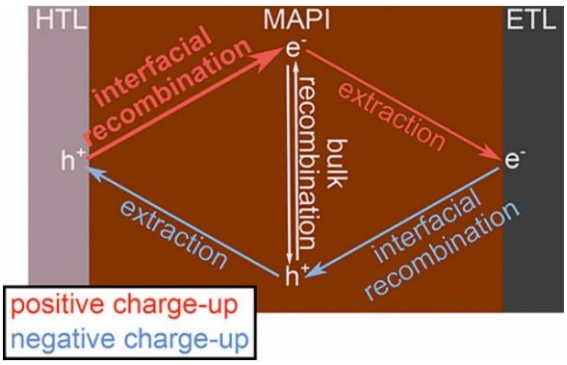

Figure 56: Pathways for charge carriers of extraction and recombination within and at the interfaces of the perovskite layer. While the white pathway keeps a balance of positive and negative charges (bulk recombination), the blue pathway creates a higher density of negative charges while the red pathway creates a higher density of positive charges. "Reprinted with permission from (J. Phys. Chem. Lett. 2018, 9, 21, 6249-6256 Copyright (2018) American Chemical Society."[92]

4.3. Open Circuit Conditions

For the setup of the cross-section measurements, open circuit conditions were easily achieved by taking one electrode off ground (floating). With one electrode floating under illumination, photo-generated charges were collected on the electrode until charge extraction and respective charge recombination at this selective interface reached equilibrium.

In this chapter I will present the CPD measurements, performed under open-circuit conditions, for all three device structures. The cross-sectional studies thereby revealed information whereabout the open circuit potential inside the device develops and where the CPD drops in case of a connected external load. Furthermore, the built-up of the open circuit potential on one of the electrodes changes the electric field and thereby also the ion migration, within the device.

4.3.1 Mesostructured Perovskite Solar Cell

Open-circuit measurements were performed for both cases of leaving one electrode floating during illumination (Figure 57). Thereby the CPD on the floating electrode developed a difference of ~900 mV compared to the initial profile measured under dark conditions (white arrows). The difference between the dark and the illuminated CPD profiles (photo-potential) developed across the perovskite capping layer, saturating on the respective floating electrode (Figure 58).

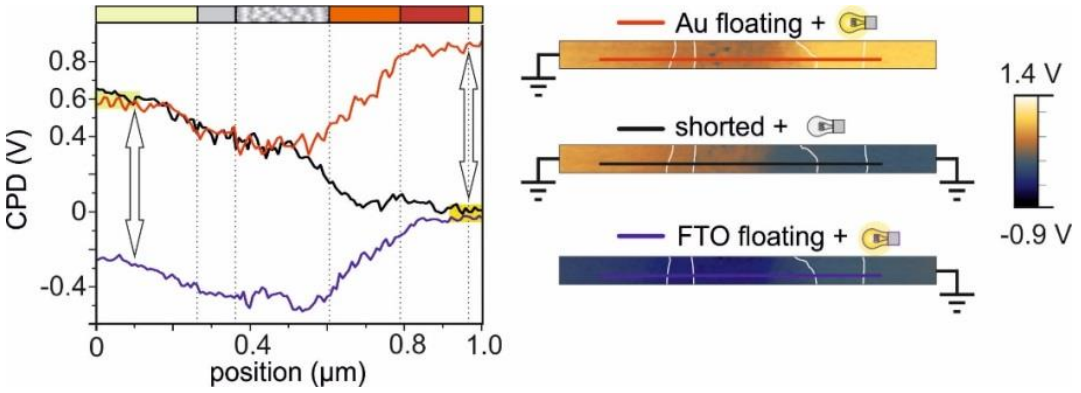

Figure 57: CPD distribution for equilibrium in dark (black line profile) and the respective CPD distributions under illumination, leaving the Au electrode floating (red line profile) and leaving the FTO electrode floating (blue line profile). Upon illumination and leaving one electrode floating, the open circuit potential builds up on the respective electrode (white arrows). The additional photo-potential thereby develops across the perovskite capping layer and stays constant upon the selective interfaces.

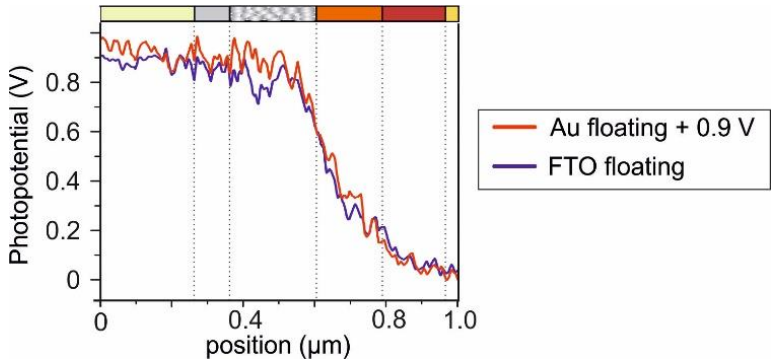

Figure 58: Photopotential that builds up at open circuit conditions under illumination. The red line profile represents the difference between the illuminated open circuit condition leaving the Au electrode floating and the equilibrium profile measured in dark, while the blue line profile represents the respective case leaving the FTO electrode floating. In order to be able to compare both profiles, an additional 0.9 V was added to the profile for leaving the Au electrode floating. Both profiles overlap within the resolution of the measurement. The open circuit potential develops across the perovskite capping layer.

In case of a floating FTO electrode, the photo-potential saturated in the mesoporous layer, while in case of a floating Au electrode, the CPD saturated within the Spiro-OMeTAD. Therefore, the open circuit potential already fully developed on the selective contacts, which was previously suggested by Qin et al..[125] In their studies, they analyzed open circuit potentials with KPFM measurements by comparing the CPD for the dark and illuminated case on top of a perovskite solar cell without top electrode (V_{OC} on the Spiro-OMeTAD).

For open circuit conditions, negative charges accumulated inside the mesoporous layer, while positive charges were present within the perovskite capping layer and the Spiro-OMeTAD (Figure 59). The presence of positive charges within the perovskite capping layer has also been observed for illuminated short circuit conditions and was expected to have the same origin (Figure 41).

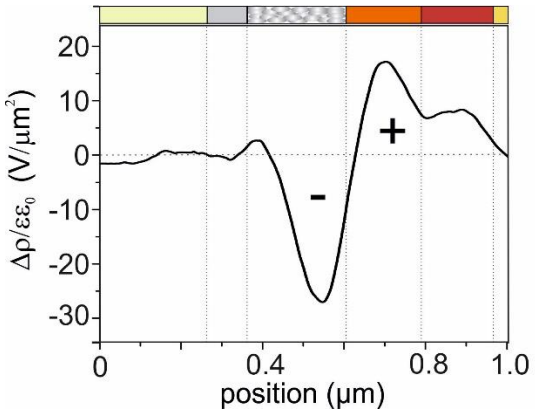

Figure 59: Charge density profile for the respective photo-generated charge distribution under illumination leaving one of the electrodes floating. Since the same trend in photo-potential for both cases of floating electrodes is observed in Figure 52, the average of the photo-potential was calculated to determine the charge density distribution. While negative charges are present within the mesoporous layer, positive charges are present within the perovskite capping layer.

As these changes in charge distribution were analyzed with respect to the equilibrium, the question arises:

How does the charge distribution change from illuminated short circuit conditions to illuminated open circuit conditions?

From analyzing the change in charge density distribution upon switching from short- to open circuit conditions, it was noticed that negative charges assemble in front of the Spiro-OMeTAD while positive charges assemble in the Spiro-OMeTAD (Figure 60). According to that, the major changes in charge distribution upon switching from short- to open-circuit conditions occur at the Spiro-OMeTAD interface. The CPD at the mesoporous/MAPI interface however does not differ considerably between open-circuit and short circuit conditions (compare Figure 40b & Figure 57).

Notice:
The time dependency of the CPD upon changing from short to open circuit conditions could not be analyzed from the measurements for the thick mesoporous device due to the same circumstances already mentioned in the short circuit conditions section.

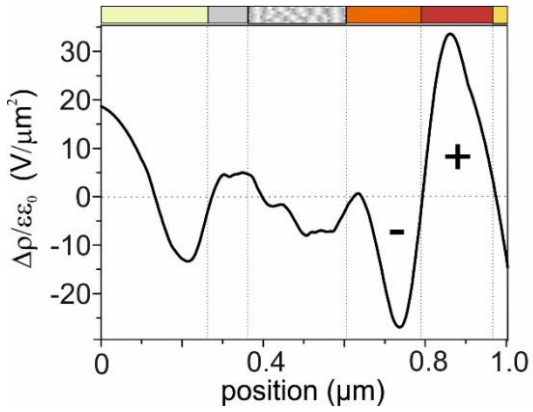

Figure 60: Averaged charge density distribution showing the additional charges when switching from illuminated short- to open circuit conditions. Since the short circuit conditions under illumination revealed positive charges within the perovskite capping layer, the major changes appear at the perovskite/Spiro-OMeTAD interface with additional negative charges in the perovskite capping layer and an increase of positive charges on the Spiro-OMeTAD.

4.3.2 Flat-Junction Perovskite Solar Cells

Flat-Junction Device #1, Open-Circuit Conditions In the CPD profile for the equilibrium state a distinct potential drop at the TiO_2 interface has been observed towards the perovskite layer (Figure 61a – black line profile). As already discussed in the short circuit section, these drops in CPD were most probably formed from a re-arrangement of ions under the electric field of the p-i-n junction.

After leaving one of the electrodes floating and turning on the illumination, a difference in CPD built up on the respective floating electrode (white arrows). For a floating Ag electrode, a difference of $\Delta CPD = 850$ mV was measured on the Ag electrode and for the floating ITO electrode $\Delta CPD = -830$ mV was measured on the ITO. With an open circuit voltage of $V_{OC} = 0.9$ V, previously measured in the JV-scan (Figure 30a), the values of the respective change in CPD corresponded well with the external JV measurement. Similar to the CPD measured under dark conditions, the CPD profiles for open circuit conditions had a field-free perovskite bulk, with the drops in CPD confined to the selective interfaces. With the respective calculated photo-potential it could be identified that a drop in CPD of -600 mV developed across the TiO_2, which was almost completely confined to the TiO_2/perovskite interface (Figure 61b). A smaller drop in CPD of 200 mV developed across the Spiro-OMeTAD.

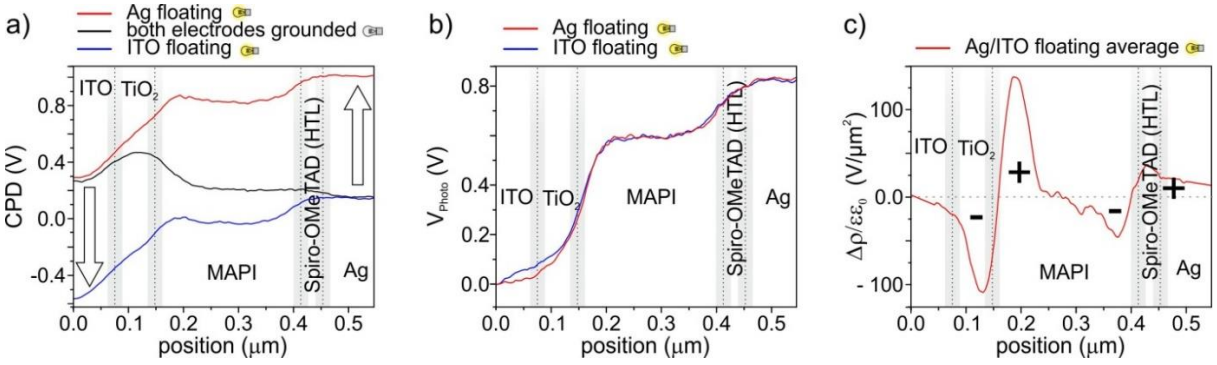

Figure 61: (a) CPD distribution for the initial dark case (black line profile) and the open circuit conditions under illumination leaving the Ag electrode floating (red line profile) or leaving the ITO electrode floating (blue line profile). The open circuit potential builds up on the respective floating electrode (white arrows). (b) The respective photo-potential calculated from (a). The open circuit potential mainly develops across the TiO_2 interface revealing a potential difference of $\Delta CPD = 600$ mV, while a smaller drop in photo-potential observed at the Spiro-OMeTAD interface with $\Delta CPD = 200$ mV. The perovskite bulk stays field free, due to charges, which arrange in front of the selective interfaces in order to screen the collected charges on the electrodes. In (c) the charge density distribution of the additional photo-generated charges is shown.

Time Dependency – Ag Electrode Floating After switching from equilibrium dark to open circuit conditions and recording the same line profile in time, the CPD distribution changed steadily until a saturation was reached after ~20 s (Figure 62a). While the initial buildup of the open circuit potential on the electrode took place on a time scale much faster than the time resolution of the measurement, an additional much slower change in the CPD distribution could still be recognized. In comparison to the line profile measured after 2 s under open circuit conditions, the line profile measured after 20 s had a significant increase of ~100 mV in front of the TiO_2 interface, which developed across the entire perovskite layer up to the Spiro-OMeTAD interface. With the calculated charge density distribution profile it could be shown that within time more positive charges accumulated in front of the TiO_2 (Figure 62c - green arrow), whereas negative charges accumulated on the TiO_2.

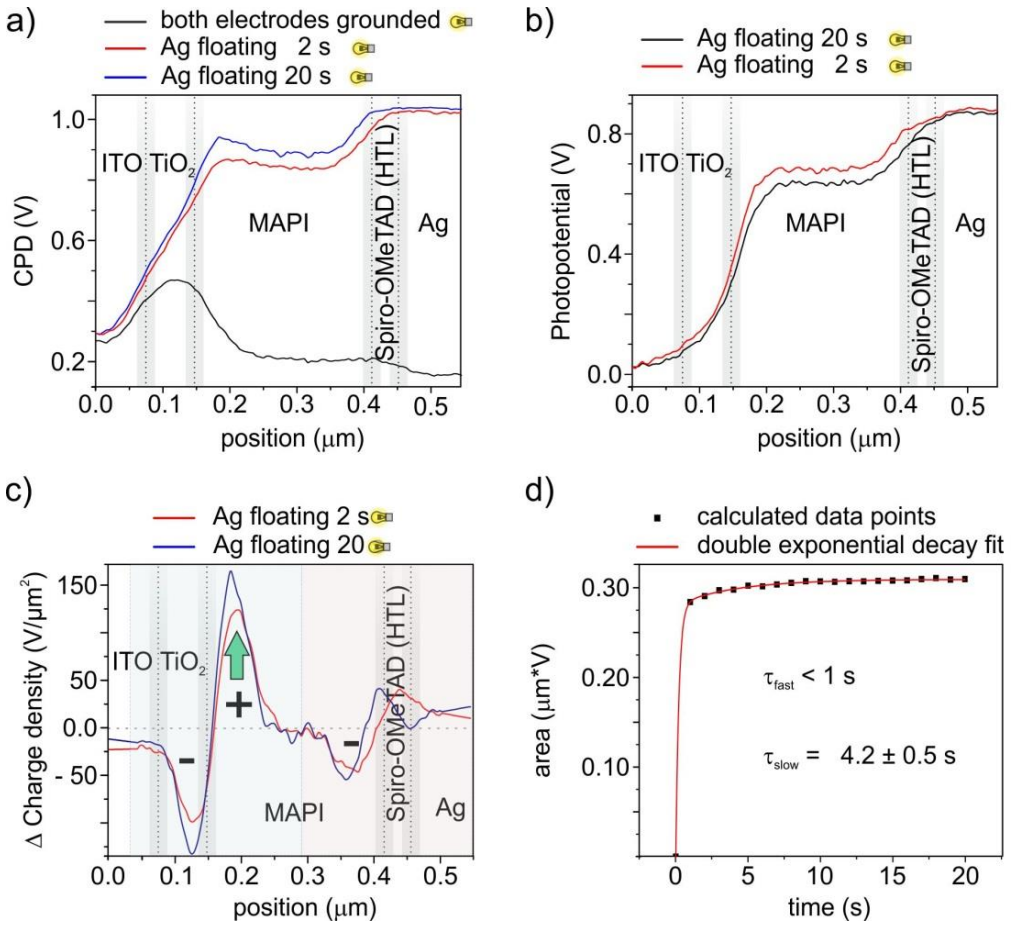

Figure 62: (a) CPD profiles measured in dark (black line profile) after 2s under open circuit conditions upon illumination (red line profile) and respectively after 20s (blue line profile). The comparison of the profiles measured after 2s and after 20 s reveals an increase of ~100 mV inside the perovskite, which is most pronounced in front of the TiO_2 interface. (b) Corresponding photo-potential calculated by subtracting the equilibrium profile from the profiles measured under illuminated open circuit conditions. (c) The charge density distribution of the photo-generated charges, calculated from the photo-potential, shows an increase of positive charge carriers in front of the TiO_2 and an increase of negative charges on the TiO_2. (d) The integrated area between the open circuit and the initial dark conditions is plotted versus time and fitted with a double exponential decay fit, resulting in τ_{slow} = 4.2 ± 0.5 s for the slow time constant.

For the analysis of the time dependencies, the integrated area between the profiles measured under open circuit conditions and equilibrium condition was plotted against time (Figure 62d). A double exponential decay function was used to fit the data and determine the time constants of the internal processes. The first time constant $\tau_{fast} < 1s$ represents the electronic process of the open circuit potential generation. However, the second time constant $\tau_{slow} = 4.2 \pm 0.5$ s represents the process which caused the slow increase in CPD inside the perovskite layer.

As the changes in CPD were supposed to be caused by a dynamic process of migrating ions/charges across the perovskite layer, a second more local time-dependent analysis was developed (equation 31). The profiles were divided in two halves, to separate the charge dynamics in front of both selective interfaces from each other (Figure 62c green and red area). For this analysis, the position of the integral for the photo-potential on the Ag side needed to be defined as the new reference point, by subtracting its value of photo-potential from all the following points:

$$A(t) = \int_{p_1}^{p_2} \big(CPD(x,t) - CPD(x,t=0)\big) - \big(CPD(p_1,t) - CPD(p_1,t=0)\big)\, dx \quad (31)$$

This procedure made sure, that all the information about time dependent changes from the ITO side was excluded from the Ag side. The time-dependent increase on the ITO side (Figure 63a) and decrease on the Ag side (Figure 63b) represents the changes of the opposed charge accumulation on each perovskite/selective contact (Figure 62c). While for the ITO side a slow time constant for the double exponential decay fit of $\tau_2 = 4.6 \pm 0.9$ s was calculated, the corresponding time constant for the Ag side was $\tau_2 = 3.5 \pm 1.0$ s.

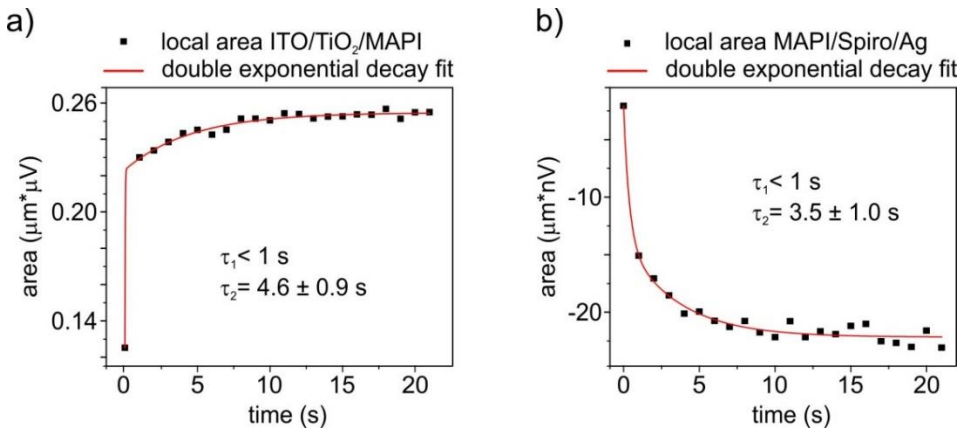

Figure 63: (a) Time-dependency of the integrated photo-potential increase for the defined area of the ITO/TiO_2/perovskite half marked in Figure 62c (green). (b) Time-dependency of the integrated photo-potential decrease for the defined area of the perovskite/Spiro/Ag half marked in Figure 62c (red). Each set of data points is fitted with a double exponential decay fit. The slow process on the ITO side ($\tau_2 = 4.6 \pm 0.9$ s) showed to be slower than the process on the Ag side ($\tau_2 = 3.5 \pm 1.0$ s).

A slow process of re-arranging charges at the interfaces under the preconditioning arrangement of illuminated open circuit conditions altered the overall CPD distribution and was expected to slowly return to the equilibrium state when the light was turned off again. However, instead of a slow decrease in CPD, the CPD immediately jumped to a lower level in CPD compared to the equilibrium profile, followed by an increase until the distribution reached the equilibrium state (Figure 64a).

Already after 1 s, the CPD had jumped below the equilibrium profile, starting from the ITO/TiO_2 interface and spreading across the device up to the Spiro-OMeTAD, with a maximum difference of ~50 mV inside the perovskite layer (Figure 64a – red line profile). The lower CPD within the perovskite layer corresponded to negative charge carriers, which were present in front of both selective contacts, while positive charges were present on the selective contacts to screen the electric field towards the grounded electrodes (Figure 64b).
A possible explanation for the observed changes in CPD is that directly after switching off the light, the previously collected photo-generated holes got extracted or recombined, leaving behind longer living species of ions or trapped charges. The time dependent saturation of the relaxation process in the integrated CPD with the corresponding exponential decay fit resulted in a time constant of τ_{after} = 8.8 ± 1.1 s (Figure 64c). The time constant calculated for the relaxation process was thereby twice the time constant determined for the overall increase, when the light was turned on (compare Figure 62d - τ_{slow} = 4.2 ± 0.5 s).

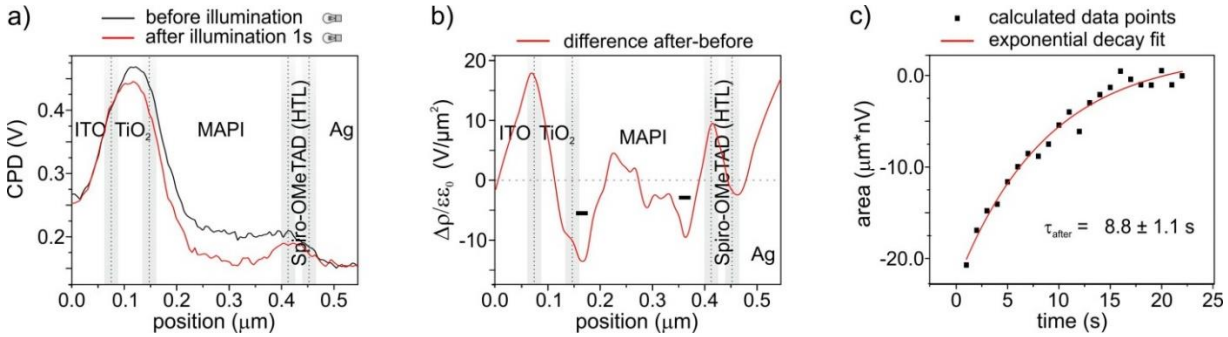

Figure 64: (a) CPD distribution for the initial profile measured in dark before illumination and after switching off the light. Directly after switching off the light, the CPD distribution within the perovskite layer is lower (up to -50 mV) than the initial profile. (b) The excess charge density reveals negative charges within the perovskite in front of both selective contacts, while positive charges on the selective contacts screen the field towards the grounded electrodes. (c) The integrated are between the profiles measured after switching off the light and the initial profile, shows a single exponential decay trend. The corresponding fit results in a time constant of τ_{after} = 8.8 ± 1.1 s.

The relaxation process under open circuit conditions for flat-junction device #1 also significantly differed from the observations made from the relaxation process of the other devices under short circuit conditions. For the other devices a steady decrease in CPD was observed without any jump towards a negative offset. A possible explanation for the excess negative charges after illumination could be electrons, which were trapped in ion vacancies or lead clusters.[126, 127]

ITO Electrode Floating Measurements of the time dependent increase in CPD under illumination with the ITO electrode left floating, corresponded with the measurements of Ag floating conditions. The time dependent ΔCPD developed in front of the TiO_2 and across the TiO_2/ITO interface with a total increase in CPD of ~100 mV on the ITO (Figure 65a). This time dependent change in CPD on the ITO could have been caused by a shift of the band levels at the perovskite/TiO_2 interface, due to the accumulation of positive ions (Figure 65b), and thereby less energy loss in the electron transfer towards the electrode.

For both options of a floating electrode while illuminating, the accumulation of ions in front of the TiO_2 lead to a time dependent increase of ΔCPD towards the direction of the floating electrode (compare Figure 62a – Ag floating/Figure 65a – ITO floating).

After the light was switched off, the CPD within the perovskite layer jumped to a level below the equilibrium state, similar to what has been observed for Ag floating conditions (Figure 66a). Additional negative charges were present in front of the selective contact within the perovskite MAPI layer (Figure 66b).

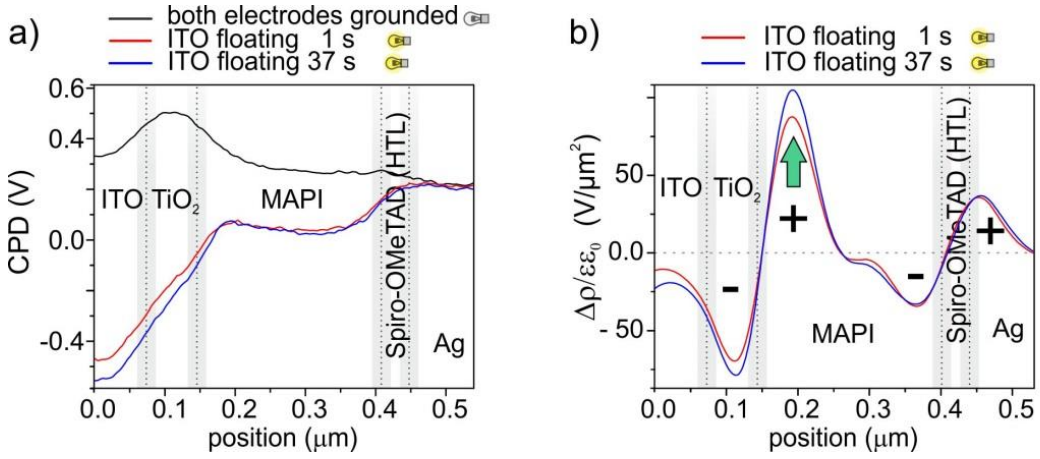

Figure 65: (a) CPD profiles for open circuit conditions under illumination leaving the ITO electrode floating. The CPD shows a time dependency across the MAPI/TiO_2 interface up to the ITO. In time, the CPD decreases, which reveals (b) an increase of positive charges in front of the TiO_2 (green arrow) as well as an increase of negative charges on the TiO_2.

Summing up, the same processes, both for switching on and off the illumination, could be observed for either leaving the ITO or the Ag electrode floating. The fact that the results are independent from which side is charging up, is another proof that the FM-KPFM measurements do not suffer from a cross talk averaging effect over the dimensions, which were studied (see section 3.3.2 AM-/FM-KPFM – Figure 16; more details following in chapter 4.5).

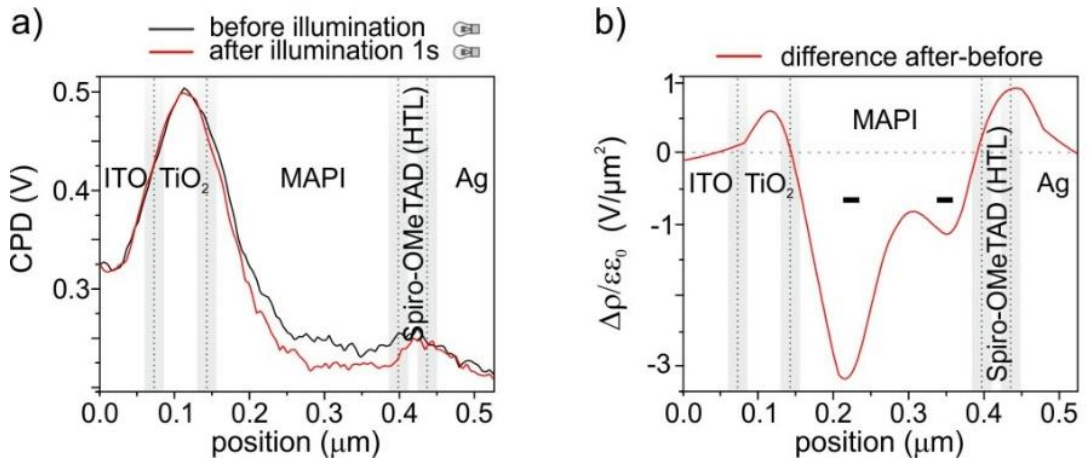

Figure 66: (a) CPD profiles for the time before and after illumination under open circuit conditions leaving the ITO electrode floating. Similar to the measurements, when the Ag electrode was left floating, the CPD after illumination shows a negative offset compared with the CPD before illumination. (b) The difference of the CPD profiles occurs due to additional negative charges inside the MAPI, which are mainly present in front of the interfaces.

Flat-Junction Device #2, Open-Circuit Conditions Flat-junction device #2 had a similar CPD distribution under open circuit conditions compared to flat-junction device #1. Keeping one electrode floating while illuminating the device, resulted in the buildup of the open circuit potential $V_{OC} \approx 0.9$ V on the respective electrode (Figure 67a - white arrows). The photo-potential thereby developed across each selective interface, while the bulk perovskite MAPI stayed almost field free having a plateau in photo-potential within the perovskite (Figure 67b). The magnitude of the drops in CPD were almost equally distributed with $\Delta CPD = 0.5$ V at the TiO_2/perovskite interface and $\Delta CPD = 0.4$ V across the Spiro-OMeTAD. These drops in CPD at the interfaces with a field free perovskite bulk formed due to the local arrangement of oppositely charged carriers around the selective interfaces (Figure 67c).

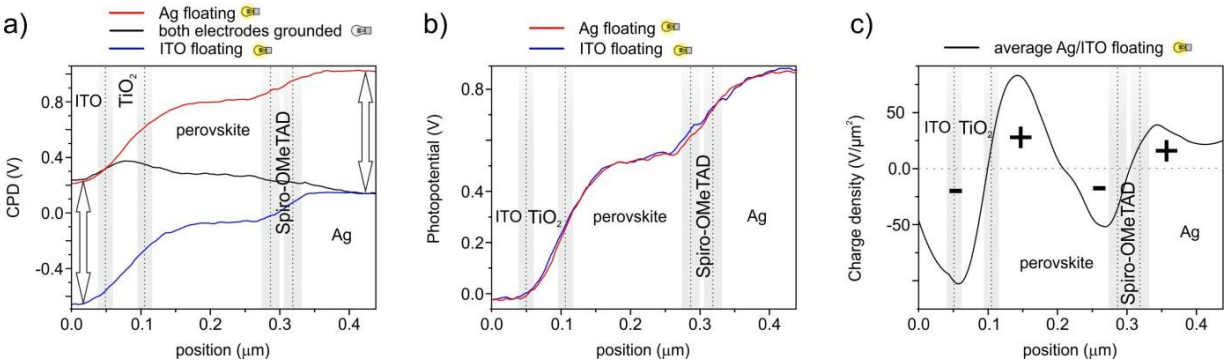

Figure 67: (a) CPD distribution of the open circuit conditions for the flat junction device with lower efficiency. The open circuit builds up on the floating electrode, respectively. (b) The difference between the illuminated and the non-illuminated CPD results in the photo-potential. In case of the ITO photo-potential, the V_{OC} is added in order to bring both photo-potentials on the same level. While the potential develops at the TiO_2/perovskite interface with 0.5 V and across the Spiro-OMeTAD with 0.4 V, the bulk of the perovskite stays field-free. (c) The charge density distribution reveals positive charges in front of the TiO_2 and negative charges in front of the Spiro-OMeTAD, which arrange in order to screen the open circuit potential to the inside.

An analysis of the time-dependent processes under open circuit conditions as made for the first flat junction device (Figure 63/64) would directly overlap with the process observed for illuminated short circuit conditions. Two processes namely turning on the light and switching from short to open circuit conditions subsequently add up in the measurement. The time dependency of changes in CPD upon illuminated short circuit conditions has already been analyzed in the previous chapter (Figure 45/Figure 47). As this process cannot be separated from the process of switching towards illuminated open circuit conditions, the analysis of the time-dependent processes under open circuit conditions could not be made. In order to overcome this problem, the experiment would have been optimized by first switching to open circuit conditions and then turning on the illumination. Here, the illumination was first turned on and then one of the electrodes was set floating. Thereby there was a small delay between the two processes, which makes the time dependent analysis less accurate. On the contrary flat-junction device #1 already remained unchanged when turning on the illumination under short circuit conditions and therefore it was possible to separately analyze the changes in photo-potential under open circuit conditions (Figure 63/64).

4.3.3 Thin Mesoporous Perovskite Solar Cell

For the thin mesoporous device structure under illuminated open circuit conditions, the CPD developed across the compact TiO_2/mesoporous TiO_2 and across the perovskite/Spiro-OMeTAD interface (Figure 68a red/blue line profile). The bulk of the perovskite stayed field free, while the CPD increased towards the corresponding floating electrode with a final photo-potential matching the open circuit voltage (white arrows $\Delta CPD \approx 1$ V).

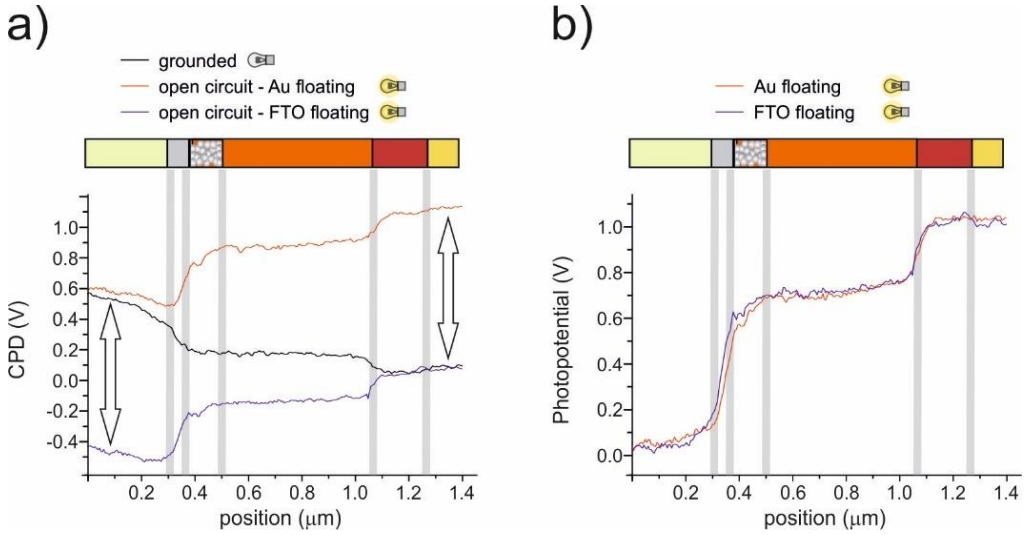

Figure 68: (a) CPD profiles for the thin mesoporous device structure under illuminated open circuit conditions (red/blue line profiles) compared with the initial dark conditions (black line profile). The CPD develops across the TiO_2 compact/mesoporous interface as well as the Spiro interface, while the perovskite bulk stays field free. (b) In the corresponding photo-potential for both options it can be observed that a significant higher portion of potential develops across the TiO_2 (~0.7 V) compared with the perovskite/Spiro interface (~0.3 V).

Hereby, the photo-potential which developed across the TiO_2 interface with ΔCPD ≈ 700 mV was higher than the potential which developed across the perovskite/Spiro interface with ΔCPD ≈ 300 mV (Figure 68b). Similar to flat-junction device #2, the time-dependent analysis under open circuit conditions could not be separately analyzed from the process under short circuit conditions (discussed in 4.3.2 last section).

4.3.4 Discussion

The CPD distribution of the thick mesoporous device structure differed from the distribution of the planar and the thin mesoporous devices. For the thick mesoporous device, the open circuit potential developed across the whole perovskite capping layer, while for the other devices it developed across both selective interfaces. An open circuit potential developing across the selective interfaces is connected with a charge arrangement at the interfaces and a corresponding field free perovskite bulk (similar to short circuit conditions). A comparison between the ΔCPD across the selective interfaces for the different device structures showed that the CPD across the TiO_2/perovskite interface was systematically higher than the CPD across the perovskite/Spiro-OMeTAD interface (Table 1). The reason for finding different energy levels for comparable devices, which were produced from materials with the same chemical composition, was expected to come from the doping density of the perovskite, as well as the preparation/doping of the selective contacts (see energy

diagrams in Figure 27/31).[92] For the perovskite MAPI it has already been reported, that the stoichiometry and thereby the density of the vacancies defines the doping level within the material.[89, 90, 128] Hence, the respective fermi energy levels of the layers could shift and different CPD distributions could be observed. Cai et al. reported that the ratio in CPD drops can directly be connected with the type of doping of the perovskite layer.[112] By using different precursor solutions of PbI_2:MAI, Cai et al. could show that the ratio of CPD drops at the interfaces under open circuit conditions changes with the stoichiometry of the perovskite precursor solution. An excess amount of PbI_2 thereby represents an n-type doping and results in a higher CPD drop at the MAPI/Spiro interface, whereas excess MAI leads to a p-type doping layer with a higher CPD drop at the TiO_2/MAPI interface.[89, 90] According to this, flat-junction device #1 exhibited a slightly higher MAI rich perovskite layer compared to flat-junction device #2. The thin mesoporous device layer therefore was also expected to exhibit a slightly higher FAI/MAI concentration.

While flat-junction device #1 did not show any charge accumulation under short circuit conditions at all, it still showed two dynamic process of re-arranging charges under open circuit conditions. Besides the fast development of the V_{OC} on the electrodes, a second slow process was observed, which could be identified as a re-distribution of charges in front of the selective contacts. The time constant of this slower process was in the range of a few seconds. Similar values had been reported in literature connected with the hysteresis[41, 42, 108] and could be attributed to the re-arrangement of ions.[108]

Sample	ΔCPD TiO_2/MAPI	ΔCPD MAPI/Spiro
Thick mesop.	Not available	Not available
Flat-junct. #1	600 mV	200 mV
Flat-junct. #2	500 mV	400 mV
Thin mesop.	700 mV	300 mV

Table 1: Comparison of the CPD drops (ΔCPD) between the interfaces TiO_2/perovskite MAPI and perovskite MAPI/Spiro for the different devices. While the thick mesoporous device showed a monotonous decrease in CPD across the perovskite layer, all other devices showed a higher CPD drop at the TiO_2/perovskite interface. Flat-junction device #2 shows the smallest difference between both interfaces, while it is also the device with the lowest efficiency.

When comparing the dynamics between both halves of flat-junction device #1, a slightly slower process had been observed for the TiO_2 side. Furthermore, a comparison of the CPD drops under open circuit conditions between both selective contacts showed a systematically higher value at the TiO_2 side for all cells. Assuming that the accumulation of holes inside the perovskite layer is caused by an unbalance of interfacial recombination, the recombination of electrons is taking place at the HTL side (Figure 56). Therefore, the density of holes is increasing from the HTL side towards the TiO_2 side over time. Further, the impact on the second slower process is affected similarly. This is in agreement with the observation that the dynamics at the TiO_2 side are slightly slower, compared to the HTL side.

4.4. External Bias/Preconditioning

In the previous chapters KPFM measurements for the two limits of operating conditions, namely short circuit- and open circuit conditions have been analyzed. In order to study CPD distributions for conditions in between these limits, which actually represent a state with a non-zero power output, it was necessary to connect an external load or representatively apply an external bias while illuminating. Furthermore, similar to the routine of recording an IV-curve, the external bias could be ramped or stepwise changed, in order to cover the full range between short- and open circuit conditions.

In the following section, CPD distributions under the influence of an external bias were studied. Subsequently, the experimental setup had been improved for the measurements of the different device architectures:

→ At the time when the measurements on the thick mesoporous device had been made, the possibility to apply an external bias was not included at all within the setup.

→ For the flat-junction device #1, CPD distributions for open circuit conditions and the correlated open circuit conditions with an external bias were compared.

→ For flat-junction device #2 a triangular bias ramp was applied while the CPD was measured. In order to separate the preconditioning effect of the applied bias and the photo generated charges, the experiments had been performed both with and without illumination.

→ For the thin mesoporous device structure, the setup was further optimized by applying a bias step-function. This step function had an advantage compared to the bias ramp, since the CPD within one scan line did not change and the time dependency could be studied within a bias step.

→ Furthermore, for the thin mesoporous device it was possible to measure the current while simultaneously measuring the CPD. With this additional information a direct correlation between the standard external measurement of an IV-scan and the internal CPD data could be studied. These simultaneous measurements made it possible to correlate local changes in the charge distribution with changes in the measured current signal.

4.4.1 Flat-Junction Devices

Device #1 - Comparison Open Circuit Conditions under Illumination/External Bias By adding a function generator (Teledyne LeCroy WaveStation 2052; 50 MHz waveform generator) to the experimental setup, it was possible to apply a bias ramp to one of the electrodes. The Ag electrode was connected to the plus pole of the generator, while the other electrode was set to the same ground potential as the KPFM feedback together with the minus pole of the generator (this was necessary for the feedback loop of the KPFM measurement).

Under illuminated open circuit conditions (previous chapter), the floating electrode charged up until the CPD reached a saturated state. When applying an external bias in the electric circuit of the same magnitude as the open circuit voltage, the same scenario was expected. Within the error of the measurement, the CPD line profiles for the scenarios of open-circuit conditions and external bias light off/on overlapped and showed the same trend (Figure 69).

Notice: Since the KPFM scan was performed while applying a triangular bias ramp (20 mV/s; 0 V → 1.1 V→ 0 V), the bias changed within each line profile by 9 mV from left to right and thereby produced a systematical error. This error was calculated by taking into account, that the scan rate was 1 Hz, which means that 1 cycle of forward/backward KPFM scan took 1 s. Since at both ends, an "overscan" of 5% was included to care for the piezo imprecision of the xy-scanner at the turning points, the recorded line profile of the backward scan took exactly 0.45 s and thereby experienced 45 % of the 20 mV change during one scan cycle (err = 9 mV). Since the cantilever position was oriented above the Ag side and the backward scan profile was analyzed, the applied bias accordingly changed by +9 mV from left to right in the line profile. Further comparisons of the forward and the backward direction of the triangular bias ramp did not reveal significant changes within the systematic error of the measurement (> 18 mV) and is shown in the appendix-5.

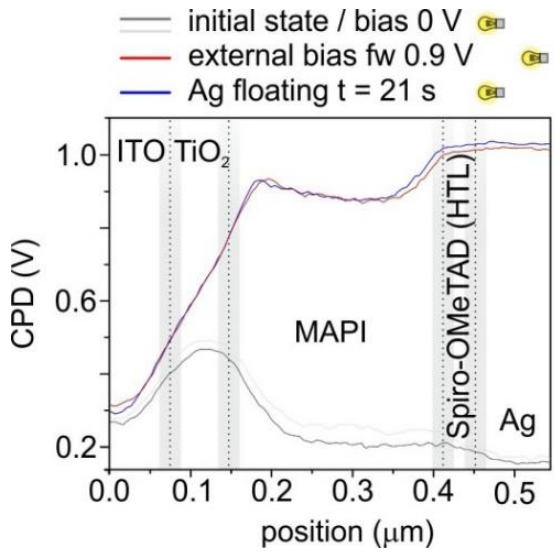

Figure 69: CPD profiles representing the case of an externally applied bias (red curve) and open circuit conditions under illumination (blue curve). Both profiles overlap within the error of the measurement.

Device #2 - External Bias Ramp with Light Off A triangular bias ramp was applied to the Ag electrode with the light turned off (0 V → 1.1 V upward ramp; 1.1 V→ 0 V downward ramp). When comparing the CPD profile of the upward ramp for the same applied external potential as the downward ramp, the profiles matched on the electrodes but not in between (Figure 70a compare red and blue line profiles). Even though the previously mentioned systematic error, connected with the bias ramp change within one scan line, must be considered (2 times 9 mV for comparing upward and downward ramp profiles), the actual difference in the line profiles between upward and downward direction was still significantly bigger with ΔCPD of up to 100 mV inside the perovskite MAPI. Since the ΔCPD, was significantly bigger than the systematic error (~ 5 times) the charge density distribution calculated from these offsets was suggested to qualitatively represent the changes for the bias ramp preconditioning (Figure 70b). During the bias induced preconditioning, positive charges accumulated in front of the TiO_2 while negative charges arranged inside the perovskite MAPI and again positive charges in front of the Spiro-OMeTAD. At the electrode interfaces negative charges were observed, which screened the positive charges in the device towards the electrodes.

Within the perovskite MAPI, the total sum of charge density distribution resulted in a positive value of additional charges. An exclusive redistribution of ions however would have resulted in an equal amount of positive and negative charge densities inside the perovskite MAPI (the total sum must thereby stay zero).

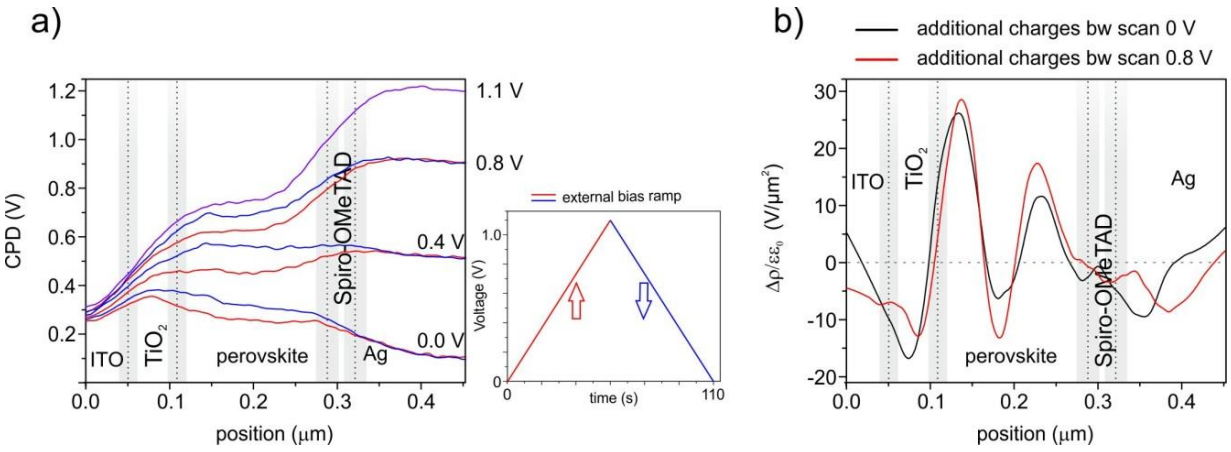

Figure 70: CPD profiles measured under an external triangular bias ramp applied to the Ag electrode without additional illumination. After each step of 0.4 V the CPD profile is plotted for both forward and backward ramp direction. The downward ramp has an offset in CPD inside the perovskite compared to the upward ramp. (b) In the respective additional charge density between the upward and downward ramp at 0 V and 0.8 V an accumulation of positive charges are observed in front of the TiO_2 and the Spiro-OMeTAD, while negative charges are present within the perovskite and on the electrodes.

The observation of an overall positive charged density lead to the suggestion that additional carriers such as trapped injected holes must have been stored within the device during the bias preconditioning. Without any illumination and thereby any additional photo-generated charges present, these holes could have only been injected into the perovskite MAPI with the external bias exceeding the corresponding potential barrier at the selective interface. These injected charges were then suggested to be trapped inside the device, while they remained in the perovskite during the downward scan.

External Bias Ramp - Light On In the next step, the same setting of the bias ramp on the CPD distribution was analyzed with illumination turned on. By adding the illumination in the experiment, the device was studied under the exact working condition as for an IV efficiency measurement. In order to separate the accumulation of charges under short circuit conditions and the additional bias ramp, the experiment was performed in two steps. Firs the light was switched on and some time passed for the photo-generated charge accumulation to saturate under short circuit conditions (~12 s) and second the triangular bias ramp was started and the CPD profiles were recorded (Figure 71a). Under the influence of the external bias, the CPD increased on the electrodes, as well as within the perovskite bulk. However, while the increase and decrease of the applied bias could directly be measured on the electrode, the CPD within the perovskite showed two different decrease processes for the downward ramp scan. First the CPD steadily decreased to the level, which was also measured at 0.8 V for the upward ramp scan. After that, the CPD within the perovskite stayed on exactly that level while the external bias on the electrode further decreased to zero. When calculating the additional charges which were present after a complete bias ramp compared to the start at 0 V, positive charges could be observed in front of both selective interfaces (Figure 71b), while negative charges screened the electric field towards both electrodes.

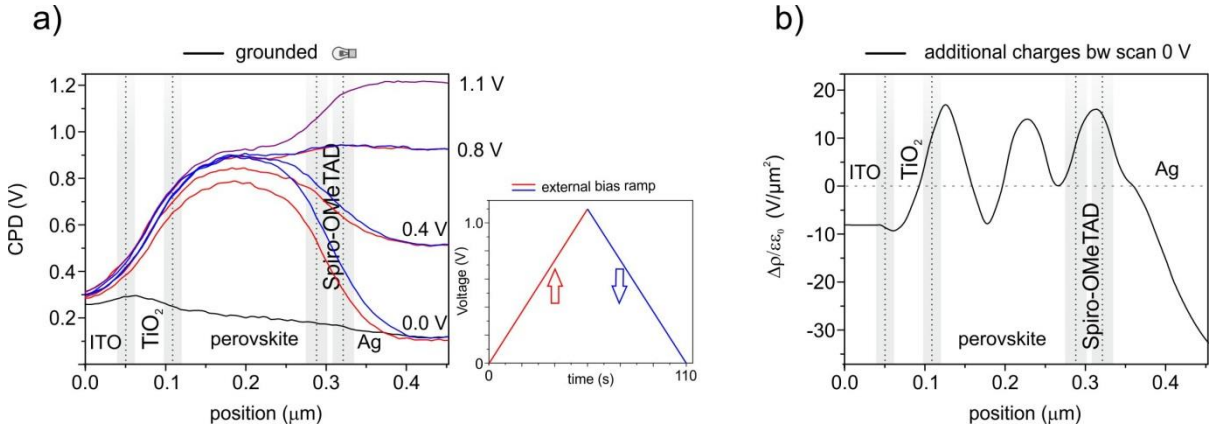

Figure 71: (a) CPD profiles for an external bias ramp applied to the Ag electrode under illumination. Each step of 0.4 V is plotted for the upward and the downward ramp scan. While the CPD overall increases for the upward ramp scan (except for the grounded ITO electrode), during the downward ramp scan the CPD within the perovskite bulk stops and stays on the level under the external bias of 0.8 V. (b) For the additional charge density calculation after a complete bias ramp, stored positive charges are present in front of the selective interfaces. The additional peak on the Spiro-OMeTAD is expected to arise as an artifact during the calculation (smoothening/derivative) of the charge density.

The changes in the CPD, which developed under the complete cycle of the applied bias ramp (Figure 71a at 0 V), were further compared with the changes in CPD, which developed under illuminated short circuit conditions (Figure 44). While the offset in CPD compared to equilibrium within the perovskite MAPI after the applied bias ramp was 0.7 V, the respective offset for saturated short circuit conditions under illumination was only 0.5 V. Additional injected charges, which accumulated in the perovskite MAPI were thereby effectively stored during the bias ramp. The light and with it the additional photo-generated charges inside the MAPI enabled a more effective preserved CPD inside the mesoporous with a higher offset ΔCPD compared to that in dark conditions. In dark conditions the decrease in ΔCPD did not saturate during downward ramp. While the bias steadily decreased, the additional charges at the interfaces either recombined or were extracted even below a bias of 0.8 V. Assuming that the amount of accumulated charges define the level of the preconditioning state, a direct connection with the JV characteristics can be suggested. A more pronounced accumulation of charges at the interfaces under illumination and external bias matches with the general observation of effectively bigger hysteresis in the JV characteristics, compared with an applied external bias without additional illumination.

4.4.2 Thin Mesoporous Perovskite Solar Cells

While the previous measurements with an external bias on the flat junction devices were performed with a waveform generator, the setup for the measurements on the thin mesoporous device structures was upgraded with a source meter (Keithley 2450). With this source meter it was possible to apply a bias while at the same time measure the current through the device. Therefore, not only cross-sectional CPD data could be collected, but also the generated photocurrent data. Hence, the external observations generally made for efficiency measurements (JV-scan) could directly be correlated with the internal CPD distribution. The source meter was synchronized with the AFM software and any sequence of bias could directly be applied to the device with simultaneously measuring the current (the implementation into the software was done by a summer student Niklas Tausendpfund from the physics department).

As a first experiment, the impact of a negative bias on the charge distribution was analyzed. Without illumination and therefore no current flowing, any redistribution of charges within the perovskite layer could thereby solely be connected with the preconditioning of the applied bias. A re-arrangement of positive charges in front of the compact TiO_2 layer has already been observed under short-circuit conditions (Figure 49). Furthermore, the same re-arrangement has been observed for the flat-junction device under the influence of an external bias (Figure 70). Consequently, by applying a negative bias, the opposite arrangement of charges was expected. With the electric field at the interface being reversed, this time negative charges were expected to accumulate in front of the TiO_2 interface.

External Bias: CPD for Reverse Direction A bias of V = -0.5 V was applied to the Au electrode to create reverse bias condition. Respective line profiles of the CPD distribution for the equilibrium state, for saturation under the reverse bias and for the grounded condition after returning from the reverse bias to 0 V were compared and analyzed (Figure 72a). Hereby, the CPD distribution after applying the reverse bias was of special interest. A negative offset compared to the equilibrium was observed, starting at the compact TiO_2 all the way across the FTO with a maximum difference in CPD of ~150 mV (Figure 72a – blue line profile). As expected, excess negative charges arranged across the mesoporous-compact TiO_2 layers (Figure 72b – red line profile). After returning to zero bias, these negative charges disappeared and positive charges inside the mesoporous TiO_2 became visible Figure 72b – blue line profile).

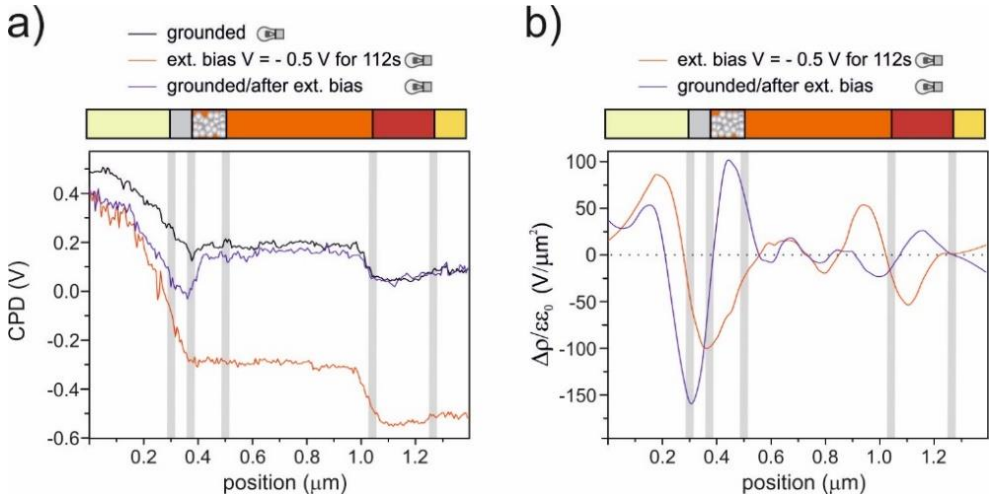

Figure 72: (a) CPD distribution for an external applied bias in reverse direction (-0.5 V). The black line profile shows the initial state, while the red line profile shows the saturated CPD for the reverse bias after 112 s. After turning off the external bias, the CPD returns to the initial level for the mesoporous TiO_2 towards the Au electrode, however a negative offset is detected across the mesoporous/compact TiO_2 interface up to the FTO electrode. While the FTO electrode is grounded, the CPD is expected to stay on the same level. However, a negative offset can be observed, which might arise from the sheet resistance of the FTO. (b) The charge density distribution for the corresponding excess charges reveals that negative charges accumulate at the mesoporous/compact TiO_2 interface during the time of the externally applied reverse bias. Directly after the preconditioning, these negative charges disappear and positive charge carriers within the center of the mesoporous TiO_2 become visible.

A similar effect has already been observed under short circuit conditions, where negative charges within the mesoporous layer disappeared as soon as the light was turned off, unraveling remaining longer living positive charges, most probably ions (Figure 53).

External Bias: IV-CPD Data at Maximum Power-Point Next, the CPD and the corresponding current data was recorded at the maximum power-point (V_{ext} = 0.75 V). For the CPD measurements, a time dependent increase of ~90 mV was observed in a time interval of Δt = 69 s starting in the FTO layer all the way to the perovskite/HTL interface (Figure 73a). By calculating the respective time-dependent increase of the integrated area between the equilibrium CPD profile and each CPD profile measured under the external bias, the data could be fitted with a double exponential decay fit. Thereby, a "slow" time constant of $\tau = 24.7 \pm 7.6$ s was calculated (Figure 73b). Since the current was measured simultaneously, the corresponding double exponential decay fit for the increase in current could be fitted as well, resulting in a "slow" time constant of $\tau = 17.7 \pm 0.3$ s (Figure 73c). Even though the time constants differ by 7 s, they still match within their errors. The determination of the time constant from the integrated CPD profiles was thereby less accurate. Still the tendency is that the measured changes in CPD distribution is directly connected to the current output and thereby the hysteresis in JV-scans.

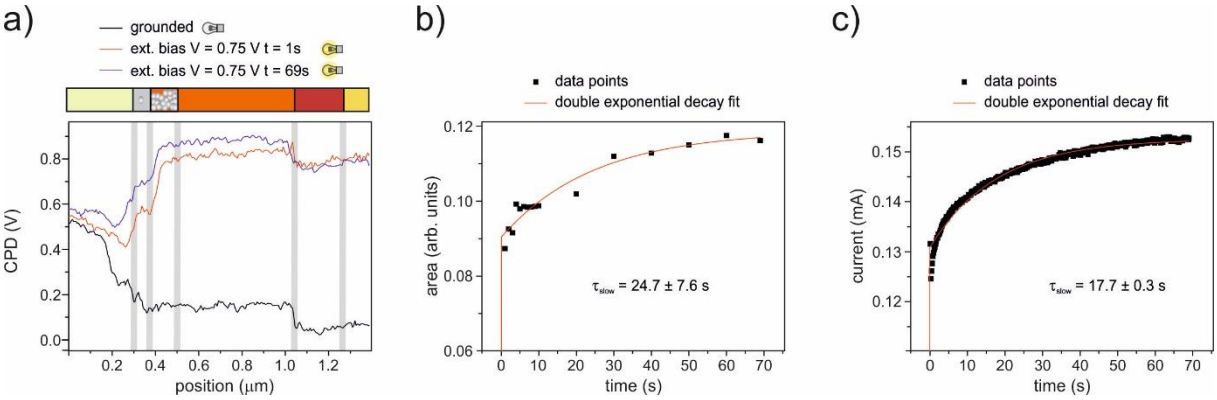

Figure 73: (a) CPD distribution for an external applied bias at maximum power point conditions. The black line profile represents the initial state, while the red line profile is recorded after 1 s of an external applied bias at V = 0.75 and the blue line profile after 69 s. Compared with the red line profile, the blue line profile shows an increase in CPD of about 100 mV starting in front of the TiO_2 all across towards the perovskite/Spiro interface. (b) The data of the integrated area between the CPD profiles under bias and the initial state are plotted and fitted with a double exponential decay fit. While the first time constant cannot be resolved with the resolution of the measurement, the slower time constant is τ = 24.7 ± 7.6 s. (c) The corresponding change in the current is plotted and fitted with a double exponential decay fit (please note that the sign of the measured current is changed due to convention). The slower time constant of the fit gives τ = 17.7 ± 0.3 s, which is comparable to the calculated time constant of the CPD increase.

External Bias: IV-CPD Step-Function The experiment was performed with external bias steps of 0.2 V, each for a time interval of 13 s, starting at -0.2 V up to 1.2 V and back to -0.2 V again (Figure 74a). Comparing the CPD profiles for the upward bias steps and the downward bias steps at each start of the interval, an offset of up to 200 mV in the mesoporous TiO_2 layer was measured (compare red/blue profile at 0 V). The offset in CPD spread over the entire perovskite and compact TiO_2 layer, while the magnitude decreased steadily in time (CPD over time within one bias step – not shown). This offset in CPD when comparing upward and downward bias direction has also been observed for the flat-junction devices, which indicated additional positive charges in front of the compact TiO_2 (compare Figure 70b). For the corresponding current output, it was observed, that at each bias step the current saturated towards the steady state current (Figure 74b). While for the upward bias direction the current increased, in backward direction the current decreased at each step towards the corresponding steady state. Hence, the curve showed a standard hysteresis, rather than an inverted hysteresis which had been measured before the cross-section preparation of the device.

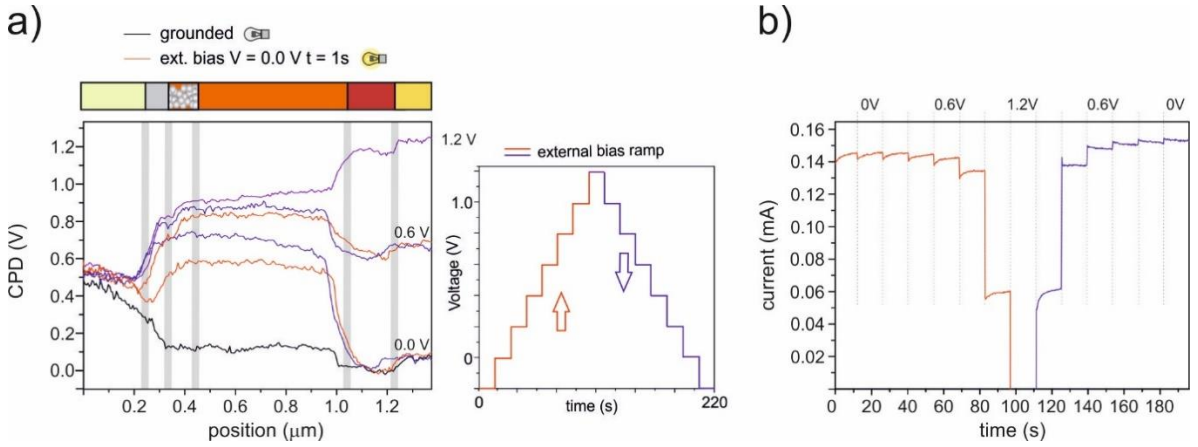

Figure 74: (a) CPD distribution under the influence of an externally applied bias step-function with representative profiles at 0 V, 0.6 V, 1.2 V and the same steps back to 0 V. The measurement was performed with step-sizes of 0.2 V, each for 13 s, starting at -0.2 V up to +1.2 V and back again. The black line profile is the reference profile under equilibrium conditions, while the others are measured under illumination. By comparing the forward direction with the backward direction, an offset in CPD is observed with a maximum of ~200 mV at 0 V inside the mesoporous TiO_2, decreasing steadily towards the FTO on one side and the Spiro on the other side. (b) The corresponding current changes and saturates for each bias step versus time. While under forward direction, the current increases towards equilibrium, under backward direction the current decreases.

Both time constants of the processes were analyzed to correlate the time-dependency of the photo-current and the changes in the CPD distribution. The representative bias of 0.6 V was chosen since it showed the most prominent change in current for the whole dataset. While the single exponential decay fit of the data points for the integrated area between the CPD profiles resulted in a time constant of $\tau = 5.7 \pm 2.9$ s, the same fit routine gave a time constant of $\tau = 6.9 \pm 1.2$ s for the changes in the current curve at V = 0.6 V (Figure 75). The time constants overlapped within the error of the measurement and were supposed to be connected with the same process, hence the accumulation of mobile ions in front of the compact TiO_2 which influenced the charge extraction efficiency.

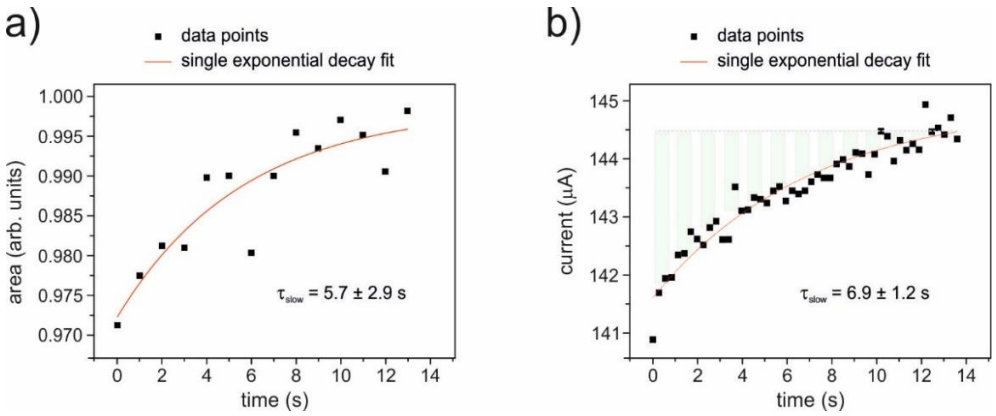

Figure 75: (a) The data points for the integrated area between the CPD profile under the influence of an external bias of 0.6 V at forward direction and the corresponding single exponential decay fit with a time constant of $\tau = 5.7 \pm 2.9$ s. (b) The corresponding data for the change in current is fitted with a single exponential decay fit, resulting in a time constant of $\tau = 6.9 \pm 1.2$ s.

Next, the amount of charges which accumulated inside the device (CPD measurement) and the additional charges, counted from the increase in current were analyzed. The hypothesis was that within time charges were stored at the perovskite MAPI/TiO_2 interface (or filled trap states) until saturation was reached. At the same time, the rest of the free charges, could be extracted. If this hypothesis was correct, the charges which were stored at the interfaces (change in CPD) and the virtual charges between the measured current curve and the saturated level of the current (accumulated charges from the hypothesis; Figure 75b – green area) would have been equal. Therefore, the changes in CPD for the bias step at 0.6 V upward direction inside the perovskite MAPI layer was calculated and derived two times to receive the charge density distribution (divided by epsilon) of the additional charges (see equation 28). In order to calculate the actual charge density, the permittivity of $\varepsilon = 62 \cdot \varepsilon_0$ was used, which had been determined by Anusca et al. combining Raman and ultrasonic spectroscopy with dielectric analysis.[129] When integrating the absolute charge density over the perovskite layer of the whole cell (0.7 µm x 0.8 cm x 0.3 cm) and dividing it by two, the total number of stored electrons (or holes) was calculated:

$$Q_{CPD} = \frac{1}{2} 62 \cdot \varepsilon_0 \cdot \iiint \left| \nabla^2 \phi_{sample} \right| dx\, dy\, dz = 313\ (\pm 53)\ nC \qquad (32)$$

For this calculation I assumed that that all of the charge density came from either electrons or holes and both charge species were equally present within the perovskite layer. The error was calculated, by taking into account that the resolution of the FM-KPFM measurement was < 50 nm.

When integrating over the area between the saturated current level and the fitted current a total number of:

$$Q_I = \int (I(t) - I(t_{sat}))dt = 13.5\ (\pm 1.5)\ \mu C \qquad (33)$$

was calculated. The error was calculated by calculating the area from the actual data points instead of the fit and taking the difference compared to the area from the fit.

Hence, the amount of charges, which could have possibly been stored at the interface, was forty times lower than the amount of charges, which would have been extracted if the output current was constantly having the magnitude of the saturated level.

4.4.3 Discussion

Under the influence of an external bias, applied to one of the electrodes, charge re-distribution occurred similarly as under illuminated open circuit conditions. When the applied external bias exceeded the open circuit voltage, additional charges were injected into the perovskite (Figure 70), which also accumulated at the interfaces. In case of an applied bias ramp (as performed during an IV-scan), additional charges were also observed at the interfaces of the perovskite which could not simply come from a re-arrangement of ions. I thereby concluded that the changes in CPD within the perovskite layer from preconditioning with an external bias were caused by a combination of a redistribution of ions and stored/trapped charges at the interface. A redistribution of mobile ions was expected to appear due to the electric field caused by the external bias. The analysis of operating conditions could thereby successfully be completed by studying both open circuit conditions and the influence of an external bias. With the integration of a source meter into the setup, the correlation of the local redistribution of charges and the external current output signal could be made.

The comparison of the time dependency between the current output and the corresponding changes in CPD lead to similar time constants. Furthermore, these time constants are matching with values for the time dependency of hysteresis reported from literature.[41]

For the combined KPFM-current measurement on the thin mesoporous device structure, the analysis of the current data revealed standard hysteresis and not the inverted hysteresis which had been observed in the initial JV-curve of the untreated device (Figure 35). In this case it must be noted that the measurement procedure of the initial JV-setup unavoidably involved intense light soaking for several tens of seconds prior to the start of the JV-scan of the unprocessed device. The light soaking seemed to cause a preconditioning which can provoke the inverted hysteresis, which was confirmed in discussions with my cooperation partner Wolfgang Tress. As observed in the previous section for illuminated short circuit conditions, the light soaking lead to an accumulation of positive charge carriers into the mesoporous device. The resulting effect on the band bending at the electron selective interface could thereby create optimum conditions for the charge transfer.[130] Any further changes under the influence of an external bias above the open circuit voltage then again could lead to a decline in current with a decrease of charge transfer at the interface. Hence, intense light soaking would have a long-lasting negative effect on the charge transfer at the electron selective interface.

An influence of the charge transfer with charge accumulation at the interface could be concluded from the comparison of the CPD data and the current output at a certain bias step. The amount of charges which were actually stored at the interface, were compared with the amount of charges calculated from the difference between the actual current and the stabilized current over time (Figure 75b green marked area). Since the amount of charges differed by a factor of forty, it could be concluded that the hysteresis in current output could not solely come from capacitive charges which were stored and released. Actually, accumulating charges and rearranged ions cause a change of the efficiency in charge extraction (and recombination) by altering the band bending at the selective interface (see also Figure 55).[130, 131] The band bending at the interface leads to a reduced or increased barrier for charges to overcome when transferring towards the respective selected layer.
I could thereby show that the changes in CPD under preconditioning conditions, which are observed at the interfaces, were caused by a combined accumulation of electronic and ionic species, which thereby directly influence the efficiency in charge transfer towards the electrode and hence the current output.

4.5. Comparing FM- with AM-Measurements

In the fundamentals section, two fundamental methods of performing a KPFM measurement were described, namely the amplitude modulation (AM) and the frequency modulation (FM) method. Both methods have in common, that an AC voltage is applied to the tip (or the sample) and due to the CPD of the tip-sample system and the corresponding electrostatic force, the tip starts to oscillate at the related frequency (and/or heterodyne frequencies of mechanical and electrical excitation).

In the AM-method, the feedback mechanism is sensitive to the electrostatic force directly. The long reaching electrostatic interaction, thereby not only leads to contributions of the CPD between surface and the tip cone of the cantilever, but also between the surface and the rest of the tip as well as the complete cantilever arm (Figure 16a).[57, 58] Hence, a proportionate averaging effect (CPD crosstalk) for the detection of the CPD and hence quantitatively incorrect values are expected to occur for AM-KPFM related methods.[57, 58, 61] Variations of AM-KPFM techniques can be achieved by setting the electrical excitation frequency (AC voltage) to the first or second eigenmode, or off resonance.[132, 133] The specific cantilever orientation was mentioned to influence the detection of the CPD as well.[134]

FM-KPFM on the contrary is sensitive to the electrostatic force gradient and thereby is much less prone to this kind of crosstalk (Figure 16b).[57, 58, 61] Variations of FM-KPFM can be achieved by sideband modulation FM- or heterodyne KPFM,[135] and for vacuum conditions also with a phase locked loop on the frequency shift. While the theory behind sideband modulation has already been explained in the fundamentals section, for heterodyne KPFM the excitation frequencies are chosen in order for a sideband to appear on one of the eigenmodes, while the mechanical excitation accordingly set on the other eigenmode and therefore increase the signal to noise ratio.[135]

Even though the problem of using AM-KPFM to measure samples with lateral differences in work function on a nanometer scale is known from literature, recently several studies have been published reporting on cross-sectional KPFM studies by using the amplitude modulation method.[79, 103-105, 136, 137]

In order to directly address the key benefits of using FM-KPFM for cross-sectional measurements, the results for both methods were directly compared for the thick mesoporous device architecture. AM-KPFM was thereby performed with the

electrical excitation frequency set on the first eigenmode ($V_{AC} = 1\ V$) in dual pass (lift height $h = 0\ nm$).

First, measurements under short circuit conditions were compared (Figure 76). In the FM measurements at dark conditions, a monotonously decreasing CPD from the FTO electrode CPD_{FTO} = 0.6 V towards the Au electrode CPD_{Au} = 0.0 V was observed (Figure 76a – black line profile). As already discussed in (4.1.1), the difference in surface potential between both electrodes ΔCPD ≈ 0.6 V matched with the difference of their respective work function literature values.
In comparison the corresponding AM measurement (Figure 76b – black line profile) revealed a monotonously decreasing potential as well, however with different absolute values on the FTO electrode CPD_{FTO} = 1.25 V and the Au electrode CPD_{Au} = 1.03 V. While the CPD on the FTO electrode turned out to be 0.65 V higher in the AM measurement, the CPD on the Au electrode showed an even higher offset of approximately 1 V. The CPD crosstalk in the AM measurement thereby resulted in a positive offset compared to the FM measurement and a reduced difference between both electrodes ΔCPD ≈ 0.22 V. This difference in CPD was suggested to be caused by the CPD crosstalk with the glass substrate underneath the cantilever. Since the cantilever arm was positioned above the glass while measuring the CPD on the FTO electrode, a contribution of the glass substrate coupled into the feedback. The glass thereby gave an upward shift on the CPD measurement since it had previously been contaminated with implanted Ga^+ ions from the FIB polishing process. This averaging "stray field" effect resulted in a shift in CPD of ~0.65 V on the FTO electrode. The same effect occurred when the CPD of the Au electrode was measured. However, as the FM measurement could locally follow the CPD over the layer structure to the Au layer with minimized crosstalk, the offset between the FM and the AM measurement for the Au electrode was even higher with approximately ~1V. The absolute difference between the FTO and the Au electrodes for the AM measurement was thereby measured to be only ΔCPD = 200 mV, which was 400 mV less than for the FM measurement.

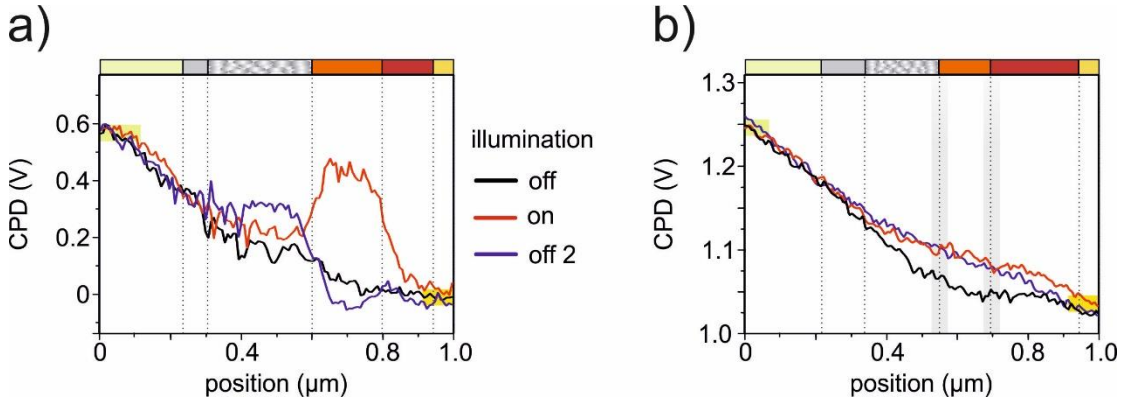

Figure 76: (a) CPD line profiles for cross sectional frequency modulation KPFM (FM-KPFM) measurements of a mesoscopic perovskite solar cell under short circuit conditions. (b) Corresponding CPD line profiles for amplitude modulation KPFM (AM-KPFM).

When illuminating the device and measuring FM-KPFM, a pronounced peak in CPD of ~200 mV was observed within the perovskite capping layer and a small offset of around ~50 mV in the mesoporous layer (Figure 76a – red line profile). For the same scenario in the AM measurement however, only a slight increase in CPD on the layers in between the electrodes with a maximum height of ~50 mV was observed (Figure 76b – red line profile). Thereby, the general tendency of an increase in CPD was consistent with the data observed by FM-KPFM. However, no locally distinct peak could be confined to the perovskite capping layer. In contrast, only a flat offset in CPD starting next to the compact/mesoporous TiO_2 interface and reaching into the Au electrode was observed. Again, the lateral resolution was limited by the strong averaging effect of the AM-KPFM crosstalk.
The same phenomenon has been observed when the illumination was turned off. While in the FM measurements a remaining positive offset in the mesoporous layer structure was observed (compare Figure 76a – blue profile), in the AM data no significant difference to the illuminated case was located (unless that the CPD returned to the initial equilibrium CPD on the Au electrode). Summing up, in the AM-KPFM measurement the averaging effect of the CPD crosstalk hindered an analysis of the quantitative CPD values, while local CPD differences (e.g. upon illumination) could not be confined to exact layers within the device structure.

Under open circuit conditions, the crosstalk in AM-KPFM measurements became even more prominent. While in both cases of floating electrodes for FM-KPFM the CPD increased about ±0.8 V compared to the dark case (Figure 77a – white arrows), for the AM-measurements significant differences for a floating FTO and floating Au electrode were observed. When the FTO electrode was set floating, a change of -0.8 V in CPD was measured upon illumination (Figure 77b – white arrow), in agreement with the FM measurement.

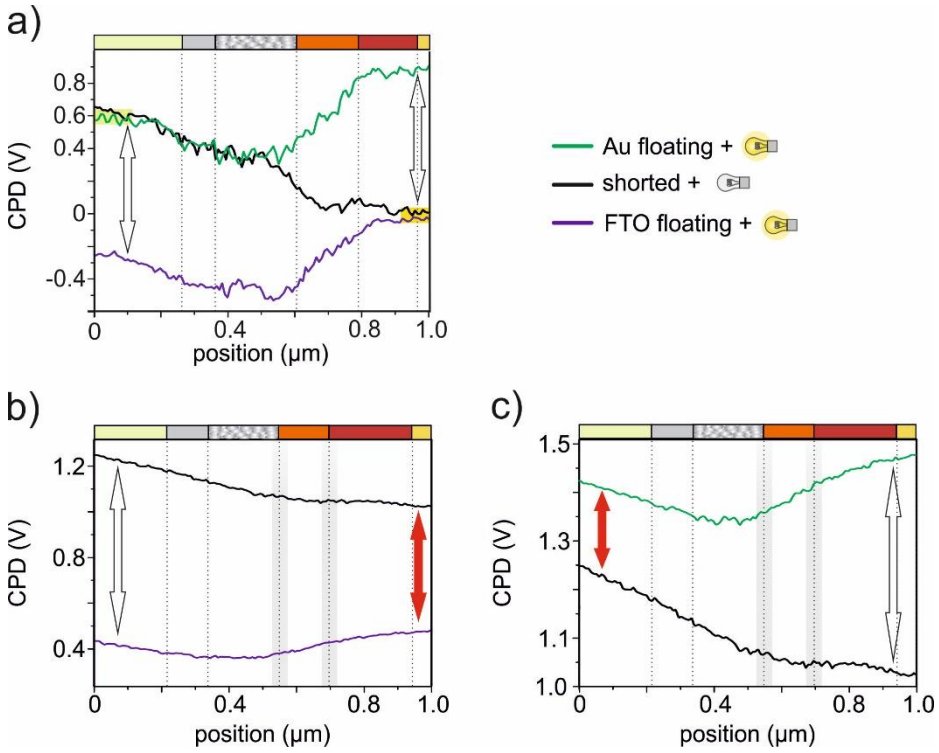

Figure 77: (a) CPD line profiles for frequency modulation KPFM (AM-KPFM) measurements under open circuit conditions. (b) and (c); corresponding AM-KPFM measurements.

However, on the grounded electrode a decrease in CPD of > 0.5 V (red arrow) was measured as well. The change in CPD on the grounded electrode was a direct result of the CPD crosstalk and has also been measured by Ziegler et al. in a similar experiment[61].

After the floating conditions were switched, upon illumination an increase in CPD of 500 mV was measured for the floating Au (Figure 77c – white arrow) and an increase of 200 mV was measured on the grounded FTO electrode (red arrow). The measured values on the respective electrode therefore significantly differed between the two open circuit conditions. These asymmetric changes in CPD were caused by the different geometric orientation of the cantilever with the respective area underneath the cantilever, when detecting the CPD underneath the tip apex. This effect has also been observed and studied by Charrier et al..[134]

When the tip apex was positioned above the grounded Au electrode in the floating FTO electrode scenario, the whole cantilever experienced electrostatic interaction with the system underneath and thereby the charged FTO electrode, which resulted in a crosstalk of > 0.5 V.

For the scenario when the Au electrode was set floating and the tip apex was positioned above the FTO electrode, the cantilever crosstalk mainly coupled with the interaction signal from the glass substrate and thereby was not influenced in the

same way by the charged electrode. Therefore, the CPD crosstalk was less for the second scenario of a floating Au electrode with a magnitude of 0.2 V (0.3 V less than for the floating FTO scenario).

4.5.1 Discussion

Differences in CPD on small scales of less than at least 1 µm cannot be quantified with the AM-KPFM (using the first resonance electrical excitation in dual pass) technique due to the averaging over the CPD due to electrostatic cantilever crosstalk. The averaging effect did not only lead to false quantitative CPD values, but also to false qualitative differences in CPD. The consequence is that whenever heterogeneous structures on small scales are studied by means of KPFM, the frequency modulation method must be used in order to be able to qualitatively and quantitatively analyze these structures.

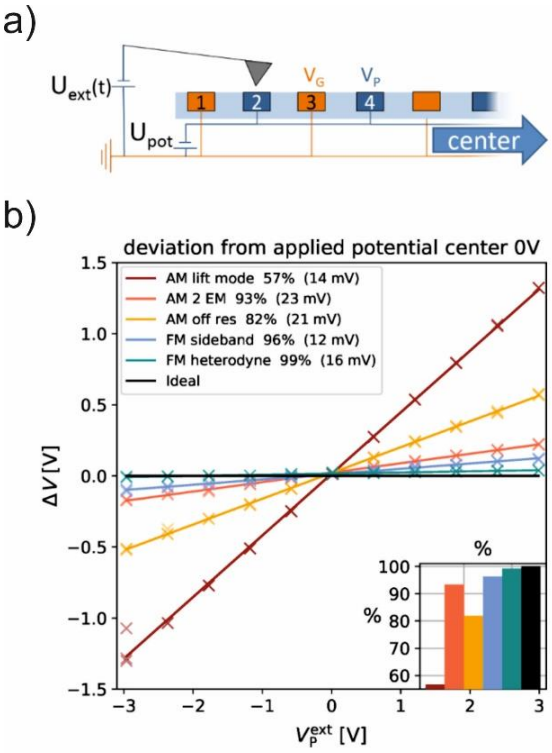

Figure 78: (a) KPFM measurement on the interdigitated electrode array, with alternatingly having one electrode grounded, while on the other electrode a voltage U_{pot} is applied. (b) When applying the voltage to the electrode each KPFM method has a different deviation (ΔV) from the actual applied voltage V_P^{ext}, which scales linearly with the magnitude of the applied voltage. "Adapted with permission from (Beilstein J. Nanotechnol. 2018, 9, 1809–1819.). Copyright (2018) Beilstein-Institut."

On the basis of my initial measurements, my colleague Amelie Axt published her systematic studies comparing different methods of measuring KPFM on a reference interdigitated electrode array (Figure 78).[133] The electrode structure thereby had alternating grounded and biased electrodes in equal length steps of 2 µm. For the two KPFM techniques, which were also used for my measurements namely sideband modulation and AM in lift mode, 96 % (FM sideband) and 57 % (AM lift mode with lift height 10 nm) of the full potential difference could be captured. These results are in agreement with the results from my measurement and correspond to the measurement of the open circuit voltage, which builds up between the electrodes (Figure 77). It was also observed, that the AM lift mode measurement gave different ΔCPD values between the Au and the FTO floating (Figure 77b/c). This phenomenon could also be replicated with the reference measurements from Axt et al..[133] Hereby, the measurement was performed with the tip

placed above the first electrode couple, while the rest of the cantilever was oriented above the glass substrate. In comparison to the first measurement, where the cantilever was oriented above the rest of the electrode array, the AM lift mode accuracy increased to capturing 68 % of the full potential. Under the same conditions the FM sideband measurements stayed on almost the same percentage with 97 %. An additional experiment, where a defined stray field was applied underneath the cantilever lead to the same results. Therefore, this reference study could confirm the argumentation of cantilever crosstalk on the cross-section devices and the necessity of choosing a FM-KPFM technique for such measurements.

5. Conclusion

"I... a universe of atoms, an atom in the universe."

— Richard Feynman

With cross-sectional KPFM, real-space information about time-dependent electric processes under different working conditions in various perovskite solar cells could be studied on a nanometer scale. By studying the time-dependency of the processes with KPFM, I could distinguish between electric and ionic charge dynamics and localize these changes within the cell. With the combination of externally measuring the device's photo-current while simultaneously imaging the changes in the KPFM signal in time, a direct correlation of the time dependencies between the current output and KPFM measurements could be made. Hence, I could show that the processes observed via KPFM are the processes which alter the current output and thereby are the cause of the hysteresis.

With the CPD profiles of the layer structure, I could show that a p-i-n junction is formed inside a perovskite solar cell upon its fabrication. While the p- and the n-layers refer to the selective contacts, the -i- refers to the intrinsic perovskite layer. With the built-in potential of the selective contacts, the intrinsic layer exhibits an electric field. This electric field generates a force on the ionic species of the perovskite crystal structure. Depending on the activation energy for the mobilization of the ionic species within the respective layer (mesoporous, bulk perovskite) these ions/vacancies are able to migrate through the device, driven by the electric field. While negative ions/vacancies are directed towards the p interface, positive ions/vacancies are directed towards the n interface. In case of a MAPI based perovskite solar cell the respective ions (or vacancies counterparts) could be I^-, $CH_3NH_3^+$ and Pb^{2+}. For a resulting accumulation of mobile ions at the respective interfaces, the built-in electric field is screened and a field-free intrinsic layer is created. Accordingly, band bending appears at the selective contacts and thereby the charge extraction efficiency is affected.[130]

Besides the activation energy of the ion migration for the respective layers (e.g. in the thick mesoporous layer, the initial built-in electric field was not sufficient to provoke an ion migration), the exact field distribution with the magnitude of the drops in potential is further influenced by the stoichiometry of the ionic species. Variations can occur from unintentional doping caused by slight changes in the mixing of the precursor or the crystallization dynamics of the perovskite MAPI.[89]

Differences in the charge recombination dynamics at the selective interfaces can cause an accumulation of one charge species. With a higher electron recombination at the TiO_2 interface, compared to the hole recombination at the hole transport layer (HTL), positive charges accumulate inside the perovskite layer. This accumulation of charges creates an electric field, which again affect the ion migration. Hereby, the

resulting electric field can even reach a higher magnitude as the initial electric field of the p-i-n junction. Therefore, ions can start to migrate, which previously were not able to overcome the activation energy (e.g. a migration in or into to the mesoporous layer). This effect is also expected to be the underlying mechanism for a light soaking preconditioning.[122, 124] A preconditioning scenario thereby refers to a state which alters the charge extraction efficiency and thereby shows the same effect as for the IV-hysteresis.[44] Hence, when returning back to dark conditions, previously shifted ions and accumulated photo-charges also return back to their initial equilibrium state with a time constant in the order of seconds. Thereby, the charge extraction dynamics at the selective interfaces change within time and hysteresis can be observed for light soaking. Ion migration, caused by the electric field of accumulated charge, could thereby also explain why for some mesoporous device an inverse hysteresis is observed, only when exposed to a long-term light-soaking preconditioning.[45]

Similarly, open circuit conditions or an applied external bias, affect the migration of ions, when generating an electric field across the device. Furthermore, charges can be trapped/stored next to the interfaces when the applied external bias exceeds the dark current threshold.

With a direct correlation of the time dependent changes in photo-current and the changes in CPD during a step wise IV ramp, ion migration on a time scale of several seconds ($\tau \sim 6s$) could be identified as the underlying mechanism for the hysteresis. Further analysis of the direct correlation could also confirm that the hysteresis cannot be explained by assuming that solely an amount of accumulated capacitive charges at the interfaces is stored and released and therefore change the current after the preconditioning. In fact, the accumulation of charges plus the migrated ions lead to band bending and therefore a change in the charge extraction and recombination efficiency.

Recent time resolved KPFM data form our group suggest a fast ion migration below the ms regime (faster than the time resolution of my measurements).[138] A formation of localized interfacial charges in the ms regime was observed, which stayed stable for over 500 ms after the bias was switched off.

In total we could therefore identify at least three different processes on different time scales with the real-space time-dependent FM-KPFM measurements. Even though there's still a discussion about the exact activation energies of the different ionic species, I can give a suggestion about the correlation of the observed time-dependent processes corresponding to the general expected trend.[118]

The three processes are expected to be:

- a fast migration of I^- on a time scale of μs with a relaxation time in the ms range [109]
- interfacial charges which built up and decay on a time scale ~ms
- a slow migration of $CH_3NH_3^+$ ions on the order of seconds,[116] which thereby create the preconditioning state and further lead to the long-term fluctuations in the output power, such as the hysteresis

In case of the Pb^{2+} ions, it is expected that they cannot easily migrate across the perovskite lattice, whereas they still can become mobile after degradation of the cell.[117]

6. Outlook

"We are lucky to live in an age in which we are still making discoveries."
— Richard Feynman

A lot of different processes have been observed inside different perovskite solar cells that can lead to a certain response in the current output or even to different preconditioning states (e.g. self-doping, light-soaking, external bias, etc.). While external IV measurements sometimes lead to contradictory conclusions with a lack of information about cells that were supposed to give the same result, my work can help to categorize solar cells according to their response in their cross-sectional CPD distribution, but also their current output. Thereby, processes can be addressed correctly and a statistical study of different fabricated solar cells with their IV-characteristics can help to further understand how to control the processes during the fabrication. Moreover, my work helps to have an overview about the different preconditioning states and therefore sensitize to take care, when studying cells that previously might have been altered.

With more knowledge and control over the fabrication process the next step is to optimize the device performance with at the same time increasing the stability of the devices, which is the holy grail for the perovskite community. A guideline to achieve this long-term goal relies on the understanding of the exact device physics. As the hysteresis plays a major factor for the device performance it is necessary to further analyze the process and finally being able to control it. In this sense it might be possible to develop a method for the fabrication process which uses a surface treatment in order to control the hysteresis by "freezing" the device in a defined efficient state. Thereby, the optimum device performance could be stabilized.

Stability, however, on the long term is the second big challenge, which must be mastered. Since the lifetime for efficient perovskite solar cells is still a major drawback, cross-sectional FM-KPFM studies on degraded cells could help to localize the interfaces at which the main issues are evolving.

The possibility to bring the perovskite solar cell as an alternative photovoltaic device on the market could also face a problem from the aspect of toxicity. In order to overcome this problem, it is beneficial to get rid of the toxicity with Pb-free perovskite materials.[139]

As a final step the small samples from the research labs need to be upscaled by means of an industrial fabrication process. However, this is a challenge which would need to be tackled from the industry side. A way to complement existing technology would also be to combine the perovskite cell with Si-based cells to form a tandem cell. Since the absorption of light for these technologies covers a different range of the sun's spectrum, the tandem cell is supposed to achieve much higher efficiencies for same space requirements.[140]

With further successful work in this direction, perovskite solar cells remain a promising candidate to revolutionize the photovoltaic market.

7. Bibliography

“Science literacy is the artery through which the solutions of tomorrow's problems flow.”
— Neil deGrasse Tyson

1. Miller, R. G.; Sorrell, S. R., The future of oil supply. *Philosophical Transactions of the Royal Society A: Mathematical, Physical and Engineering Sciences* **2014,** *372* (2006).
2. Stocker, T. F., D. Qin, G.-K. Plattner, M. Tignor, S.K. Allen, J. Boschung, A. Nauels, Y. Xia, V. Bex and P.M. Midgley, IPCC, **2013**: Climate Change 2013: The Physical Science Basis. Contribution of Working Group I to the Fifth Assessment Report of the Intergovernmental Panel on Climate Change. In *Cambridge University Press*, United Kingdom and New York, NY, USA, 2013; p 1535 pp.
3. OECD/IEA *World Energy Outlook Special Report*; **2015**.
4. Wang, Q.; Page, M. R.; Iwaniczko, E.; Xu, Y.; Roybal, L.; Bauer, R.; To, B.; Yuan, H.-C.; Duda, A.; Hasoon, F.; Yan, Y. F.; Levi, D.; Meier, D.; Branz, H. M.; Wang, T. H., Efficient heterojunction solar cells on p-type crystal silicon wafers. *Applied Physics Letters* **2010,** *96* (1), 013507.
5. Edri, E.; Kirmayer, S.; Mukhopadhyay, S.; Gartsman, K.; Hodes, G.; Cahen, D., Elucidating the Charge Carrier Separation and Working Mechanism of CH3NH3PbI3−xClx Perovskite Solar Cells. *Nat. Commun.* **2014,** *5*.
6. Shockley, W.; Queisser, H. J., Detailed Balance Limit of Efficiency of p-n Junction Solar Cells. *Journal of Applied Physics* **1961,** *32* (3), 510-519.
7. Tiedje, T.; Yablonovitch, E.; Cody, G. D.; Brooks, B. G., Limiting efficiency of silicon solar cells. *IEEE Transactions on Electron Devices* **1984,** *31* (5), 711-716.
8. Shockley, W., The Theory of p-n Junctions in Semiconductors and p-n Junction Transistors. *Bell System Technical Journal* **1949,** *28* (3), 435-489.
9. De Wolf, S.; Descoeudres, A.; Holman Zachary, C.; Ballif, C., High-efficiency Silicon Heterojunction Solar Cells: A Review. In *green*, **2012**; Vol. 2, p 7.
10. O'Regan, B.; Gratzel, M., A low-cost, high-efficiency solar cell based on dye-sensitized colloidal TiO2 films. *Nature* **1991,** *353* (6346), 737-740.
11. Grätzel, M., Dye-sensitized solar cells. *Journal of Photochemistry and Photobiology C: Photochemistry Reviews* **2003,** *4* (2), 145-153.
12. Sommeling, P. M.; Späth, M.; Smit, H. J. P.; Bakker, N. J.; Kroon, J. M., Long-term stability testing of dye-sensitized solar cells. *Journal of Photochemistry and Photobiology A: Chemistry* **2004,** *164* (1–3), 137-144.
13. Kazim, S.; Nazeeruddin, M. K.; Grätzel, M.; Ahmad, S., Perovskite as Light Harvester: A Game Changer in Photovoltaics. *Angew. Chem., Int. Ed.* **2014,** *53* (11), 2812-2824.
14. Bhalla, S. A.; Guo, R.; Roy, R., The perovskite structure – a review of its role in ceramic science and technology. *Material Research Innovations* **2000,** *4* (1), 3-26.

15. Kojima, A.; Teshima, K.; Shirai, Y.; Miyasaka, T., Organometal Halide Perovskites as Visible-Light Sensitizers for Photovoltaic Cells. *J. Am. Chem. Soc.* **2009,** *131* (17), 6050-6051.
16. Im, J.-H.; Lee, C.-R.; Lee, J.-W.; Park, S.-W.; Park, N.-G., 6.5% efficient perovskite quantum-dot-sensitized solar cell. *Nanoscale* **2011,** *3* (10), 4088-4093.
17. Kim, H.-S.; Lee, C.-R.; Im, J.-H.; Lee, K.-B.; Moehl, T.; Marchioro, A.; Moon, S.-J.; Humphry-Baker, R.; Yum, J.-H.; Moser, J. E.; Gratzel, M.; Park, N.-G., Lead Iodide Perovskite Sensitized All-Solid-State Submicron Thin Film Mesoscopic Solar Cell with Efficiency Exceeding 9%. *Sci. Rep.* **2012,** *2*, 591.
18. Etgar, L.; Gao, P.; Xue, Z.; Peng, Q.; Chandiran, A. K.; Liu, B.; Nazeeruddin, M. K.; Grätzel, M., Mesoscopic CH3NH3PbI3/TiO2 Heterojunction Solar Cells. *Journal of the American Chemical Society* **2012,** *134* (42), 17396-17399.
19. Lee, M. M.; Teuscher, J.; Miyasaka, T.; Murakami, T. N.; Snaith, H. J., Efficient Hybrid Solar Cells Based on Meso-Superstructured Organometal Halide Perovskites. *Science* **2012,** *338* (6107), 643-647.
20. Ball, J. M.; Lee, M. M.; Hey, A.; Snaith, H. J., Low-temperature processed meso-superstructured to thin-film perovskite solar cells. *Energy & Environmental Science* **2013,** *6* (6), 1739-1743.
21. Liu, M.; Johnston, M. B.; Snaith, H. J., Efficient planar heterojunction perovskite solar cells by vapour deposition. *Nature* **2013,** *advance online publication*.
22. Stranks, S. D.; Eperon, G. E.; Grancini, G.; Menelaou, C.; Alcocer, M. J. P.; Leijtens, T.; Herz, L. M.; Petrozza, A.; Snaith, H. J., Electron-Hole Diffusion Lengths Exceeding 1 Micrometer in an Organometal Trihalide Perovskite Absorber. *Science* **2013,** *342* (6156), 341-344.
23. Xing, G.; Mathews, N.; Sun, S.; Lim, S. S.; Lam, Y. M.; Grätzel, M.; Mhaisalkar, S.; Sum, T. C., Long-Range Balanced Electron- and Hole-Transport Lengths in Organic-Inorganic CH3NH3PbI3. *Science* **2013,** *342* (6156), 344-347.
24. Wehrenfennig, C.; Eperon, G. E.; Johnston, M. B.; Snaith, H. J.; Herz, L. M., High Charge Carrier Mobilities and Lifetimes in Organolead Trihalide Perovskites. *Advanced Materials* **2014,** *26* (10), 1584-1589.
25. Miyata, A.; Mitioglu, A.; Plochocka, P.; Portugall, O.; Wang, J. T.-W.; Stranks, S. D.; Snaith, H. J.; Nicholas, R. J., Direct measurement of the exciton binding energy and effective masses for charge carriers in organic-inorganic tri-halide perovskites. *Nat Phys* **2015,** *11* (7), 582-587.
26. Gratzel, M., The light and shade of perovskite solar cells. *Nat Mater* **2014,** *13* (9), 838-842.
27. Im, J.-H.; Jang, I.-H.; Pellet, N.; Grätzel, M.; Park, N.-G., Growth of CH3NH3PbI3 cuboids with controlled size for high-efficiency perovskite solar cells. *Nat Nano* **2014,** *9* (11), 927-932.

28. Bi, D.; Yi, C.; Luo, J.; Décoppet, J.-D.; Zhang, F.; Zakeeruddin, Shaik M.; Li, X.; Hagfeldt, A.; Grätzel, M., Polymer-templated nucleation and crystal growth of perovskite films for solar cells with efficiency greater than 21%. *Nature Energy* **2016,** *1*, 16142.
29. Saliba, M.; Correa-Baena, J. P.; Grätzel, M.; Hagfeldt, A.; Abate, A., Perovskite Solar Cells: From the Atomic Level to Film Quality and Device Performance. *Angewandte Chemie International Edition* **2018,** *57* (10), 2554-2569.
30. Best Research cells efficiencies. *http://www.nrel.gov/ncpv/images/efficiency_chart.jpg*, Date of access: 2019/04/15.
31. Jeon, N. J.; Noh, J. H.; Yang, W. S.; Kim, Y. C.; Ryu, S.; Seo, J.; Seok, S. I., Compositional engineering of perovskite materials for high-performance solar cells. *Nature* **2015,** *517* (7535), 476-480.
32. Bi, D.; Tress, W.; Dar, M. I.; Gao, P.; Luo, J.; Renevier, C.; Schenk, K.; Abate, A.; Giordano, F.; Correa Baena, J.-P.; Decoppet, J.-D.; Zakeeruddin, S. M.; Nazeeruddin, M. K.; Grätzel, M.; Hagfeldt, A., Efficient luminescent solar cells based on tailored mixed-cation perovskites. *Science Advances* **2016,** *2* (1).
33. Baikie, T.; Fang, Y.; Kadro, J. M.; Schreyer, M.; Wei, F.; Mhaisalkar, S. G.; Graetzel, M.; White, T. J., Synthesis and crystal chemistry of the hybrid perovskite (CH3NH3)PbI3 for solid-state sensitised solar cell applications. *Journal of Materials Chemistry A* **2013,** *1* (18), 5628-5641.
34. Tress, W., Maximum Efficiency and Open-Circuit Voltage of Perovskite Solar Cells. In *Organic-Inorganic Halide Perovskite Photovoltaics: From Fundamentals to Device Architectures*, Park, N.-G.; Grätzel, M.; Miyasaka, T., Eds. Springer International Publishing: Cham, **2016**; pp 53-77.
35. Gujar, T. P.; Thelakkat, M., Highly Reproducible and Efficient Perovskite Solar Cells with Extraordinary Stability from Robust CH3NH3PbI3: Towards Large-Area Devices. *Energy Technology* **2016,** *4* (3), 449-457.
36. Noh, J. H.; Im, S. H.; Heo, J. H.; Mandal, T. N.; Seok, S. I., Chemical Management for Colorful, Efficient, and Stable Inorganic–Organic Hybrid Nanostructured Solar Cells. *Nano Letters* **2013,** *13* (4), 1764-1769.
37. Li, D.; Bretschneider, S. A.; Bergmann, V. W.; Hermes, I. M.; Mars, J.; Klasen, A.; Lu, H.; Tremel, W.; Mezger, M.; Butt, H.-J.; Weber, S. A. L.; Berger, R., Humidity-Induced Grain Boundaries in MAPbI3 Perovskite Films. *J. Phys. Chem. C* **2016,** *120* (12), 6363-6368.
38. Niu, G.; Li, W.; Meng, F.; Wang, L.; Dong, H.; Qiu, Y., Study on the stability of CH3NH3PbI3 films and the effect of post-modification by aluminum oxide in all-solid-state hybrid solar cells. *Journal of Materials Chemistry A* **2014,** *2* (3), 705-710.

39. Yang, J.; Siempelkamp, B. D.; Liu, D.; Kelly, T. L., Investigation of CH3NH3PbI3 Degradation Rates and Mechanisms in Controlled Humidity Environments Using in Situ Techniques. *ACS Nano* **2015,** *9* (2), 1955-1963.
40. Snaith, H. J.; Abate, A.; Ball, J. M.; Eperon, G. E.; Leijtens, T.; Noel, N. K.; Stranks, S. D.; Wang, J. T.-W.; Wojciechowski, K.; Zhang, W., Anomalous Hysteresis in Perovskite Solar Cells. *J. Phys. Chem. Lett.* **2014,** *5* (9), 1511-1515.
41. Unger, E. L.; Hoke, E. T.; Bailie, C. D.; Nguyen, W. H.; Bowring, A. R.; Heumuller, T.; Christoforo, M. G.; McGehee, M. D., Hysteresis and Transient Behavior in Current-Voltage Measurements of Hybrid-Perovskite Absorber Solar Cells. *Energy Environ. Sci.* **2014,** *7* (11), 3690-3698.
42. Tress, W.; Marinova, N.; Moehl, T.; Zakeeruddin, S. M.; Nazeeruddin, M. K.; Gratzel, M., Understanding the Rate-Dependent J-V hysteresis, Slow Time Component, and Aging in CH3NH3PbI3 Perovskite Solar Cells: The Role of a Compensated Electric Field. *Energy Environ. Sci.* **2015,** *8* (3), 995-1004.
43. Bryant, D.; Wheeler, S.; O'Regan, B. C.; Watson, T.; Barnes, P. R. F.; Worsley, D.; Durrant, J., Observable Hysteresis at Low Temperature in "Hysteresis Free" Organic–Inorganic Lead Halide Perovskite Solar Cells. *The Journal of Physical Chemistry Letters* **2015,** *6* (16), 3190-3194.
44. O'Regan, B. C.; Barnes, P. R. F.; Li, X.; Law, C.; Palomares, E.; Marin-Beloqui, J. M., Optoelectronic Studies of Methylammonium Lead Iodide Perovskite Solar Cells with Mesoporous TiO2: Separation of Electronic and Chemical Charge Storage, Understanding Two Recombination Lifetimes, and the Evolution of Band Offsets during J–V Hysteresis. *J. Am. Chem. Soc.* **2015,** *137* (15), 5087-5099.
45. Tress, W.; Correa Baena, J. P.; Saliba, M.; Abate, A.; Graetzel, M., Inverted Current–Voltage Hysteresis in Mixed Perovskite Solar Cells: Polarization, Energy Barriers, and Defect Recombination. *Advanced Energy Materials* **2016,** *6* (19), 1600396-n/a.
46. Shao, Y.; Xiao, Z.; Bi, C.; Yuan, Y.; Huang, J., Origin and Elimination of Photocurrent Hysteresis by Fullerene Passivation in CH3NH3PbI3 Planar Heterojunction Solar Cells. *Nat. Commun.* **2014,** *5*, 5784.
47. Christians, J. A.; Manser, J. S.; Kamat, P. V., Best Practices in Perovskite Solar Cell Efficiency Measurements. Avoiding the Error of Making Bad Cells Look Good. *The Journal of Physical Chemistry Letters* **2015,** *6* (5), 852-857.
48. de Quilettes, D. W.; Vorpahl, S. M.; Stranks, S. D.; Nagaoka, H.; Eperon, G. E.; Ziffer, M. E.; Snaith, H. J.; Ginger, D. S., Impact of microstructure on local carrier lifetime in perovskite solar cells. *Science* **2015,** *348* (6235), 683-686.
49. Edri, E.; Kirmayer, S.; Henning, A.; Mukhopadhyay, S.; Gartsman, K.; Rosenwaks, Y.; Hodes, G.; Cahen, D., Why Lead Methylammonium Tri-Iodide Perovskite-Based Solar Cells Require a Mesoporous Electron

Transporting Scaffold (but Not Necessarily a Hole Conductor). *Nano Lett.* **2014,** *14* (2), 1000-1004.
50. Binnig, G.; Rohrer, H.; Gerber, C.; Weibel, E., Surface Studies by Scanning Tunneling Microscopy. *Physical Review Letters* **1982,** *49* (1), 57-61.
51. Binnig, G.; Quate, C. F.; Gerber, C., Atomic Force Microscope. *Physical Review Letters* **1986,** *56* (9), 930-933.
52. García, R.; Pérez, R., Dynamic atomic force microscopy methods. *Surface Science Reports* **2002,** *47* (6–8), 197-301.
53. Martin, Y.; Wickramasinghe, H. K., Magnetic imaging by ''force microscopy'' with 1000 Å resolution. *Applied Physics Letters* **1987,** *50* (20), 1455-1457.
54. Martin, Y.; Abraham, D. W.; Wickramasinghe, H. K., High-resolution capacitance measurement and potentiometry by force microscopy. *Applied Physics Letters* **1988,** *52* (13), 1103-1105.
55. Nonnenmacher, M.; O'Boyle, M. P.; Wickramasinghe, H. K., Kelvin probe force microscopy. *Applied Physics Letters* **1991,** *58* (25), 2921-2923.
56. Kikukawa, A.; Hosaka, S.; Imura, R., Silicon pn junction imaging and characterizations using sensitivity enhanced Kelvin probe force microscopy. *Applied Physics Letters* **1995,** *66* (25), 3510-3512.
57. Colchero, J.; Gil, A.; Baró, A. M., Resolution Enhancement and Improved Data Interpretation in Electrostatic Force Microscopy. *Phys. Rev. B* **2001,** *64* (24), 245403.
58. Gil, A.; Colchero, J.; Gómez-Herrero, J.; Baró, A. M., Electrostatic Force Gradient Signal: Resolution Enhancement in Electrostatic Force Microscopy and Improved Kelvin Probe Microscopy. *Nanotechnology* **2003,** *14* (2), 332-340.
59. Glatzel, T.; Sadewasser, S.; Lux-Steiner, M. C., Amplitude or Frequency Modulation-Detection in Kelvin Probe Force Microscopy. *Appl. Surf. Sci.* **2003,** *210* (1–2), 84-89.
60. Zerweck, U.; Loppacher, C.; Otto, T.; Grafström, S.; Eng, L. M., Accuracy and Resolution Limits of Kelvin Probe Force Microscopy. *Phys. Rev. B* **2005,** *71* (12), 125424.
61. Ziegler, D.; Stemmer, A., Force Gradient Sensitive Detection in Lift-Mode Kelvin Probe Force Microscopy. *Nanotechnology* **2011,** *22* (7), 075501.
62. Cohen, G.; Halpern, E.; Nanayakkara, S. U.; Luther, J. M.; Held, C.; Bennewitz, R.; Boag, A.; Rosenwaks, Y., Reconstruction of surface potential from Kelvin probe force microscopy images. *Nanotechnology* **2013,** *24* (29), 295702.
63. Nonnenmacher, M.; O'Boyle, M.; Wickramasinghe, H. K., Surface investigations with a Kelvin probe force microscope. *Ultramicroscopy* **1992,** *42*, 268-273.

64. Takao, U.; Masashi, A.; Shigeru, K.; Takashi, M.; Toshiaki, K.; Hidetoshi, I., Cross-Sectional Potential Imaging of Compound Semiconductor Heterostructure by Kelvin Probe Force Microscopy. *Japanese Journal of Applied Physics* **1998,** *37* (3S), 1522.
65. Takashi, M.; Takao, U.; Shigeru, K.; Koichi, M., Measurement of Contact Potential of GaAs pn Junctions by Kelvin Probe Force Microscopy. *Jpn. J. Appl. Phys.* **1999,** *38* (8R), 4893.
66. Ballif, C.; Moutinho, H. R.; Al-Jassim, M. M., Cross-sectional electrostatic force microscopy of thin-film solar cells. *Journal of Applied Physics* **2001,** *89* (2), 1418-1424.
67. Glatzel, T.; Marrón, D. F.; Schedel-Niedrig, T.; Sadewasser, S.; Lux-Steiner, M. C., CuGaSe2 Solar Cell Cross Section Studied by Kelvin Probe Force Microscopy in Ultrahigh Vacuum. *Appl. Phys. Lett.* **2002,** *81* (11), 2017-2019.
68. Jiang, C.-S.; Moutinho, H. R.; Geisz, J. F.; Friedman, D. J.; Al-Jassim, M. M., Direct measurement of electrical potentials in GaInP2 solar cells. *Applied Physics Letters* **2002,** *81* (14), 2569-2571.
69. Jiang, C.-S.; Hasoon, F. S.; Moutinho, H. R.; Al-Thani, H. A.; Romero, M. J.; Al-Jassim, M. M., Direct Evidence of a Buried Homojunction in Cu(In,Ga)Se2 Solar Cells. *Appl. Phys. Lett.* **2003,** *82* (1), 127-129.
70. Jiang, C.-S.; Friedman, D. J.; Geisz, J. F.; Moutinho, H. R.; Romero, M. J.; Al-Jassim, M. M., Distribution of built-in electrical potential in GaInP2/GaAs tandem-junction solar cells. *Applied Physics Letters* **2003,** *83* (8), 1572-1574.
71. Jiang, C.-S.; Moutinho, H. R.; Friedman, D. J.; Geisz, J. F.; Al-Jassim, M. M., Measurement of built-in electrical potential in III–V solar cells by scanning Kelvin probe microscopy. *Journal of Applied Physics* **2003,** *93* (12), 10035-10040.
72. Visoly-Fisher, I.; Cohen, S. R.; Cahen, D.; Ferekides, C. S., Electronically active layers and interfaces in polycrystalline devices: Cross-section mapping of CdS/CdTe solar cells. *Applied Physics Letters* **2003,** *83* (24), 4924-4926.
73. Glatzel, T.; Steigert, H.; Sadewasser, S.; Klenk, R.; Lux-Steiner, M. C., Potential distribution of Cu(In,Ga)(S,Se)2-solar cell cross-sections measured by Kelvin probe force microscopy. *Thin Solid Films* **2005,** *480–481*, 177-182.
74. Jiang, C.-S.; Noufi, R.; Ramanathan, K.; AbuShama, J. A.; Moutinho, H. R.; Al-Jassim, M. M., Does the local built-in potential on grain boundaries of Cu(In,Ga)Se2 thin films benefit photovoltaic performance of the device? *Applied Physics Letters* **2004,** *85* (13), 2625-2627.
75. Mainz, R.; Streicher, F.; Abou-Ras, D.; Sadewasser, S.; Klenk, R.; Lux-Steiner, M. C., Combined analysis of spatially resolved electronic structure

and composition on a cross-section of a thin film Cu(In1–xGax)S2 solar cell. *physica status solidi (a)* **2009,** *206* (5), 1017-1020.
76. Lee, J.; Kong, J.; Kim, H.; Kang, S.-O.; Lee, K., Direct Observation of Internal Potential Distributions in a Bulk Heterojunction Solar Cell. *Appl. Phys. Lett.* **2011,** *99* (24), 243301.
77. Kong, J.; Lee, J.; Jeong, Y.; Kim, M.; Kang, S.-O.; Lee, K., Biased Internal Potential Distributions in a Bulk-Heterojunction Organic Solar Cell Incorporated with a TiOx Interlayer. *Appl. Phys. Lett.* **2012,** *100* (21), 213305.
78. Zhang, Z.; Tang, X.; Kiowski, O.; Hetterich, M.; Lemmer, U.; Powalla, M.; Hölscher, H., Reevaluation of the beneficial effect of Cu(In,Ga)Se2 grain boundaries using Kelvin probe force microscopy. *Applied Physics Letters* **2012,** *100* (20), 203903.
79. Saive, R.; Scherer, M.; Mueller, C.; Daume, D.; Schinke, J.; Kroeger, M.; Kowalsky, W., Imaging the Electric Potential within Organic Solar Cells. *Adv. Funct. Mater.* **2013,** *23* (47), 5854-5860.
80. Scherer, M.; Saive, R.; Daume, D.; Kröger, M.; Kowalsky, W., Sample Preparation for Scanning Kelvin Probe Microscopy Studies on Cross Sections of Organic Solar Cells. *AIP Adv.* **2013,** *3* (9), 092134.
81. Zhang, Z.; Hetterich, M.; Lemmer, U.; Powalla, M.; Hölscher, H., Cross Sections of Operating Cu(In,Ga)Se2 Thin-Film Solar Cells under Defined White Light Illumination Analyzed by Kelvin Probe Force Microscopy. *Appl. Phys. Lett.* **2013,** *102* (2), 023903.
82. Ballif, C.; Moutinho, H. R.; Hasoon, F. S.; Dhere, R. G.; Al-Jassim, M. M., Cross-sectional atomic force microscopy imaging of polycrystalline thin films. *Ultramicroscopy* **2000,** *85* (2), 61-71.
83. Bergmann, V. W., Potentialverläufe in organischen Solarzellen, Diplomarbeit zur Erlangung des Grades "Diplomphysiker" am Fachbereich Physik der Johannes Gutenberg-Universität in Mainz. **2013**.
84. Berger, R.; Domanski, A. L.; Weber, S. A. L., Electrical Characterization of Organic Solar Cell Materials Based on Scanning Force Microscopy. *Eur. Polym. J.* **2013,** *49* (8), 1907-1915.
85. Savitzky, A.; Golay, M. J. E., Smoothing and Differentiation of Data by Simplified Least Squares Procedures. *Analytical Chemistry* **1964,** *36* (8), 1627-1639.
86. Burschka, J.; Pellet, N.; Moon, S.-J.; Humphry-Baker, R.; Gao, P.; Nazeeruddin, M. K.; Gratzel, M., Sequential Deposition as a Route to High-Performance Perovskite-Sensitized Solar Cells. *Nature* **2013,** *499* (7458), 316-319.
87. Bergmann, V. W.; Weber, S. A. L.; Javier Ramos, F.; Nazeeruddin, M. K.; Grätzel, M.; Li, D.; Domanski, A. L.; Lieberwirth, I.; Ahmad, S.; Berger, R., Real-Space Observation of Unbalanced Charge Distribution Inside a Perovskite-Sensitized Solar Cell. *Nat. Commun.* **2014,** *5*, 5001.

88. Introduction to Energy Dispersive X-ray Spectrometry (EDS). *Central Facility for Advanced Microscopy and Microanalysis*
89. Yin, W.-J.; Shi, T.; Yan, Y., Unusual Defect Physics in CH3NH3PbI3 Perovskite Solar Cell Absorber. *Appl. Phys. Lett.* **2014,** *104* (6), 063903.
90. Wang, Q.; Shao, Y.; Xie, H.; Lyu, L.; Liu, X.; Gao, Y.; Huang, J., Qualifying composition dependent p and n self-doping in CH3NH3PbI3. *Applied Physics Letters* **2014,** *105* (16), 163508.
91. Kim, J.; Lee, S.-H.; Lee, J. H.; Hong, K.-H., The Role of Intrinsic Defects in Methylammonium Lead Iodide Perovskite. *J. Phys. Chem. Lett.* **2014,** *5* (8), 1312-1317.
92. Hermes, I. M.; Hou, Y.; Bergmann, V. W.; Brabec, C. J.; Weber, S. A. L., The Interplay of Contact Layers: How the Electron Transport Layer Influences Interfacial Recombination and Hole Extraction in Perovskite Solar Cells. *The Journal of Physical Chemistry Letters* **2018,** *9* (21), 6249-6256.
93. Laban, W. A.; Etgar, L., Depleted hole conductor-free lead halide iodide heterojunction solar cells. *Energy & Environmental Science* **2013,** *6* (11), 3249-3253.
94. You, J.; Hong, Z.; Yang, Y.; Chen, Q.; Cai, M.; Song, T.-B.; Chen, C.-C.; Lu, S.; Liu, Y.; Zhou, H.; Yang, Y., Low-Temperature Solution-Processed Perovskite Solar Cells with High Efficiency and Flexibility. *ACS Nano* **2014,** *8* (2), 1674-1680.
95. Schulz, P.; Edri, E.; Kirmayer, S.; Hodes, G.; Cahen, D.; Kahn, A., Interface energetics in organo-metal halide perovskite-based photovoltaic cells. *Energy & Environmental Science* **2014,** *7* (4), 1377-1381.
96. Miller, E. M.; Zhao, Y.; Mercado, C. C.; Saha, S. K.; Luther, J. M.; Zhu, K.; Stevanovic, V.; Perkins, C. L.; van de Lagemaat, J., Substrate-controlled band positions in CH3NH3PbI3 perovskite films. *Physical Chemistry Chemical Physics* **2014,** *16* (40), 22122-22130.
97. Andersson, A.; Johansson, N.; Bröms, P.; Yu, N.; Lupo, D.; Salaneck, W. R., Fluorine Tin Oxide as an Alternative to Indium Tin Oxide in Polymer LEDs. *Advanced Materials* **1998,** *10* (11), 859-863.
98. Michaelson, H. B., The work function of the elements and its periodicity. *Journal of Applied Physics* **1977,** *48* (11), 4729-4733.
99. Kirchartz, T.; Bisquert, J.; Mora-Sero, I.; Garcia-Belmonte, G., Classification of solar cells according to mechanisms of charge separation and charge collection. *Physical Chemistry Chemical Physics* **2015,** *17* (6), 4007-4014.
100. Bergmann, V. W.; Guo, Y.; Tanaka, H.; Hermes, I. M.; Li, D.; Klasen, A.; Bretschneider, S. A.; Nakamura, E.; Berger, R.; Weber, S. A. L., Local Time-Dependent Charging in a Perovskite Solar Cell. *ACS Applied Materials & Interfaces* **2016,** *8* (30), 19402-19409.

101. Dweydari, A. W.; Mee, C. H. B., Work Function Measurements on (100) and (110) Surfaces of Silver. *Phys. Status Solidi A* **1975,** *27* (1), 223-230.
102. Schlaf, R.; Murata, H.; Kafafi, Z. H., Work Function Measurements on Indium Tin Oxide Films. *J. Electron Spectrosc. Relat. Phenom.* **2001,** *120* (1–3), 149-154.
103. Jiang, C.-S.; Yang, M.; Zhou, Y.; To, B.; Nanayakkara, S. U.; Luther, J. M.; Zhou, W.; Berry, J. J.; van de Lagemaat, J.; Padture, N. P.; Zhu, K.; Al-Jassim, M. M., Carrier Separation and Transport in Perovskite Solar Cells Studied by Nanometre-Scale Profiling of Electrical Potential. *Nat. Commun.* **2015,** *6*, 8397.
104. Guerrero, A.; Juarez-Perez, E. J.; Bisquert, J.; Mora-Sero, I.; Garcia-Belmonte, G., Electrical Field Profile and Doping in Planar Lead Halide Perovskite Solar Cells. *Appl. Phys. Lett.* **2014,** *105* (13), 133902.
105. Dymshits, A.; Henning, A.; Segev, G.; Rosenwaks, Y.; Etgar, L., The Electronic Structure of Metal Oxide/Organo Metal Halide Perovskite Junctions in Perovskite Based Solar Cells. *Sci. Rep.* **2015,** *5*, 8704.
106. van Reenen, S.; Kemerink, M.; Snaith, H. J., Modeling Anomalous Hysteresis in Perovskite Solar Cells. *J. Phys. Chem. Lett.* **2015,** *6* (19), 3808-3814.
107. Richardson, G.; O'Kane, S. E. J.; Niemann, R. G.; Peltola, T. A.; Foster, J. M.; Cameron, P. J.; Walker, A. B., Can Slow-Moving Ions Explain Hysteresis in the Current-Voltage Curves of Perovskite Solar Cells? *Energy Environ. Sci.* **2016,** *9* (4), 1476-1485.
108. Eames, C.; Frost, J. M.; Barnes, P. R. F.; O'Regan, B. C.; Walsh, A.; Islam, M. S., Ionic Transport in Hybrid Lead Iodide Perovskite Solar Cells. *Nat. Commun.* **2015,** *6*, 7497.
109. Azpiroz, J. M.; Mosconi, E.; Bisquert, J.; De Angelis, F., Defect Migration in Methylammonium Lead Iodide and its Role in Perovskite Solar Cell Operation. *Energy Environ. Sci.* **2015,** *8* (7), 2118-2127.
110. Giordano, F.; Abate, A.; Correa Baena, J. P.; Saliba, M.; Matsui, T.; Im, S. H.; Zakeeruddin, S. M.; Nazeeruddin, M. K.; Hagfeldt, A.; Graetzel, M., Enhanced electronic properties in mesoporous TiO2 via lithium doping for high-efficiency perovskite solar cells. *Nature Communications* **2016,** *7*, 10379.
111. Correa Baena, J. P.; Steier, L.; Tress, W.; Saliba, M.; Neutzner, S.; Matsui, T.; Giordano, F.; Jacobsson, T. J.; Srimath Kandada, A. R.; Zakeeruddin, S. M.; Petrozza, A.; Abate, A.; Nazeeruddin, M. K.; Gratzel, M.; Hagfeldt, A., Highly efficient planar perovskite solar cells through band alignment engineering. *Energy & Environmental Science* **2015,** *8* (10), 2928-2934.
112. Cai, M.; Ishida, N.; Li, X.; Yang, X.; Noda, T.; Wu, Y.; Xie, F.; Naito, H.; Fujita, D.; Han, L., Control of Electrical Potential Distribution for High-Performance Perovskite Solar Cells. *Joule* **2018,** *2* (2), 296-306.

113. Frost, J. M.; Walsh, A., Molecular Motion and Dynamic Crystal Structures of Hybrid Halide Perovskites. In *Organic-Inorganic Halide Perovskite Photovoltaics: From Fundamentals to Device Architectures*, Park, N.-G.; Grätzel, M.; Miyasaka, T., Eds. Springer International Publishing: Cham, **2016**; pp 1-17.
114. Walsh, A.; Scanlon, D. O.; Chen, S.; Gong, X. G.; Wei, S.-H., Self-Regulation Mechanism for Charged Point Defects in Hybrid Halide Perovskites. *Angewandte Chemie International Edition* **2015,** *54* (6), 1791-1794.
115. Egger, D. A.; Kronik, L.; Rappe, A. M., Theory of Hydrogen Migration in Organic–Inorganic Halide Perovskites. *Angewandte Chemie International Edition* **2015,** *54* (42), 12437-12441.
116. Yuan, Y.; Chae, J.; Shao, Y.; Wang, Q.; Xiao, Z.; Centrone, A.; Huang, J., Photovoltaic Switching Mechanism in Lateral Structure Hybrid Perovskite Solar Cells. *Advanced Energy Materials* **2015,** *5* (15), 1500615-n/a.
117. Haruyama, J.; Sodeyama, K.; Han, L.; Tateyama, Y., First-Principles Study of Ion Diffusion in Perovskite Solar Cell Sensitizers. *Journal of the American Chemical Society* **2015,** *137* (32), 10048-10051.
118. Yuan, Y.; Wang, Q.; Huang, J., Ion Migration in Hybrid Perovskite Solar Cells. In *Organic-Inorganic Halide Perovskite Photovoltaics: From Fundamentals to Device Architectures*, Park, N.-G.; Grätzel, M.; Miyasaka, T., Eds. Springer International Publishing: Cham, **2016**; pp 137-162.
119. Yu, H.; Lu, H.; Xie, F.; Zhou, S.; Zhao, N., Native Defect-Induced Hysteresis Behavior in Organolead Iodide Perovskite Solar Cells. *Advanced Functional Materials* **2016,** *26* (9), 1411-1419.
120. Choi, J. J.; Yang, X.; Norman, Z. M.; Billinge, S. J. L.; Owen, J. S., Structure of Methylammonium Lead Iodide Within Mesoporous Titanium Dioxide: Active Material in High-Performance Perovskite Solar Cells. *Nano Letters* **2014,** *14* (1), 127-133.
121. Wojciechowski, K.; Stranks, S. D.; Abate, A.; Sadoughi, G.; Sadhanala, A.; Kopidakis, N.; Rumbles, G.; Li, C.-Z.; Friend, R. H.; Jen, A. K. Y.; Snaith, H. J., Heterojunction Modification for Highly Efficient Organic–Inorganic Perovskite Solar Cells. *ACS Nano* **2014,** *8* (12), 12701-12709.
122. Wu, B.; Fu, K.; Yantara, N.; Xing, G.; Sun, S.; Sum, T. C.; Mathews, N., Charge Accumulation and Hysteresis in Perovskite-Based Solar Cells: An Electro-Optical Analysis. *Advanced Energy Materials* **2015,** *5* (19), 1500829-n/a.
123. Docampo, P.; Ball, J. M.; Darwich, M.; Eperon, G. E.; Snaith, H. J., Efficient organometal trihalide perovskite planar-heterojunction solar cells on flexible polymer substrates. *Nature Communications* **2013,** *4*, 2761.
124. Zhao, C.; Chen, B.; Qiao, X.; Luan, L.; Lu, K.; Hu, B., Revealing Underlying Processes Involved in Light Soaking Effects and Hysteresis

Phenomena in Perovskite Solar Cells. *Advanced Energy Materials* **2015,** *5* (14), 1500279-n/a.
125. Qin, P.; Domanski, A. L.; Chandiran, A. K.; Berger, R.; Butt, H.-J.; Dar, M. I.; Moehl, T.; Tetreault, N.; Gao, P.; Ahmad, S.; Nazeeruddin, M. K.; Gratzel, M., Yttrium-substituted nanocrystalline TiO2 photoanodes for perovskite based heterojunction solar cells. *Nanoscale* **2014,** *6* (3), 1508-1514.
126. Shkrob, I. A.; Marin, T. W., Charge Trapping in Photovoltaically Active Perovskites and Related Halogenoplumbate Compounds. *The Journal of Physical Chemistry Letters* **2014,** *5* (7), 1066-1071.
127. Leijtens, T.; Stranks, S. D.; Eperon, G. E.; Lindblad, R.; Johansson, E. M. J.; McPherson, I. J.; Rensmo, H.; Ball, J. M.; Lee, M. M.; Snaith, H. J., Electronic Properties of Meso-Superstructured and Planar Organometal Halide Perovskite Films: Charge Trapping, Photodoping, and Carrier Mobility. *ACS Nano* **2014,** *8* (7), 7147-7155.
128. Xiao, Z.; Yuan, Y.; Shao, Y.; Wang, Q.; Dong, Q.; Bi, C.; Sharma, P.; Gruverman, A.; Huang, J., Giant Switchable Photovoltaic Effect in Organometal Trihalide Perovskite Devices. *Nat. Mater.* **2015,** *14* (2), 193-198.
129. Anusca, I.; Balčiūnas, S.; Gemeiner, P.; Svirskas, Š.; Sanlialp, M.; Lackner, G.; Fettkenhauer, C.; Belovickis, J.; Samulionis, V.; Ivanov, M.; Dkhil, B.; Banys, J.; Shvartsman, V. V.; Lupascu, D. C., Dielectric Response: Answer to Many Questions in the Methylammonium Lead Halide Solar Cell Absorbers. *Advanced Energy Materials* **2017,** *7* (19), 1700600.
130. Zhao, Y.; Liang, C.; Zhang, H.; Li, D.; Tian, D.; Li, G.; Jing, X.; Zhang, W.; Xiao, W.; Liu, Q.; Zhang, F.; He, Z., Anomalously large interface charge in polarity-switchable photovoltaic devices: an indication of mobile ions in organic-inorganic halide perovskites. *Energy & Environmental Science* **2015,** *8* (4), 1256-1260.
131. Zarazua, I.; Bisquert, J.; Garcia-Belmonte, G., Light-Induced Space-Charge Accumulation Zone as Photovoltaic Mechanism in Perovskite Solar Cells. *J. Phys. Chem. Lett.* **2016,** *7* (3), 525-528.
132. Li, G.; Mao, B.; Lan, F.; Liu, L., Practical aspects of single-pass scan Kelvin probe force microscopy. *Review of Scientific Instruments* **2012,** *83* (11), 113701.
133. Axt, A.; Hermes, I. M.; Bergmann, V. W.; Tausendpfund, N.; Weber, S. A. L., Know your full potential: Quantitative Kelvin probe force microscopy on nanoscale electrical devices. *Beilstein Journal of Nanotechnology* **2018,** *9*, 1809-1819.
134. Charrier, D. S. H.; Kemerink, M.; Smalbrugge, B. E.; de Vries, T.; Janssen, R. A. J., Real versus Measured Surface Potentials in Scanning Kelvin Probe Microscopy. *ACS Nano* **2008,** *2* (4), 622-626.

135. Joseph, L. G.; Jeremy, N. M., Fast, high-resolution surface potential measurements in air with heterodyne Kelvin probe force microscopy. *Nanotechnology* **2016,** *27* (24), 245705.
136. Chen, Q.; Mao, L.; Li, Y.; Kong, T.; Wu, N.; Ma, C.; Bai, S.; Jin, Y.; Wu, D.; Lu, W.; Wang, B.; Chen, L., Quantitative Operando Visualization of the Energy Band Depth Profile in Solar Cells. *Nat. Commun.* **2015,** *6*, 7745.
137. Saive, R.; Mueller, C.; Schinke, J.; Lovrincic, R.; Kowalsky, W., Understanding S-shaped current-voltage characteristics of organic solar cells: Direct measurement of potential distributions by scanning Kelvin probe. *Applied Physics Letters* **2013,** *103* (24), 243303.
138. Weber, S. A. L.; Hermes, I. M.; Turren-Cruz, S.-H.; Gort, C.; Bergmann, V. W.; Gilson, L.; Hagfeldt, A.; Graetzel, M.; Tress, W.; Berger, R., How the formation of interfacial charge causes hysteresis in perovskite solar cells. *Energy & Environmental Science,* **2018**, *11*, 2404-2413.
139. Ke, W.; Kanatzidis, M. G., Prospects for low-toxicity lead-free perovskite solar cells. *Nature Communications* **2019,** *10* (1), 965.
140. Werner, J.; Weng, C.-H.; Walter, A.; Fesquet, L.; Seif, J. P.; De Wolf, S.; Niesen, B.; Ballif, C., Efficient Monolithic Perovskite/Silicon Tandem Solar Cell with Cell Area >1 cm2. *The Journal of Physical Chemistry Letters* **2016,** *7* (1), 161-166.
141. Guo, Y.; Liu, C.; Inoue, K.; Harano, K.; Tanaka, H.; Nakamura, E., Enhancement in the Efficiency of an Organic-Inorganic Hybrid Solar Cell with a Doped P3HT Hole-Transporting Layer on a Void-Free Perovskite Active Layer. *J. Mater. Chem. A* **2014,** *2* (34), 13827-13830.
142. Xiao, M.; Huang, F.; Huang, W.; Dkhissi, Y.; Zhu, Y.; Etheridge, J.; Gray-Weale, A.; Bach, U.; Cheng, Y.-B.; Spiccia, L., A Fast Deposition-Crystallization Procedure for Highly Efficient Lead Iodide Perovskite Thin-Film Solar Cells. *Angew. Chem., Int. Ed.* **2014,** *126* (37), 10056-10061.
143. Abate, A.; Leijtens, T.; Pathak, S.; Teuscher, J.; Avolio, R.; Errico, M. E.; Kirkpatrik, J.; Ball, J. M.; Docampo, P.; McPherson, I.; Snaith, H. J., Lithium salts as "redox active" p-type dopants for organic semiconductors and their impact in solid-state dye-sensitized solar cells. *Physical Chemistry Chemical Physics* **2013,** *15* (7), 2572-2579.
144. Abate, A.; Hollman, D. J.; Teuscher, J.; Pathak, S.; Avolio, R.; D'Errico, G.; Vitiello, G.; Fantacci, S.; Snaith, H. J., Protic Ionic Liquids as p-Dopant for Organic Hole Transporting Materials and Their Application in High Efficiency Hybrid Solar Cells. *Journal of the American Chemical Society* **2013,** *135* (36), 13538-13548.
145. Abate, A.; Staff, D. R.; Hollman, D. J.; Snaith, H. J.; Walker, A. B., Influence of ionizing dopants on charge transport in organic semiconductors. *Physical Chemistry Chemical Physics* **2014,** *16* (3), 1132-1138.

8. Acknowledgements

“The highest forms of understanding we can achieve are laughter and human compassion.”
— Richard Feynman

Laughter and human compassion also have been a great part of my PhD. In fact, this journey was full of many wonderful people I got to know on the way. Not only that I learned a lot about solar cells and atomic force microscopy, but the time also taught me a lot about life itself. It is highly unlikely that you master the challenge of a PhD all on your own. In fact you need people around you, that inspire, guide and support you on your way to achieve your goals. This chapter is dedicated to all of them and to say thanks to all of the inspiration they gave me.

First of all, I want to thank [redacted], who actually gave me the opportunity to work in his wonderful group. He has always been someone to look up to, taking so much time to support his students. In so many meetings it was always truly helpful to discuss about the projects with him and to work on new ideas. One could always learn from his knowledge, but also from his balanced spirit, being so calm and sensitive even when times were getting stressful.

For the next person I want to tell a little story from back in the days, about what it reminds me to have him as your project leader. As a young guy, just moved on from elementary school to Gymnasium, I got my first video game, which I loved to play. It was a video game where you played a wizard, who can walk around and collect things, which were then needed to interact at another place. It was full of riddles and was getting quite difficult sometimes. At times I did not know what to do anymore, there was a phone number to call (Internet was limited to just a few services at that point). That's why I called the number, told them at which situation I was stuck and they gave me a hint what I could do. I think it's obvious where this comparison is leading. Whenever, I had a problem with a measurement, did not know how to analyze the data or just needed some advice what to do next, I went to see my project leader [redacted]. He always had a good comment, helpful idea or just pushed me in the right direction. Ever since I got to know him from being my tutor in the second semester, his knowledge, skills and passion for science were truly inspiring.

Another big shout out is going to my previous project leader (and mentor of my mentor) [redacted]. I always appreciated his direct and honest comments. They kept me focused and helped me to understand the key points in giving presentations or scientific writing. He is also the one who supported me to get into the IRTG 1404 scholarship, a German-Korean collaboration program.

Within the IRTG 1404 I spent half a year at Seoul National University, which has been a unique experience that I don't want to miss in my life anymore. For that I also want to thank [redacted], who's been the German coordinator of the IRTG 1404 and accepted my application.

On the Korean side I want to thank [redacted], who has been hosting me at Seoul National University. Many thanks also to all the lovely members of the [redacted]. Further, I want to thank [redacted], who coordinated the IRTG 1404 from Korean side and always been very inviting.

Back to Germany many thanks to [redacted], who accepted me as a second supervisor at the University Mainz. Even though I missed to contact him more often and use his help, the times I contacted or visited him, he has always been very supportive and helped me to focus on discussing my project more accurately.

Talking about the University Mainz, there is another special person who deserves a lot of appreciation. Ever since the preparation course at the start of my studies, [redacted] was my fellow student, friend and companion through all the classes. He has been a big inspiration and help. Without him my physics studies would have both been more boring and challenging at the same time. It was also together with him, when I started at the Max-Planck-Institute for polymer research (MPIP) as a summer student.

During that time as a so called HiWi, I worked together with a lot of nice PhD students to support them on their projects. Many thanks to [redacted] for giving me the chance to work on their projects and get more experience in the field of science.

Also, not to forget about all my colleagues, with whom I was lucky to share the time at the MPIP and work on several projects. Special thanks to [redacted].

Without them, the work at MPIP would not run as smoothly as it does right now. It is only with the help of the technicians, especially [redacted] and all guys from the electronic workshop, that helped me to setup the equipment and run the measurements the way I did.

All of the important measurements for my thesis would have been impossible if not for the samples I received from my collaboration partners. Thanks to [redacted] from Abengoa Research Seville, [redacted] from the Ecole Polytechnique fédérale de Lausanne, and [redacted] from the University of Tokyo.

Being part of the IRTG 1404 and the wonderful German-Korean partnership made me get to know a lot of beautiful people. Thanks to all of you for the time and many

wonderful memories I don't want to miss in my life. Special thanks to [redacted]. From the Korean side special thanks to [redacted].

A special person from the older IRTG generation deserves a special thanks. He introduced me to so many new friends in Seoul and made Seoul feel like my second home. Thank you, [redacted]!

Besides my life as a scientist, there is another big part, which is so-to-say building the balance. Thanks to all my friends, business partners or simply inspiring people I met on the way. Thanks to my longtime friends [redacted]. Thanks to the whole [redacted] and especially my business partners [redacted] for giving me the possibility to start this amazing journey. Also, thanks to [redacted]. Thanks to [redacted] and all the creativity from the [redacted].

Without you two I would not be here and would not get the chance to experience anything like this. Thanks to the love and support, to my beloved parents [redacted]. Even when times were difficult, you always trusted me, that I will find my way and achieve my goals. Thank you for who you are and what you give to me. Also, thanks to my sister [redacted], for letting me look over your shoulder since I was a little boy, sitting on your desk while you were working on your projects. Thanks to my little special partner in crime [redacted], I'm still honored that you gave me a special name ("Kuka") as soon as you learned to speak. Thank you [redacted], I'm blessed to have such a wonderful family and team. Cannot think of anything better.

Last but not least thank you [redacted], for being who you are. The love of my life!

9. Curriculum Vitae

"Science is a wonderful thing if one does not have to earn one's living at it."

— Albert Einstein

Victor Wolfgang Bergmann
Date of birth: September 17th, 1986
Place of birth: Mainz, Germany
Nationality: German

Career:

Since 07/2016 Gutleut GbR - bar and exhibition space

Co-Founder/Consultant/Manager

- Organization of events
- Accounting/Management/HR

Since 05/2017 Park Systems Europe GmbH - Application Scientist

- Since 08/2018 Application and Service Manager
- Since 03/2019 "Prokurist"

Since 11/2018 Besserleut GbR - event space "Altes Postlager"

Co-Founder/Consultant/Manager

- Organization of events
- Accounting/Management

Dissertation:

Since 08/2013 PhD Physics

- Johannes-Gutenberg University Mainz/Max Planck Institute for polymer research
- Title: Inside perovskite solar cells – charges at interfaces

- Graduate college "International research training Group – IRTG 1404" Seoul National University - Depm. of Chemistry, Prof. Tae-Lim Choi
  - 08/2014-10/2014
  - 08/2015-11/2015
  - 02/2016-04/2016

Studies:

10/2007-06/2013 Diplom Physics

- Johannes Gutenberg University Mainz
- Title: Potential profiles in organic solar cells - Very good (1.5) (Externally at the Max Planck Institute for polymer research)

Until 03/2006 Gymnasium Gonsenheim Mainz, Germany

- Degree obtained: "Abitur" (university entrance exam)

Publication list:

first author

- Real-space observation of unbalanced charge distribution inside a perovskite-sensitized solar cell (*Nature Communications,* **2014**, *5,* 5001.)
- Local Time-Dependent Charging in a Perovskite Solar Cell *(ACS Appl. Mater. Interfaces*, **2016**, *8 (30).)*

co-author

- Enhanced Power Conversion Efficiency of Inverted Organic Solar Cells by Using Solution Processed Sn-Doped TiO_2 as an Electron Transport Layer *(J. Mater. Chem. A*, **2014**, *2*, 11426.)
- Surface Modification of TiO_2 Photoanodes with Fluorinated Self-Assembled Monolayers for Highly Efficient Dye-Sensitized Solar Cells (*ACS Appl. Mater. Interfaces*, **2015**, *7 (46)*.)
- Preparing DNA-mimicking multi-line nanocaterpillars via in situ nanoparticlisation of fully conjugated polymers (*Polym. Chem.*, **2016**, *7*, 1422-1428.)
- Ferroelastic Fingerprints in Methylammonium Lead Iodide Perovskite *(J. Phys. Chem. C*, **2016**, *120*, *10*, 5724-5731.*)*
- Humidity-Induced Grain Boundaries in $MAPbI_3$ Perovskite Films (*J. Phys. Chem. C*, **2016**, *120*, *12*, 6363-6368.)
- How the Formation of Interfacial Charge Causes Hysteresis in Perovskite Solar Cells (*Energy Environ. Sci.*, **2018**, *11*, 2404-2413.)

- Know your full potential: Quantitative Kelvin probe force microscopy on nanoscale electrical devices (*Beilstein J. Nanotechnol.,* **2018**, *9,* 1809–1819.)
- The Interplay of Contact Layers: How the Electron Transport Layer Influences Interfacial Recombination and Hole Extraction in Perovskite Solar Cells (*J. Phys. Chem. Lett.,* **2018**, *9, 21,* 6249-6256.)
- Removal of Surface Oxygen Vacancies increases Conductance through TiO_2 Thin Films for Perovskite Solar Cells (*J. Phys. Chem. C,* **2019**, *123, 22,* 13458-13466.)

Conferences/Workshops:

Oral Presentations at International Conferences:

- 12/2015 Pacific Chemistry Conference, Honolulu
- 03/2015 DPG Jahrestagung, Berlin
- 12/2014 MRS Fall Meeting, Boston

Poster Presentations at International Conferences:

- 09/2015 IRTG-Workshop, Korea Seoul
- 07/2015 IRTG-Conference, Germany Berlin
- 05/2015 IACIS, Germany Mainz
- 01/2015 IRTG-Meeting, Korea Gonjiam Resort
- 07/2014 IRTG-Meeting, Mainz
- 02/2014 IRTG-Meeting, Daejon
- 01/2014 ACSSSC Australia, Ballarat
- 08/2013 German-Korean Polymer Symposium, Hamburg

10. Appendix

"To explain all nature is too difficult a task for any one man or even for any one age."
— Isaac Newton

Appendix 1 – Recipe for fabricating the thick mesoporous perovskite cell:

Materials FTO-coated, 3-mm-thick glass (NSG10) was patterned by laser etching. Then, the substrates were cleaned and brushed using Hellmanex solution and rinsed with deionized water and ethanol; subsequently they were ultrasonicated in 2-propanol and rinsed again with ethanol and finally dried with compressed air. Prior to the compact layer deposition, the samples were cleaned with an ultraviolet/O3 treatment for 30 minutes. The TiO_2 compact layer was deposited by spin-coating an aqueous $TiCl_4$ solution (2M) at 5,000 rpm for 30 s. Then, the samples were heated at 125°C for 30 minutes. The TiO_2 mesoporous layer was prepared by spreading a solution of the commercial 18NR-T paste of Dyesol® diluted in pure ethanol (1 g of paste in 3.5 g of ethanol) over the compact titania layer, and spin-coated at 5000 rpm for 30 s. Then, the samples were sequentially heated to 125°C (5 min), 325°C (5 min), 375°C (5 min), 450°C (15 min) and finally 500°C (15 min) for the sintering process.

Next, the perovskite was prepared by sequential deposition[86]. For this, a first lead iodide (PbI_2) film was deposited by spin-coating (6500 rpm for 30 s with 5500 rpm s^{-1} as acceleration) using 50 μL per cell of PbI_2 solution in N,N-dimethylformamide (DMF) that was kept at 70°C under vigorous stirring. Immediately after the spin-coating step, the cells were placed onto a hot plate at 70°C for 30 minutes for annealing. The samples were allowed to cool to room temperature, after which the cells were dipped in the methylammonium iodide (MAI) solution in 2-propanol (8 mg mL^{-1}) for 20 s until the change of color from yellow to dark brown-black was observed. Subsequently, they were rinsed in pure 2-propanol and dried using the spin-coating machine at 4000 rpm for 30 s. Then, the samples were annealed again at 70°C for 30 minutes. For hole transporting materials, 35 μL of the Spiro-OMeTAD solution was spin-coated at 4000 rpm for 30 s. The Spiro-OMeTAD solution was made by dissolving 72.3mg of Spiro-OMeTAD in 1 mL of chlorobenzene; 21.9μL of tris(2-(1H-pyrazol-1-yl)-4-tert-butylpyrydine)cobalt(III) bis(trifluoro-methyl-sulphonyl)imide (FK209) stock solution (400 mg of FK209 in 1 mL of acetonitrile), 17.5 μL of lithium bis(trifluoromethylsulphonyl)imide (LiTFSI) stock solution (520 mg of LiTFSI in 1 mL of acetonitrile) and 28.8 μL of 4-tert-butylpyridine (tBP) were also added to the solution as additives. The cells were finally completed by thermally evaporating 150 nm of gold as a cathode under a vacuum level between $1 \cdot 10^{-6}$ and $1 \cdot 10^{-5}$ torr. PbI_2, MAI and Spiro-OMeTAD solutions were prepared inside an argon glove box under moisture and oxygen-controlled conditions (H_2O level: <1 ppm and O_2 level: <50 ppm). PbI_2 spin-coating, MAI dipping and Spiro-OMeTAD spin-coating depositions were developed inside a dry box. The reference sample without Spiro-

OMeTAD was fabricated in the same procedure, but PbI_2 was employed as 1.25 molar instead of 1M and no further HTM was deposited on these devices.

Appendix 2 – Recipe for fabricating the flat-junction perovskite cell:

Materials

Preparation of MAPI precursor: The MAPI precursor was prepared according to the following procedure from [19]: Twelve milliliters of hydroiodic acid (57 wt % in water, Sigma-Aldrich) was added dropwise in 2 h to 24 mL of methylamine (33 wt % in ethanol, Sigma-Aldrich) in 100 mL of ethanol. Solvent was removed on a rotary evaporator, and the product was recrystallized from diethyl ether to obtain methylammonium iodide (MAI) as a crystalline powder. The powder was dried in a vacuum chamber at 65 °C for 12 h. In a glovebox (N_2 atmosphere), MAI and PbI_2 (Aldrich, 99.999%, purified by vacuum oven two times) were dissolved in dimethylformamide (Tokyo Chemical Industry Co., 99.5%) at a molar ratio of 1:1 and stirred for 12 h at 60 °C to obtain a precursor solution. The total material concentration was 40 wt %.

Preparation of TiO_2 precursor:[141] To prepare a TiO_2 precursor solution, 438 μL of commercially available titanium isopropoxide (Tokyo Chemical Industry Co.) was diluted in 3 mL of isopropanol. In a separate flask, 83 μL of a 1 M HCl solution was diluted with isopropanol (3 mL) and added dropwise to the titanium precursor solution under rapid stirring. The solution was filtered through a polytetrafluoroethylene (PTFE) membrane filter with a 0.2 μm pore size just before use.

Materials for the hole-transporting layer: High-purity spiro-OMeTAD (>99.5) from Lumitech, 82.5 mg was dissolved in 1 mL of chlorobenzene with 15 μL of lithium bis(trifluoromethylsulphonyl)-imide (Li-TFSI; 520 mg/mL in CH3CN) and 22.5 μL of di-tert-butylperoxide (D-TBP).

Fabrication of solar cells: The devices were fabricated according to the following procedure. An indium tin oxide (ITO) layer with a thickness of 145 nm and a sheet resistance of 8 Ω/square was used on a glass substrate. The surface roughness, Ra, was 0.7 nm, and the Rmax value was 8.1 nm. Prior to the formation of the buffer layer, the patterned ITO glass was ultrasonically cleaned using a surfactant, rinsed with water, and then finally given UV−ozone treatment. Then, the TiO_2 precursor

solution was spin-coated onto the ITO at 3000 rpm for 30 s, and the coated ITO was heated to 470 °C for 30 min in air. The MAPI precursor solution was spin-coated onto the TiO_2 surface at 500 rpm for 3 s and 5000 rpm for 30 s, and then the surface was washed with 50 μL of chlorobenzene after 10 s under a nitrogen atmosphere. The crystalline MAPI active layer thus prepared was ca. 300 nm thick after 10 min of annealing at 100 °C.[142] The hole-transporting layer was then deposited by spin coating (2200 rpm for 30 s for Spiro-OMeTAD). The top electrode (Ag, 150 nm) was deposited through a metal shadow mask, which defined a 2 mm stripe pattern perpendicular to the ITO stripe. For Spiro-OMeTAD, we tested the device without encapsulation after storing it for 1 day in ambient air.

Appendix 3 – Recipe for fabricating the thin mesoporous perovskite cell:

Materials The recipe for the fabrication of the devices has already been published in ([110]). The exact procedure for the fabrication of the devices is simply transferred from the manuscript to this chapter. The devices were fabricated by my collaboration partners in the laboratory of the École polytechnique fédérale de Lausanne under the supervision of Wolfgang Tress, Michael Saliba, Mohammad Khaja Nazeeruddin and Michael Grätzel.

Substrate preparation and Li-doping TiO_2: Nippon Sheet Glass of $1\Omega sq^{-1}$ was cleaned by sonication in 2% Hellmanex water solution for 30 min. After rinsing with deionized water and ethanol, the substrates were further cleaned with ultraviolet ozone treatment for 15 min. Then, 30-nm TiO_2 compact layer was deposited on FTO via spray pyrolysis at 450 °C from a precursor solution of titanium diisopropoxide bis(acetylacetonate) in anhydrous ethanol. After the spraying, the substrates were left at 450 °C for 45 min and left to cool down to room temperature. Then, mesoporous TiO_2 layer was deposited by spin coating for 20 s at 4,000 r.p.m. with a ramp of 2,000 r.p.m. s^{-1}, using 30 nm particle paste (Dyesol 30 NR-D) diluted in ethanol to achieve 150 - to 200-nm-thick layer. After the spin coating, the substrates were immediately dried at 100 °C for 10 min and then sintered again at 450 °C for 30 min under dry air flow. Li-doping of mesoporous TiO_2 was accomplished by spin coating a 0.1M solution of Li-TFSI in acetonitrile. The solution was prepared freshly before the application in nitrogen atmosphere. 150 ml were poured on 1.4 * 2.4 cm^2 substrate. After 5 s of loading time, the spinning program started with an acceleration of 1,000 r.p.m. s^{-1} to a final speed of 3,000 r.p.m., the substrate was left spinning for 30 s. Both Li^+-doped and undoped electrodes were completed with a second calcination step at 450 °C for 30 min. After cooling down to 150 °C, the substrates were immediately

transferred in a nitrogen atmosphere glove box for the deposition of the perovskite films.

Perovskite precursor solution and film preparation: The perovskite films were deposited from a precursor solution containing FAI (1M), PbI_2 (1.1 M), MABr (0.2 M) and $PbBr_2$ (0.2 M) in anhydrous dimethylformamide/ dimethylsulphoxide (4:1 (v:v)) solution. The perovskite solution was spin coated in a two-step program at 1,000 and 4,000 r.p.m. for 10 and 30 s, respectively. During the second step, 100 μl of clorobenzene was poured on the spinning substrate 15 s prior the end of the program. The substrates were then annealed at 100 °C for 1 h in nitrogen-filled glove box. We note that the perovskite precursor solution for this cell was prepared with a different composition from what reported by Jeon et al., who used an equimolar amount of FAI and PbI_2 to achieve a certified PCE of 17.9% with the mixed halide and cation formulation, $(FAPbI_3)0.85(MAPbBr_3)0.15$.[31]

Hole transporting layer and top electrode: After the perovskite annealing, the substrates were cooled down for few minutes and a spirofluorene-linked methoxy triphenylamines (spiro-OMeTAD, from Merck) solution (70mM in chlorobenzene) was spun at 4,000 r.p.m. for 20 s. The spiro-OMeTAD was doped with bis(trifluoromethylsulfonyl)imide lithium salt (Li-TFSI, from Aldrich), tris(2-(1H-pyrazol-1-yl)-4-tert-butylpyridine)- cobalt(III) tris(bis(trifluoromethylsulfonyl)imide) (FK209, from Dyenamo) and 4-tert-Butylpyridine (TBP, from Aldrich).[143-145] The molar ratio of additives for spiro-OMeTAD was: 0.5, 0.03 and 3.3 for Li-TFSI, FK209 and TBP, respectively. Finally, 70–80 nm of gold top electrode was thermally evaporated under high vacuum.

Appendix 4 - Spectra of white light illumination UVICO-VIS:

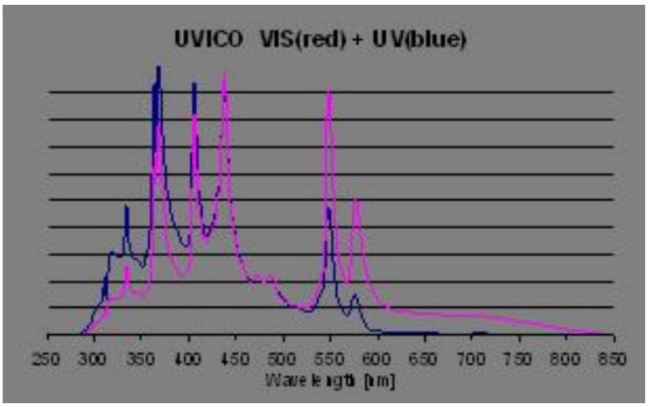

Figure 79: Spectra of the UVICO-VIS white light illumination which was used during the cross-sectional KPFM measurements

Appendix 5: Flat-junction device #1 – Comparison external bias ramp forward/backward

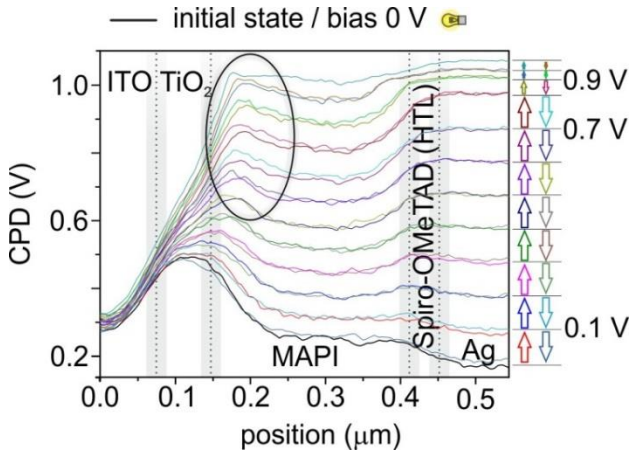

Figure 80: CPD profiles with a triangular external bias ramp applied to the Ag electrode. After each step of 0.1 V a profile is plotted both for the forward and the backward scan. The ramp was applied from 0 V to 1.1 V and back. The steps of 0.1 V can be detected on the Ag electrode. Above the open circuit potential the potential steps on the Ag electrode did not follow the applied bias from the external bias anymore, pointing to a breakdown of potential due to a reverse current. The black circle marks a region where the comparison between the forward and the backward scan reveals a positive offset. This positive offset is mainly created by the changes of the bias ramp within one scan line.

The scan rate of the IV curve was set to 0.02 V/s with a range from 0 V – 1.1 V forward and backward, while the scan rate of the KPFM scan was set to 1 Hz. In order to keep track of the changes in CPD versus the change in external bias, every CPD profile after each step of ~0.1 V was plotted (every 5 s ~ 5 lines). The differences in CPD correlated with the steps of the external bias in steps of 0.1 V after each 5 s could be observed on the Ag electrode. On the grounded ITO electrode, the CPD

stayed constant within the error of the measurement. When the forward and the backward scan at the same potential bias were compared, a positive offset for the backward scan was observed in front of the TiO_2 interface (Figure 80 - black circle). The most significant impact thereby is observable at an external bias of 0.7 V with ΔCPD = 40 mV. This increase in CPD is expected to be mainly caused by the changes of the bias ramp within one scan line (see explanation in 4.4.1 → $2 \cdot err = 2 \cdot 9\ mV = 18\ mV$). Therefore, no significant changes due to preconditioning could be concluded.

Notice: Above the open circuit voltage ~0.85 V, the CPD on the Ag electrode did not matched the applied potential step of the external supply anymore. However, the CPD within the perovskite MAPI still increased in similar steps compared to the previous profiles. An explanation could be that above the V_{OC} ~ 0.9 V, the applied external potential broke down since the V_{OC} was overcome and a current in opposite direction built up. Thereby, additional charges could not be collected on the electrode anymore and spread across the device. Another possibility is a malfunction of the waveform generator.